

AD-A060 004

ILLINOIS UNIV AT URBANA-CHAMPAIGN DEPT OF METALLURGY --ETC F/G 11/6  
PRECIPITATION AND ORDERING IN THE NIOBium-HYDROGEN SYSTEM.(U)

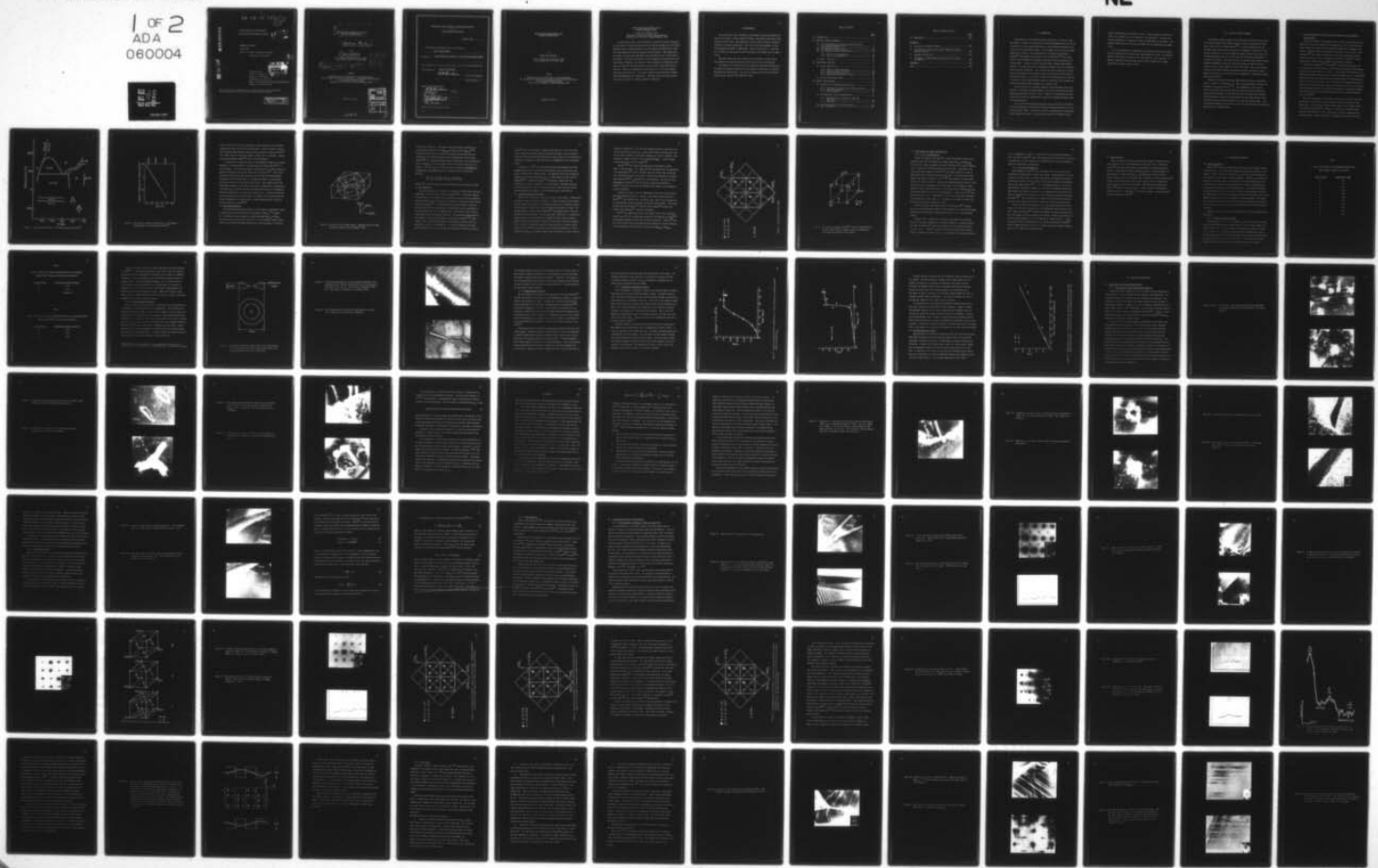
JUL 78 B J MAKENAS

N00014-75-C-1012

NL

UNCLASSIFIED

1 OF 2  
ADA  
060004



78 08 08 151

123

ADA060004

PRECIPITATION AND ORDERING  
IN THE NIOBIUM-HYDROGEN SYSTEM

VAL

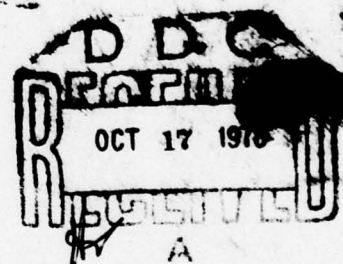
TECHNICAL REPORT

July 1978

Office of Naval Research Contract

USN 000 14-75-C-1012

DDC FILE COPY



Submitted by:

Bruce J. Makenas

Howard K. Birnbaum

University of Illinois

Dept. of Metallurgy & Mining Engineering  
Urbana, Illinois 61801

This document is unclassified. Distribution and reproduction  
for any purpose of the U.S. Government is permitted.

**DISTRIBUTION STATEMENT A**  
Approved for public release  
Distribution Unlimited

78 08 08 151

⑥

PRECIPITATION AND ORDERING IN THE  
NIOBium-HYDROGEN SYSTEM

⑦ Doctoral thesis,

⑩

BY

BRUCE JAMES MAKENAS

B.S., Michigan State University, 1972  
M.S., University of Illinois, 1973

⑪ Jul 78

⑫ 169P

⑯ N00014-75-C-1012

THESIS

Submitted in partial fulfillment of the requirements  
for the degree of Doctor of Philosophy in Metallurgical Engineering  
in the Graduate College of the  
University of Illinois at Urbana-Champaign, 1978 ✓

Urbana, Illinois

ACCESSION NO.	
176	UNIV. LIBRARIES
000	UNIV. LIBRARIES
UNABRIDGED	
NOT INDEXED	
FILED	
MAY 1978	
DISTRIBUTION/AVAILABILITY CODES	
000	AVAIL. AND/OR SPECIAL
A	

176014

fb

UNIVERSITY OF ILLINOIS AT URBANA-CHAMPAIGN

THE GRADUATE COLLEGE

January, 1978

WE HEREBY RECOMMEND THAT THE THESIS BY

BRUCE JAMES MAKENAS

ENTITLED PRECIPITATION AND ORDERING IN THE NIOBium-HYDROGEN SYSTEM

BE ACCEPTED IN PARTIAL FULFILLMENT OF THE REQUIREMENTS FOR  
THE DEGREE OF DOCTOR OF PHILOSOPHY

H K Birnbaum

Director of Thesis Research

Head of Department

Committee on Final Examination†

H K Birnbaum

Chairman

E N Pugh

Harry Ahren

C P Bollerhwaert

Tim Sinclair

† Required for doctor's degree but not for master's.

PRECIPITATION AND ORDERING IN THE  
NIOBIUM-HYDROGEN SYSTEM

BY

BRUCE JAMES MAKENAS

B.S., Michigan State University, 1972  
M.S., University of Illinois, 1973

THESIS

Submitted in partial fulfillment of the requirements  
for the degree of Doctor of Philosophy in Metallurgical Engineering  
in the Graduate College of the  
University of Illinois at Urbana-Champaign, 1978

Urbana, Illinois

PRECIPITATION AND ORDERING IN THE  
NIOBIUM-HYDROGEN SYSTEM

Bruce James Makenas, Ph.D.

Department of Metallurgy and Mining Engineering  
University of Illinois at Urbana-Champaign, 1978

An experimental study, using Transmission Electron Microscopy techniques was carried out to observe precipitation and ordering phenomena in the Niobium-Hydrogen system. Niobium-Hydrogen alloys of composition  $H/Nb=0.001$  to  $H/Nb=1.07$  were prepared by improved hydrogen charging methods. Room temperature, hot stage, and cold stage experiments were performed *in situ* in the electron microscope. The plastic deformation, which accompanies the precipitation and dissolution of hydrides, was observed. Volume constraint, temperature gradients, and impurity traps were shown to have an effect on the nucleation of hydrides. Several low temperature ordered phases  $\zeta$ ,  $\epsilon$  and  $\lambda$  were studied using electron diffraction. The crystal structures were observed to change with both temperature and composition. The  $NbH_2$ ,  $\delta$ -phase was also studied and shown to consist of a highly twinned fcc structure.

## ACKNOWLEDGMENT

The author would like to gratefully acknowledge the patient guidance and help of his advisor, Professor Howard Birnbaum. Many helpful discussions with Professor Hamish Fraser, John Woodhouse, Ian Ward, Nestor Zalusec, and Martin Grossbeck are greatly appreciated. Also the help and encouragement of many fellow graduate students is appreciated. Thanks are due to Dr. T. Brun and Dr. D. Potter for making their results available to the author prior to publication.

The author would also like to thank his wife, Vickie, for her loving encouragement and understanding during the course of this investigation.

The support of the Microstructure and Analytical Chemistry Facilities of the Materials Research Laboratory and the support of the Center for Electron Microscopy are acknowledged. This work was supported by the Office of Naval Research under contract USN N 00014-75-C-1012.

## TABLE OF CONTENTS

	<u>Page</u>
1.0 INTRODUCTION .....	1
2.0 REVIEW OF PREVIOUS RESEARCH .....	3
2.1 The Precipitation of Hydrides from Solid Solution at Low Hydrogen Concentrations .....	4
2.2 The $\alpha$ Niobium Hydride .....	7
2.3 Low Temperature Ordered Phases .....	10
2.4 High Temperature Phase Transformations .....	14
2.4.1 The $\alpha \leftrightarrow \alpha' + \alpha''$ Transformation .....	14
2.4.2 The $\alpha' \rightarrow \beta$ Transformation .....	15
2.5 NbH <sub>2</sub> - $\delta$ Hydride .....	16
3.0 EXPERIMENTAL PROCEDURE .....	17
3.1 Sample Preparation .....	17
3.1.1 Thin Foil Niobium Specimens .....	17
3.1.2 Palladium Coated TEM Samples .....	20
3.1.3 Gaseous Hydrogen Charging .....	24
3.1.4 Electrolytic Charging of Niobium .....	25
3.2 Electron Microscopy Studies .....	28
4.0 RESULTS AND DISCUSSION .....	30
4.1 Hydrides at Low Hydrogen Concentrations .....	30
4.1.1 TEM Studies of Precipitation and Dissolution .....	30
4.1.2 Beam Heating Effects .....	47
4.1.3 Trapping Effects .....	52
4.2 Low Temperature Phase Transformations .....	53
4.2.1 Transformations in Samples of H/Nb Less Than 0.70 .....	53
4.2.2 The $\lambda$ Phase .....	79
4.3 The High Temperature $\alpha' \rightarrow \beta$ Transformation .....	111
4.4 NbH <sub>2</sub> - $\delta$ Hydride .....	117

## TABLE OF CONTENTS (Cont'd)

	<u>Page</u>
5.0 CONCLUSIONS .....	124
APPENDICES	
A. Flow Chart of Computer Program .....	126
B. The Formation of Oxides During High Temperature Gaseous Hydrogen Charging .....	127
C. Hydrogen Ion Charging .....	149
D. The Effects of High Temperature Annealing on Thin Foils of Niobium .....	151
REFERENCES .....	156
VITA .....	160

## 1.0 INTRODUCTION

Investigations of the niobium-hydrogen system have, in the past, been motivated by a number of scientifically interesting phenomena and also by the possibility of using niobium based alloys in the hydrogen environments associated with various energy systems. In this regard, one of the most notable properties of niobium is its susceptibility to hydrogen embrittlement.

Westlake<sup>(1)</sup> has proposed and Grossbeck, Gahr and Birnbaum<sup>(2-3)</sup> have shown that this embrittlement is intimately connected with the precipitation of a hydride phase. In order to fully understand these hydrogen embrittlement effects, it is necessary to have a thorough knowledge of the various hydride phases and their properties. This includes the crystal structure and composition of hydrides and the conditions under which hydride will precipitate from solid solution. To this end, a study of the precipitation and ordering of hydrides in the niobium hydrogen system was undertaken using Transmission Electron Microscopy (TEM) techniques as a principal tool.

Several techniques for hydrogen charging of thin specimens were investigated. An improved charging procedure, utilizing an evaporated palladium coating was developed for niobium foils. Aspects of contamination by other interstitials were also explored and a mechanism of hydrogen enhanced oxidation was formulated.

In situ cooling and heating experiments were carried out in the TEM to study the morphology of hydride precipitation and hydride dissolution in low H concentration alloys. The details of plastic accommodation of precipitate volume changes were noted. The effects of varying foil thickness and of

electron beam heating were studied in detail. Higher hydrogen concentration alloys, up to  $H/Nb=1$ , were also studied at low temperatures. Electron diffraction evidence for a sequence of several ordered phases was obtained. The hydrogen sublattices were observed to change with both temperature and composition.

In situ high temperature morphological and electron diffraction studies were also performed in the composition range  $H/Nb=0.50$  to  $0.90$ . The transformation of the ordered  $\beta$  hydride to the solid solution  $\alpha'$  was observed. In addition, specimens containing  $NbH_2.5$  hydride were prepared and a highly twinned fcc structure shown to result.

## 2.0 REVIEW OF PREVIOUS RESEARCH

The elements oxygen, nitrogen and hydrogen form interstitial solid solutions with the group Vb bcc metals vanadium, niobium and tantalum and also form a large number of ordered phases<sup>(4-7)</sup>. In these ordered phases the non-metal atoms occupy a specific subset of the possible interstitial sites and the resulting unit cells are generally larger than the simple metal cell. The ordering phases exist over a wide range of stoichiometry and exhibit a variety of structures. These often result from different but closely related ordered arrangements of both the interstitial atoms and the interstitial vacancies on the allowed subset of interstitial sites. This is particularly evident in the niobium-hydrogen system which contains an extensive single phase solid solution, a region of spinodal decomposition, and several ordered hydride modifications.

Transmission Electron Microscopy (TEM) methods have been successfully used by a number of investigators to study the ordered oxides, nitrides, and hydrides of the group Vb metals<sup>(7-9)</sup>. Both morphological and electron diffraction studies have been performed and have utilized the significant atomic scattering factors of the light interstitial elements for electrons. Diffraction patterns from the ordered phases show weak superlattice reflections due to the scattering of electrons by light interstitial atoms. This diffraction information can be used to aid in the identification and structure determination of ordered phases.

## 2.1 The Precipitation of Hydrides from Solid Solution at Low Hydrogen Concentrations

As shown in Figures 1-2, hydrogen forms a limited solid solution (up to  $H/Nb=0.04$ ) with the bcc niobium at room temperature. The  $\alpha$  solid solution region becomes more extensive with increasing temperature. Hydrogen is believed to randomly occupy the tetrahedral interstices in the  $\alpha$  phase. Pick and Bausch<sup>(10)</sup> have recently reported that the lattice parameter increase of the bcc lattice, due to the addition of hydrogen, is  $4.72 \times 10^{-4} \Delta a/a$  per atomic percent (H/Nb) where  $a=3.3044\text{\AA}$  for hydrogen free niobium.

Optical metallography<sup>(11-13)</sup> and SEM<sup>(14)</sup> studies have shown that, on slow cooling the  $\alpha$  solid solution, the  $\beta$  hydride precipitates in bulk samples in the form of plates parallel to  $\{100\}_c$ . Large numbers of dislocations are contained both within these plates and in the surrounding matrix. Westlake<sup>(15)</sup> has determined the low concentration  $\alpha \leftrightarrow \alpha + \beta$  phase boundary for niobium hydride (Figure 2) during slow cooling. Due to the large volume change which accompanies the  $\alpha \rightarrow \beta$  transformation,  $(\Delta V/V)_{\alpha \rightarrow \beta} = 11.9$  percent, this solvus is not the true thermodynamic equilibrium solvus but corresponds to equilibrium between the  $\alpha$  solid solution and  $\beta$  hydride particles which are constrained by the solid solution<sup>(16)</sup>.

Thin foils containing a small amount of hydrogen (less than 4 percent) are entirely in the  $\alpha$  solid solution region of the phase diagram at room temperature. If these foils are then cooled rapidly, small, roughly spherical, hydrides precipitate<sup>(9)</sup>. A number of interstitial prismatic loops, which have been emitted in  $\langle 111 \rangle_c$  directions, are usually associated with the precipitates. These dislocations are thought to partially relieve the

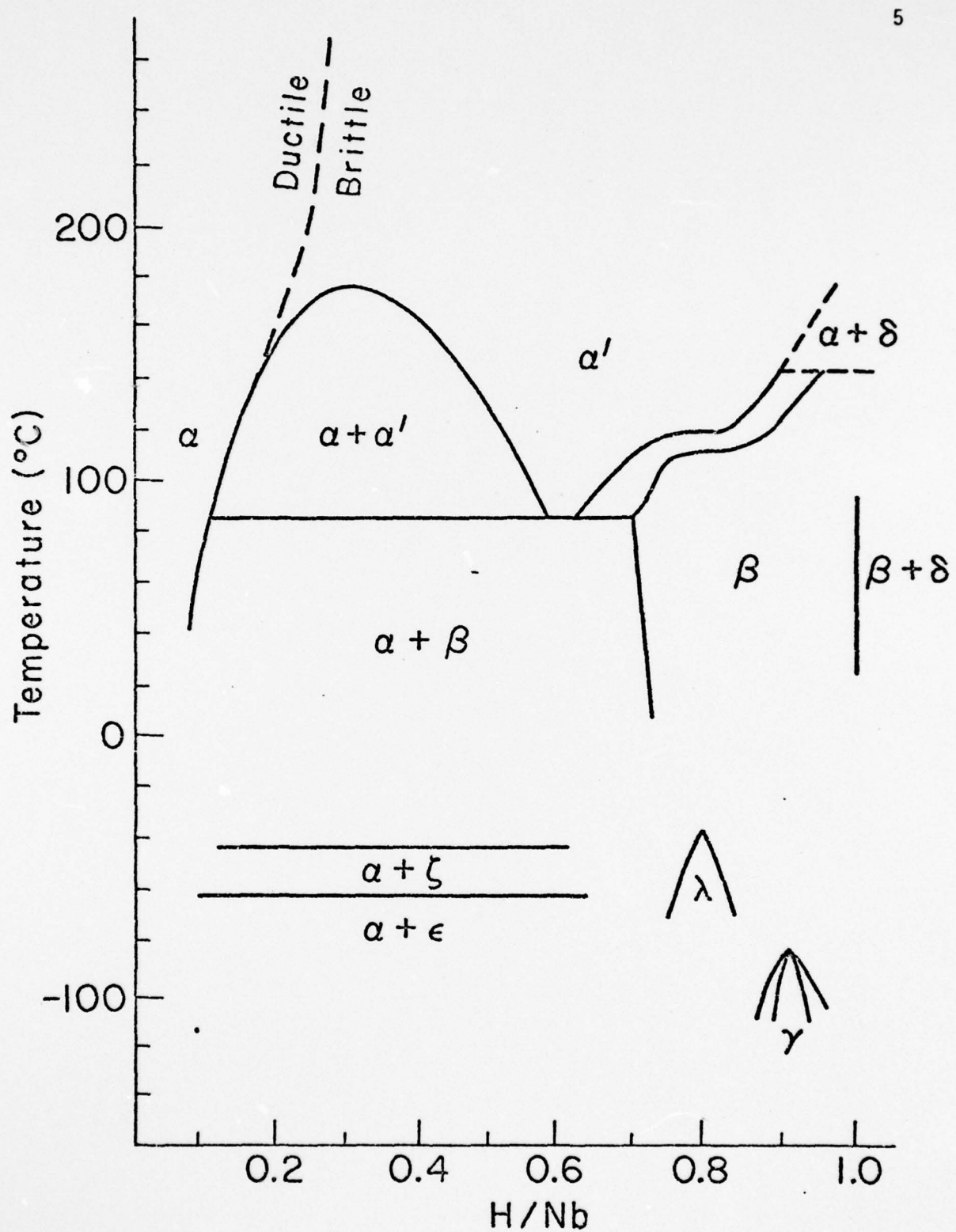


Figure 1. A partial phase diagram of the Niobium-Hydrogen system<sup>(64)</sup>.

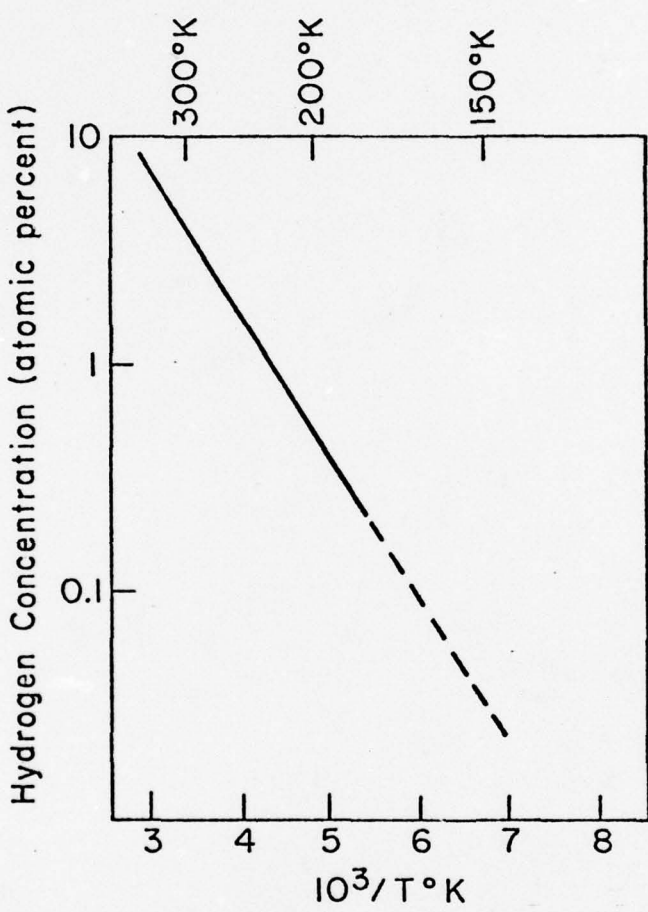


Figure 2. The solvus for hydride precipitation at low hydrogen concentrations as determined by Westlake<sup>(4)</sup>.

misfit strains that arise from the greater lattice parameter of the hydride compared with that of the solid solution matrix. Similar prismatic interstitial loops have been observed during the precipitation of niobium nitride<sup>(17)</sup> and in both cases the loops have Burger's vector  $\frac{1}{2}\langle 111 \rangle$  as expected. Several other metal-hydrogen systems<sup>(18)</sup> exhibit the same behavior.

It should also be noted that there is considerable evidence for a thermal hysteresis in the precipitation and dissolution of niobium hydride<sup>(15)</sup> in bulk specimens. The nucleation, growth, and dissolution of niobium hydride is greatly influenced by the volume constraint of the matrix<sup>(16)</sup>. Both elastic and plastic work must be done during both the  $\alpha \rightarrow \beta$  and  $\beta \rightarrow \alpha$  transformations. Precipitation of  $\beta$  hydride occurs at a temperature which is significantly below the stress free or true equilibrium solvus. This happens because the free energy required for the elastic and plastic accommodation is supplied by increasing  $\Delta G_{\alpha \rightarrow \beta}$  (chemical) through undercooling below the true thermodynamic equilibrium temperature at which  $\Delta G_{\alpha \rightarrow \beta}$  (chemical) = 0. The thermal hysteresis which accompanies the  $\beta \rightarrow \alpha$  transformation is thought to be associated with the work of accommodation on heating since a volume change opposite to that observed on cooling is required<sup>(16)</sup>.

## 2.2 The $\beta$ Niobium Hydride

The niobium-hydrogen system exhibits a face-centered orthorhombic  $\beta$  phase in the vicinity of the stoichiometric composition of  $\text{NbH}_{1.0}$ <sup>(19)</sup> (Figure 1). This phase has been reported to extend from about  $\text{NbH}_{0.75}$  to  $\text{NbH}_{1.0}$  and to have the structure shown in Figure 3. The arrangement of metal atoms differs only slightly from body centered cubic with the degree of distortion

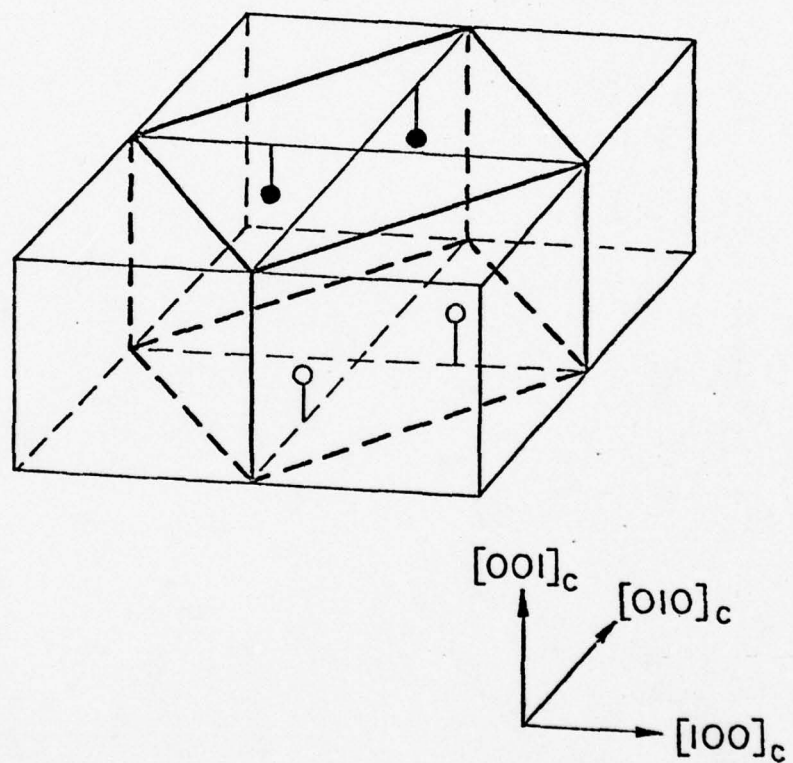


Figure 3. The unit cell of the NbH  $\beta$  phase. Hydrogen atoms are shown to occupy a subset of the tetrahedral sites.

varying with composition. The angle between the  $[100]_c$  and  $[010]_c$  deviates from  $90^\circ$  by about  $0.5^\circ$  at  $\text{NbH}_{0.80}$  and about  $0.8^\circ$  at  $\text{NbH}_{0.95}$ .<sup>(10)</sup>

Formation of the  $\beta$  hydride from solid solutions can therefore occur by ordering of the H atoms with only elastic displacement of the Nb atoms.

Somenkov<sup>(20)</sup> has demonstrated using neutron diffraction, that the deuterium atoms in  $\text{NbD}_{0.95}$  are ordered on the subset of tetrahedral sites shown in Figure 3. This structure is related to the bcc  $\alpha$  phase by  $[100]_0 \parallel [110]_c$ ,  $[010]_0 \parallel [110]_c$ ,  $[001]_0 \parallel [001]_c$  and has hydrogen solutes at tetrahedral positions

$$\left(\frac{1}{4} \frac{1}{4} \frac{1}{4}\right)_0, \left(\frac{3}{4} \frac{3}{4} \frac{3}{4}\right)_0, \left(\frac{3}{4} \frac{1}{4} \frac{1}{4}\right)_0 \text{ and } \left(\frac{1}{4} \frac{3}{4} \frac{3}{4}\right)_0.$$

Schober<sup>(21)</sup> using TEM, demonstrated that  $\text{NbH}$  has the same structure as  $\text{NbD}$  at room temperature.

One striking feature of  $\beta$  hydride, as studied in TEM and polarized light microscopy, is the presence of domain boundaries<sup>(21)</sup>. In TEM these boundaries are seen as thin ribbons of fringe contrast within an area of  $\beta$  hydride. Similar boundaries were also observed in alloys of niobium with interstitials other than hydrogen<sup>(22)</sup>. From the ordered  $\beta$  structure shown in Figure 3, one sees that there are six equivalent orientations for the orthorhombic  $\beta$  unit cell relative to the bcc niobium matrix. The domains differ by their orientations relative to the bcc unit cell. The boundaries between domains are coherent twin boundaries and show  $\delta$  interference fringes<sup>(23-24)</sup> when imaged in TEM. These domain boundaries are highly mobile under stress as expected for coherent twin boundaries. It has been suggested that these domain boundaries are due to an attempt by the hydride to lower its overall

energy<sup>(13)</sup> while maintaining an interface with the  $\alpha$  or  $\alpha'$  bcc solid solutions. Even though domain boundaries necessarily imply a certain amount of interfacial energy, the alternating layers of two or more twin related domains decreases the amount of strain that must be accommodated by the surrounding matrix.

Cassidy et al.,<sup>(25)</sup> have suggested that the crystallography and shape change associated with the hydride transformations can be described by the theory of martensitic transformations. The applicability of the martensitic theory has so far been demonstrated for a limited number of metal hydride systems<sup>(25-26)</sup>. Rashid and Scott,<sup>(27)</sup> furthermore, suggest that the nucleation of hydride is possibly a two step process. Hydrogen atoms may first concentrate and order in dislocation stress fields and then hydride nucleation possibly proceeds by a diffusionless shear transformation.

### 2.3 Low Temperature Ordered Phases

Many of the "interstitial phases" exist over a wide range of compositions as shown in Figure 1 for the NbH  $\beta$  phase. In these systems only the stoichiometric composition can have the idealized structure with complete occupancy of the subset of interstitial sites upon which the structure is based. For non-stoichiometric compositions, Somenkov<sup>(28)</sup> has proposed that a series of ordered structures can form. If the composition is deficient in interstitial atoms, relative to the stoichiometric composition, this series of phases results from placing vacancies on specific sites of the interstitial sublattice in order to increase the degree of order relative to a random distribution of the interstitial solutes on the interstitial sublattice. At the composition NbD<sub>0.75</sub>, for example, above 170°K, the  $\beta$  phase is stable with an

occupation probability of 0.75 for the allowed tetrahedral interstitial sub-lattice sites of the  $\beta$  structure. Below 170°K further ordering occurs and only a specific subset of the  $\beta$  phase interstitial sites is occupied. This structure is shown in Figure 4 and is designated  $\text{Nb}_4\text{D}_3$ . A similar phase has been reported in the Ta-D system<sup>(28)</sup>.

Schober<sup>(9,30)</sup> has reported the  $\text{Nb}_4\text{H}_3$  phase (designated  $\epsilon$ ) below 208°K in TEM specimens. The  $\epsilon$  phase has not been detected by low temperature x-ray measurements<sup>(31)</sup>, which indicates that the volume change during the  $\beta \rightarrow \epsilon$  transformation must be very small. Optical metallography has similarly been unsuccessful<sup>(32)</sup> in detecting the  $\beta \rightarrow \epsilon$  transition. The specific heat measurements of Heibel<sup>(33)</sup> and the elastic constant measurements of Amano<sup>(34)</sup> do show a transition at 208-209°K which appears to correspond to the  $\beta \rightarrow \epsilon$  transition.

In addition, several other low temperature transitions and structures have been reported (Figure 1). Schober, using electron diffraction evidence<sup>(9,30)</sup>, has reported that, on heating, the  $\epsilon$  phase first transforms to an intermediate structure (designated  $\zeta$ ) between 228 and 208°K. The  $\zeta$  phase was not observed by Heibel<sup>(33)</sup> (specific heat), Amano<sup>(34)</sup> (elastic constants) or by Somenkov<sup>(29)</sup> (neutron diffraction).

Pick<sup>(31)</sup> has demonstrated with x-ray methods, that a cubic hydride,  $\gamma$ , exists below 173°K at an approximate composition of  $\text{H}/\text{Nb}=0.91$  and Hauck<sup>(35)</sup> has proposed hydrogen positions for this phase (Figure 5). Schober<sup>(32)</sup> has also seen evidence (optical metallography and differential thermal analysis) for low temperature transformations in the region  $\text{NbH}_{0.80}$  to  $\text{NbH}_{0.98}$ .

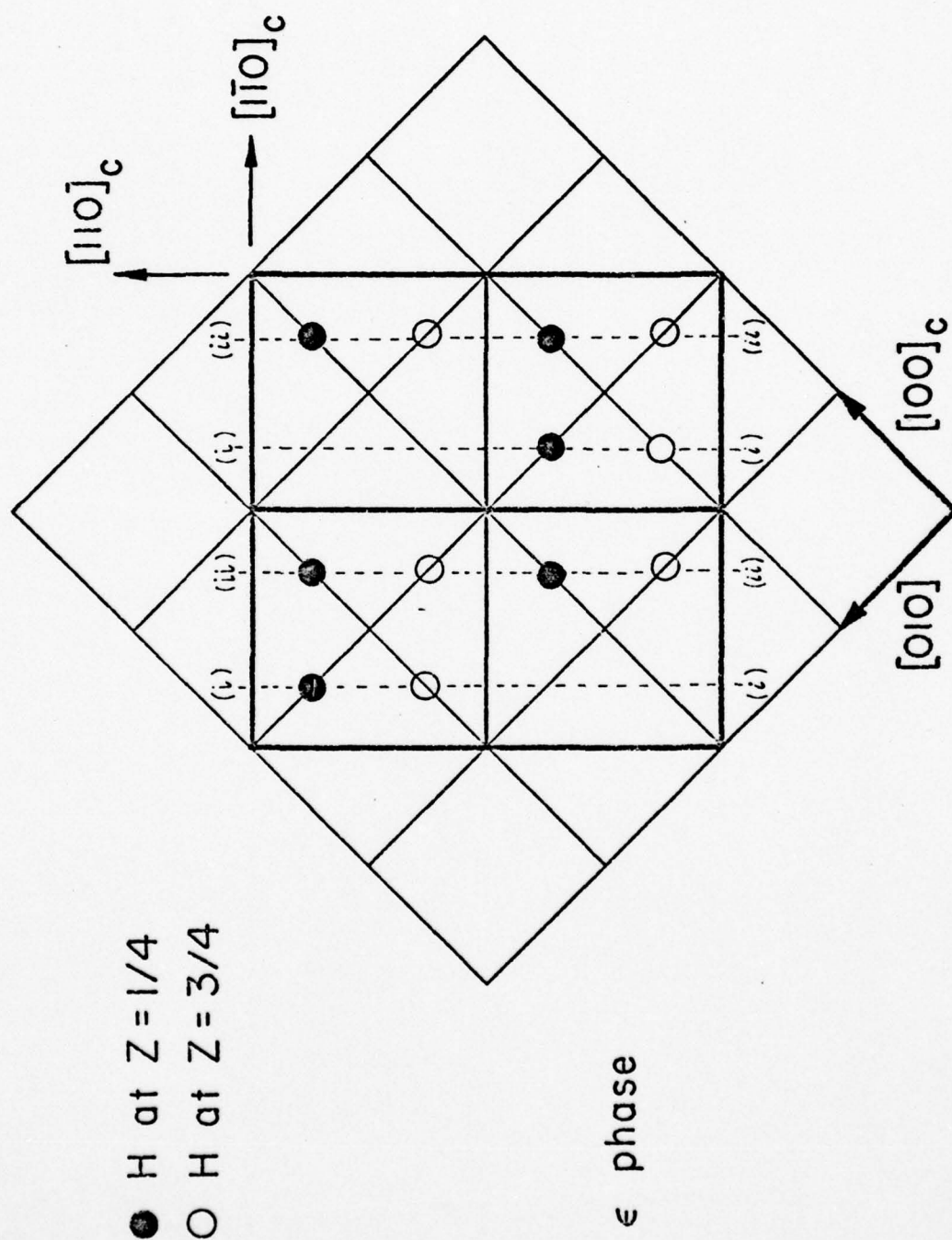


Figure 4. The unit cell of the  $\epsilon$  phase.

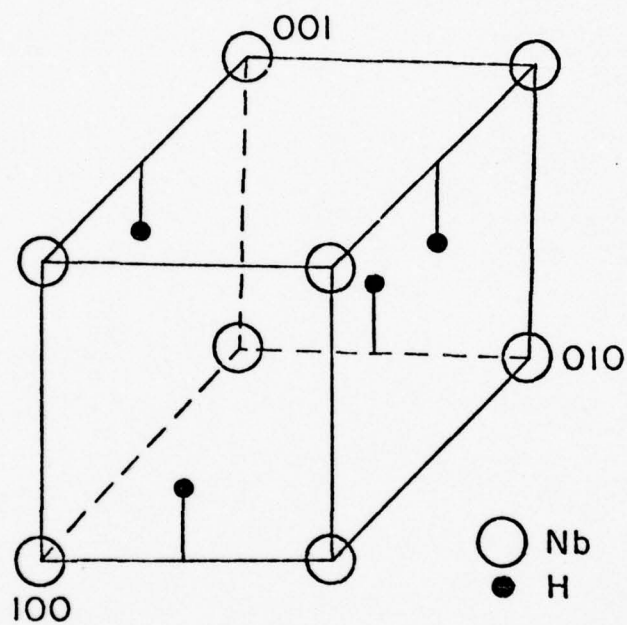


Figure 5. The structure proposed by Hauk<sup>(35)</sup> for the  $\gamma$ -hydride phase. Hydrogen atoms occupy a different subset of tetrahedral sites than allowed in the  $\beta$  phase.

## 2.4 High Temperature Phase Transformations

### 2.4.1 $\alpha \rightarrow \alpha + \alpha'$ Transformation

Walter and Chandler have shown<sup>(19)</sup>, using x-ray methods, that at temperatures above 78°C and compositions between about NbH<sub>0.15</sub> and NbH<sub>0.50</sub>, the bcc solid solution undergoes a spinodal decomposition to two bcc phases,  $\alpha$  and  $\alpha'$  (Figure 1) of differing hydrogen concentrations. According to the lattice gas model proposed by Alefeld<sup>(36)</sup> this phase separation is due to long range elastic interactions between hydrogens via the host metal atoms. Recent x-ray studies by Zabel, et al.<sup>(37-38)</sup> have found the critical point of the  $\alpha + \alpha'$  field to be 85°C. They have also demonstrated that the  $\alpha + \alpha'$  separation persists to temperatures well above 300°C in the presence of large amounts of plastic deformation such as dislocation debris introduced during  $\beta$  hydride precipitation at or below room temperature. Fenzl, et al.,<sup>(39)</sup> have also studied the  $\alpha$  to  $\alpha + \alpha'$  decomposition with a  $\gamma$  ray diffraction technique. They observed that {100} plates of  $\alpha'$  nucleated at the edges of niobium samples during electrolytic charging at 140°C.

Lattice parameter measurements made by Pick and Bausch<sup>(10)</sup> indicate that at elevated temperature (160°C) lattice expansion is linear with hydrogen concentration and continuous throughout the entire  $\alpha$  and  $\alpha'$  solid solution regions.

Although  $\alpha$  and  $\alpha'$  appear to be identical body centered cubic phases, except for hydrogen concentration and lattice parameter, it should be noted that Gahr and Birnbaum<sup>(3)</sup> have found differences in the mechanical properties of  $\alpha$  and  $\alpha'$ . Samples fractured in the  $\alpha$  phase region showed ductile fracture surfaces while those in the  $\alpha'$  region showed flat cleavage fractures.

up to a temperature of 400°C. In addition, the resistivity measurements of Maier and Wipf at 196°C<sup>(40)</sup> show increasing resistivity values with increasing H concentration in solid solution until H/Nb=0.6 where resistivity begins to drop with increasing H concentration.

#### 2.4.2 The $\alpha' \rightarrow \beta$ Transformation

Metallographic studies<sup>(13)</sup> have shown that the  $\alpha'$  solid solution will transform to the multidomain  $\beta$  phase upon cooling. Domain boundaries in such crystals are mobile under the influence of stress and temperature gradients, and domain free bulk  $\beta$  hydride single crystals can be grown by taking advantage of this domain mobility<sup>(41)</sup>. In  $\alpha'$  the hydrogen atoms are, as a first approximation, distributed randomly over all of the tetrahedral interstices. Some evidence for deuterium correlations corresponding to the  $\beta$  phase interstitial occupancy has been reported in the  $\alpha'$  phase using neutron scattering techniques<sup>(42)</sup>. The correlations correspond to extensive short range order well above the  $\beta$  phase boundary and indicate very strong D-D interactions.

At the  $\alpha' \rightarrow \beta$  transition temperature,  $T_c$ , the hydrogen atoms order onto a subset of 1/3 of the tetrahedral sites corresponding to the  $\beta$  hydride structure. Amano and Birnbaum<sup>(34)</sup> studied the behavior of elastic constants near the  $\alpha' \rightarrow \beta$  boundary during both heating and cooling. Evidence was found for an elastic constant softening in C' at temperatures slightly above  $T_c$ . These pretransition elastic phenomenon above  $T_c$  and the calculations of Hauck<sup>(35)</sup> further suggest the possibility of short range correlations between hydrogen atoms in this region of the phase diagram.

## 2.5 $\text{NbH}_2$ - $\delta$ Hydride

Above the composition  $\text{NbH}_{1.0}$  the particular subset of tetrahedral positions allowed in the  $\beta$  hydride structure is entirely filled. Reilly and Wiswall<sup>(43)</sup> have used high pressure  $\text{H}_2$  charging and x-ray measurements to show that a hydride with composition  $\text{NbH}_{1.8}$  forms in increasing amounts as more hydrogen is added above  $\text{NbH}_{1.0}$ . The  $\text{NbH}_2$  phase,  $\delta$  hydride (often called  $\gamma$  hydride in older literature) has a structure in which the metal atoms occupy a face centered cubic lattice, with  $a_0 = 4.53$ , which is formed from the bcc lattice by elastic displacements. The  $\delta$  hydride precipitates on  $\{102\}_c^{(32)}$  planes within the  $\beta$  phase. Little is known of the hydrogen lattice structure or morphology of this phase although a flourite structure has been suggested by Hauck<sup>(35)</sup>.

### 3.0 EXPERIMENTAL PROCEDURE

#### 3.1 Sample Preparation

Westlake<sup>(44)</sup> had demonstrated that electropolishing of hydrogen charged refractory metals can significantly change the hydrogen concentration of the samples. Either increases or decreases in C<sub>H</sub> have been reported depending on the metal and the detailed thinning procedure. Therefore, controlled compositions of hydrogen cannot be maintained on thinning precharged specimens. In addition, acid electropolishing techniques are known to preferentially attack second phases such as hydride precipitates. The extensive handling during polishing may also cause the very brittle hydride samples to shatter. For these reasons, throughout this study, hydrogen was introduced into niobium samples only after all thinning procedures had been completed. All samples were examined in TEM between the thinning and charging steps and any samples which showed evidence of hydrogen pickup or deformation during thinning were discarded.

Hydrogen analysis of specimens was performed using hot vacuum extraction techniques.

##### 3.1.1 Thin Foil Niobium Specimens

Niobium strips (1 in. x 4 in. x 0.004 in.) were cut from an as-received sheet and then UHV outgassed at 2100°C and 10<sup>-10</sup> torr to remove oxygen and nitrogen impurities. A typical analysis for impurities is given in Table 1 and 2. Discs, 3 mm in diameter, were cut from the outgassed sheet using a standard specimen punch and plastic deformation during this cutting operation was entirely confined to the rim of each disc. No differences were noted between these samples and discs which have been sparkcut from sheets.

TABLE 1

A TYPICAL SPARK SOURCE MASS SPECTROMETRY ANALYSIS FOR  
SUBSTITUTIONAL IMPURITIES IN NIOBIUM

<u>Solute Element</u>	<u>Concentration (ppm)</u>
Si	4.0
Ti	0.1
V	0.2
Cr	0.04
Mn	0.03
Fe	0.03
Cu	0.1
Zn	0.06
Mo	0.4
Ta	10.0
W	5.0

TABLE 2

TYPICAL INTERSTITIAL IMPURITY CONCENTRATIONS FOR UHV ANNEALED  
NIOBIUM SHEET DETERMINED BY VACUUM FUSION ANALYSIS

<u>Solute Element</u>	<u>Concentration (atomic percent)</u>
O	0.03
N	0.02
C	undetectable

TABLE 3

TYPICAL INTERSTITIAL IMPURITY CONCENTRATIONS AFTER THE PALLADIUM COATING  
PROCEDURE DETERMINED BY VACUUM FUSION ANALYSIS

<u>Solute Element</u>	<u>Concentration (atomic percent)</u>
O	0.06
N	0.02
C	0.02

Several techniques are known to produce good quality niobium specimens for TEM<sup>(45,46)</sup>. The following technique, used in this study, was found to consistently produce large electron transparent areas (Figure 7) (<2000Å in thickness). The 3 mm niobium discs were jet thinned from both sides to a concave shape in a stream of H<sub>2</sub>SO<sub>4</sub>:HF:Methanol, 2:1:7 at 100-125 volts.\* Final electropolishing to perforation was accomplished in a solution of H<sub>2</sub>SO<sub>4</sub>:HF:lactic acid, 1:1:2 at 3 volts using platinum tipped tweezers to hold the specimens and an aluminum cathode. Samples were washed in aqua regia, water and methanol and quickly dried in a warm air stream. The final geometry of the sample is given in Figure 5.

### 3.1.2 Palladium Coated TEM Samples

Oxide layers which act as barriers to hydrogen pickup are characteristic of the group Vb refractory metals at room temperature. The following technique was developed in order to replace the low permeability oxide layer with a high hydrogen permeability layer of palladium. UHV annealed niobium sheet samples (0.5 x 2 x 0.004 in.) were mounted in stainless steel grips in a glass bell jar vacuum system. The niobium specimens were then resistance heated to 700°C at  $5 \times 10^{-6}$  torr for one minute to dissolve the oxide layer. During cooling a thin layer of palladium was evaporated from a hot tungsten basket onto one side of the niobium sheet. A typical interstitial impurity analysis of the sample following this treatment is given in Table 3.

---

\*The mixing of H<sub>2</sub>SO<sub>4</sub> and Methanol is highly exothermic and the initial mixing should be done with a liberal quantity of dry ice to cool the solution.

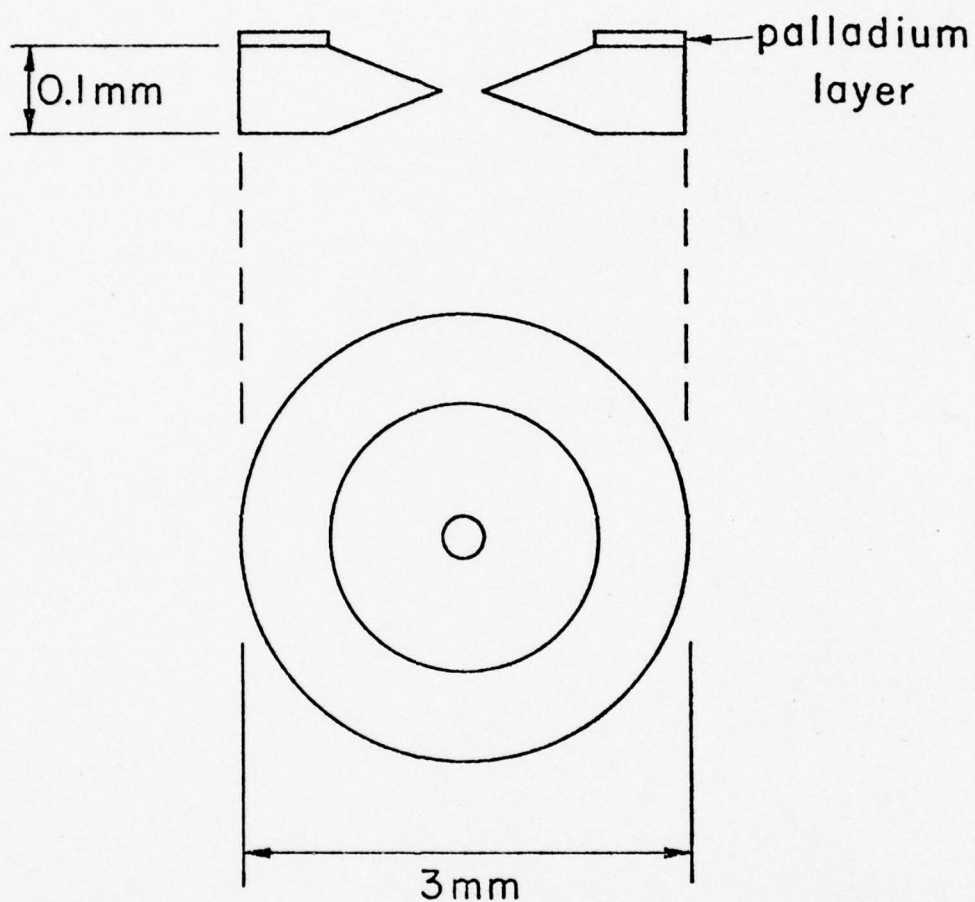
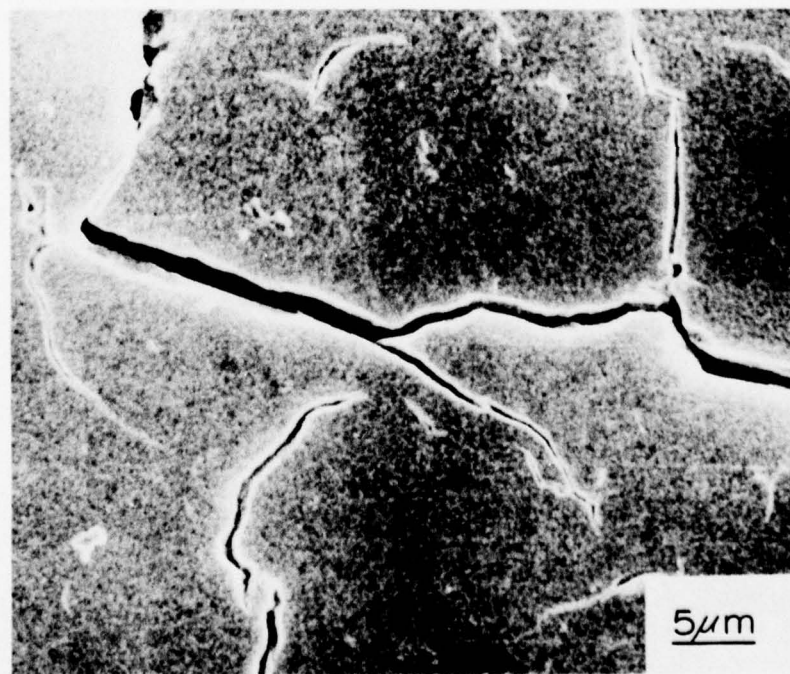
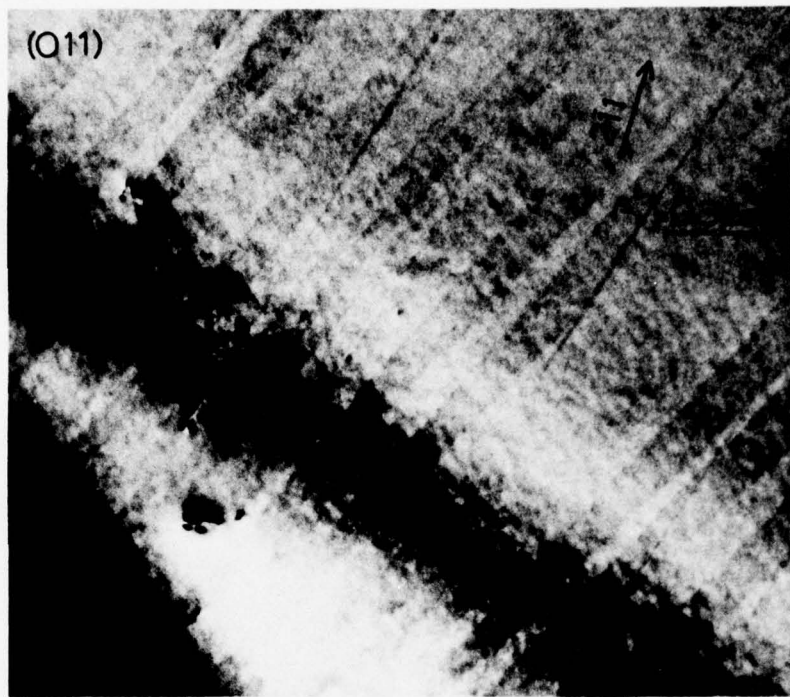


Figure 6. The geometry of the TEM samples used in this investigation. In some of the experiments the normal oxide surface layer was replaced with a thin layer of palladium.

Figure 7. Transmission micrograph of a niobium sample immediately after electropolishing. Surface disturbances, due to the passage of dislocations, are visible. These "tracks" disappeared after only a few seconds of exposure to the electron beam.

Figure 8. SEM micrograph showing cracking of specimens due to a high flux of hydrogen during electrolytic charging.



The Palladium-Niobium "composites" were thinned for TEM in the same manner as pure niobium, except that some portion of the palladium layer was protected (by laquer or plastic holder) from acid attack. (Figure 6). The amount of final electropolishing was minimized relative to the amount of jet polishing in order to prevent excessive H pickup during polishing. The aqua regia wash was not used for these specimens.

### 3.1.3 Gaseous Hydrogen Charging

The usual method of gaseous hydrogen charging for refractory metals<sup>(14)</sup> involves the heating of bulk samples to high temperatures (>600°C) in order to dissolve the surface oxide layer. Hydrogen gas is then introduced and the pressure adjusted to give the proper hydrogen equilibrium concentration<sup>(48)</sup>. As detailed in Appendix B, this method was found to be unsuitable for the charging of niobium thin foils because of oxygen pickup and subsequent oxide precipitation even in UHV environments. Furthermore, heating in the presence of purified hydrogen gas, at temperatures as low as 250°C, was sufficient to cause precipitation of metastable suboxides in the thinnest sections of the foil<sup>(49)</sup>.

Oxide precipitation during gaseous charging was avoided by the use of Pd coated samples. Hydrogen charging of the niobium foils could be accomplished at ambient temperatures because the palladium layer is much less of a permeation barrier to hydrogen entry than the oxide layer. A diffusion pumped, glass vacuum system was used for this charging procedure. Since the palladium coating effectively purified the incoming H<sub>2</sub> gas, commercial hydrogen gas could be used. Samples were quickly removed from this system and immersed in

mercury to poison the palladium layer and trap hydrogen in the sample. The hydrogen concentration was controlled by varying the  $H_2$  pressure and time of exposure (Figures 9 and 10). At  $P_{H_2} \leq 1$  atmosphere, concentrations of  $H/Nb \leq 1$  could be obtained with this method.

### 3.1.4 Electrolytic Charging of Niobium

Many investigators of hydrogen in niobium have employed cathodic charging techniques using solutions containing  $H_2SO_4$  or  $H_3PO_4$ . The general observation is that this technique does not yield predictable hydrogen concentrations. That observation is confirmed in this work. Several thin foil samples charged equal current densities for equal times showed widely varying concentrations. Most of the current supplied to the sample goes to the creation of gaseous hydrogen in the reaction  $2H^+ (\text{solution}) \rightarrow H_2$  (bubbles). Only a small and apparently uncontrollable amount of hydrogen penetrates the oxide layer and enters the niobium sample. These difficulties were surmounted by the use of palladium coated samples<sup>(47)</sup>.

Cathodic charging of palladium coated niobium samples was performed in 85% reagent grade orthophosphoric acid at temperatures of 20°C to 150°C. A 1 sq. in. stainless steel cathode was used. The higher charging temperatures (110°C-150°C) were used whenever it was desirable to avoid charging through the  $\alpha + \beta$  region of the Nb-H phase diagram. Palladium coated samples were usually immersed in mercury and aqua regia after charging to trap the hydrogen in the specimens. All samples were rinsed in water, acetone and methanol and dried with a cool air stream after charging.

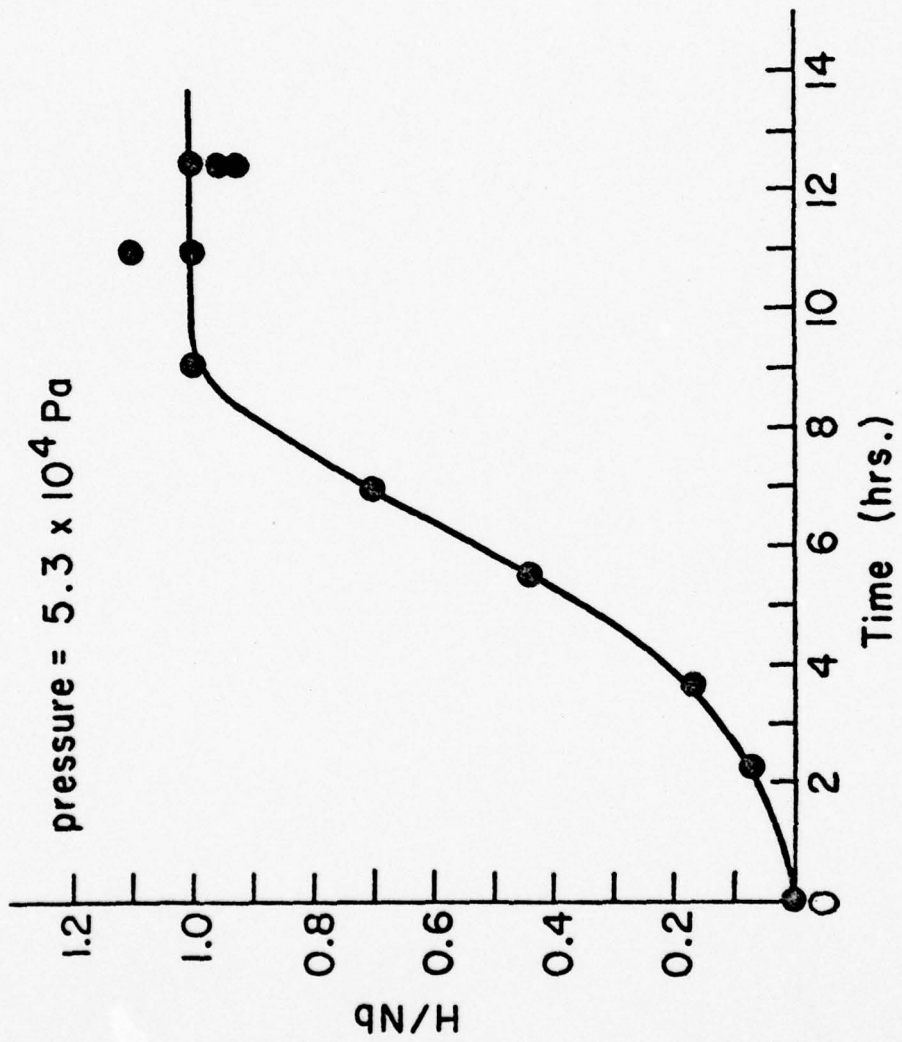


Figure 9. Typical calibration curve of concentration vs. time of exposure for palladium coated samples and constant  $P_{H_2}$ .

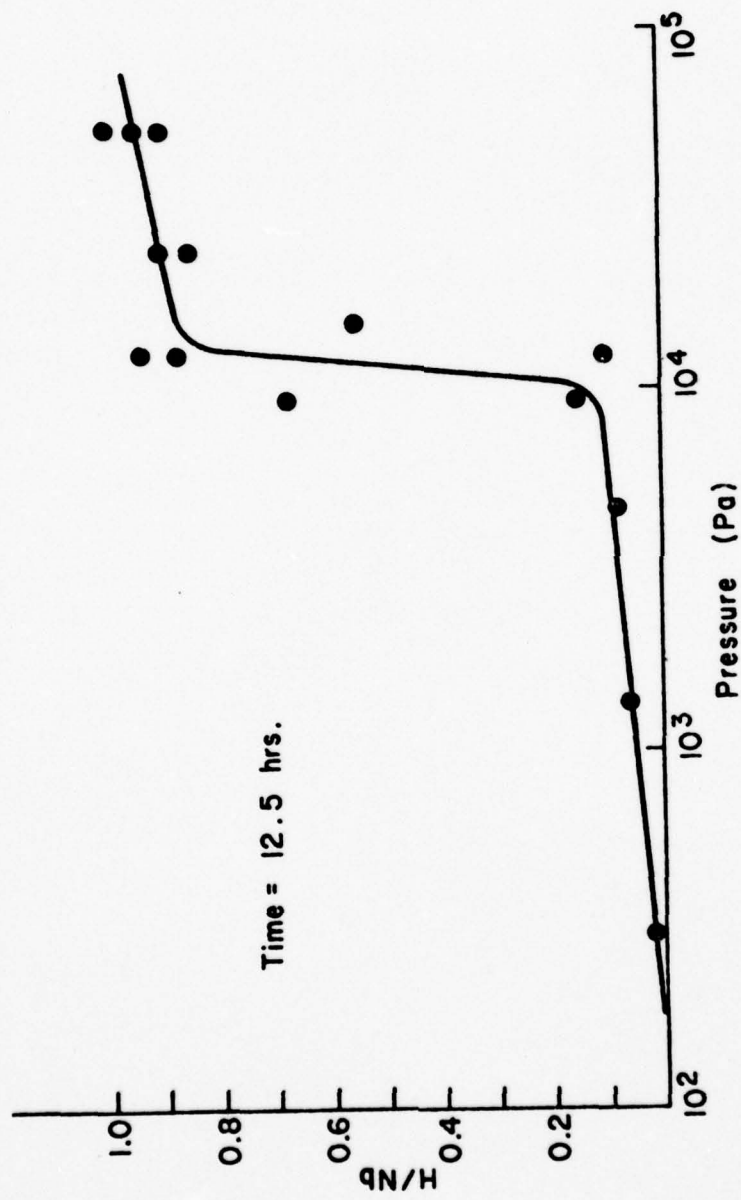


Figure 10. A typical calibration curve of concentration vs.  $P_{H_2}$  for palladium coated samples at constant exposure time.

Reliable hydrogen concentrations up to  $H/Nb=0.60$  could be obtained using this method. During electrolytic charging at low current densities ( $<10 \text{ mA/cm}^2$ ) no formation of  $H_2$  bubbles was observed at the sample surface.

The amount of hydrogen uptake could be accurately controlled by charging current and time (Figure 11) following Faraday's Law  $n_H = Fq$  where  $n_H$  is the number of moles of hydrogen,  $q$  is the total charge transferred, and  $F$  is Faraday's constant 96516 coulombs/mole. This result indicates that all of the hydrogen reduced at the surface, enters the sample.

For concentrations above  $H/Nb=0.60$ , some bubble formation occurred and the actual concentrations deviated from those predicted. However, samples with hydrogen concentrations as high as  $H/Nb=1.07$  were obtained, with less reliability, using high current densities ( $0.2\text{A/cm}^2$  to  $1.0\text{A/cm}^2$ ). Cracking due to high hydrogen fluxes (Figure 8) could be avoided by charging to  $H/Nb=0.60$  at low current densities and then completing the charging at high current densities. The cathodic charging technique is therefore applicable to charging bulk or thin samples to a wide range of compositions with no contaminant pickup.

### 3.2 Electron Microscopy Studies

Microstructural and electron diffraction studies were carried out using a JEOL 200B transmission electron microscope equipped with a side entry  $\pm 60^\circ$  goniometer, scanning-transmission, and supplemental pumping to minimize contamination. A single tilt heating stage, single tilt cooling stage ( $-180^\circ\text{C}$ ) and room temperature double-tilt and tilt-rotate stages were used in this work. In addition a tilt-rotate cooling stage was designed and constructed. This gas cooled holder was used for experiments between room temperature and  $-70^\circ\text{C}$  and allowed control of the specimen temperature in this range.

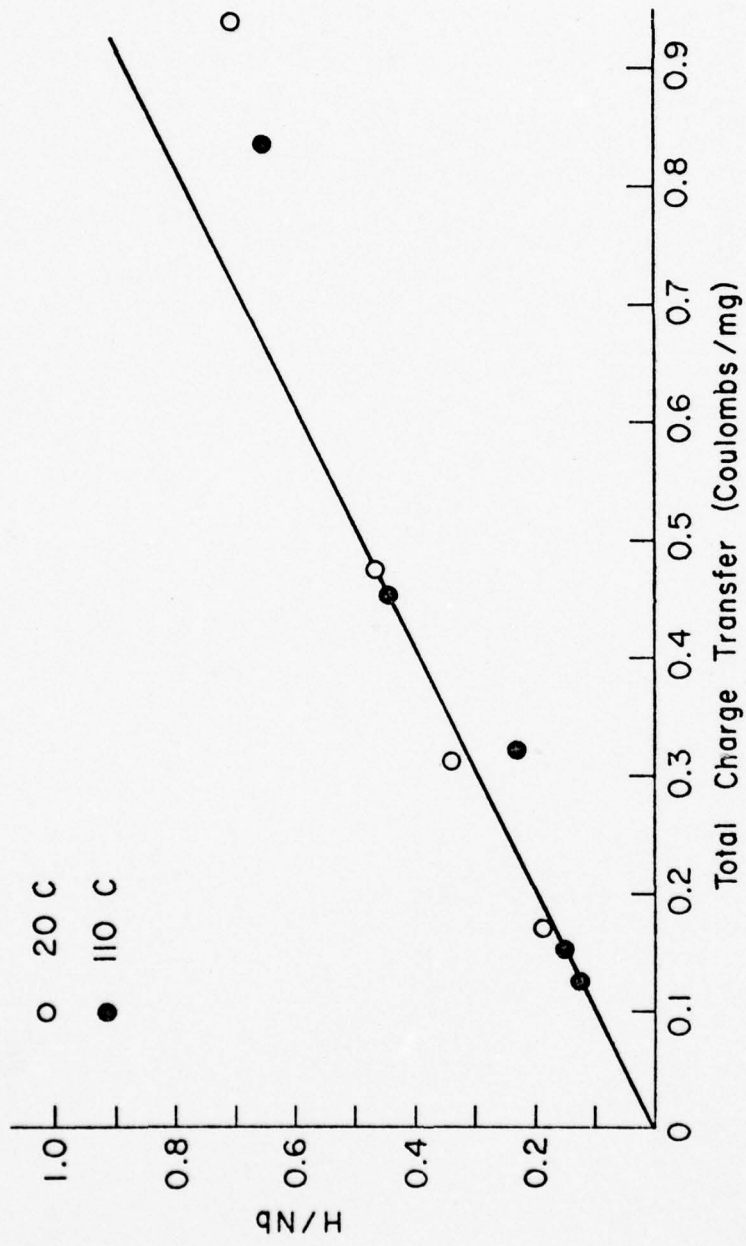


Figure 11. Concentration vs. total charge transferred for electrolytic charging of palladium coated niobium samples. The solid line is the result predicted by Faraday's law.

## 4.0 RESULTS AND DISCUSSION

### 4.1 Hydrides at Low Hydrogen Concentrations

#### 4.1.1 TEM Studies of Precipitation and Dissolution

Thinned TEM samples containing 0.1 to 2.0 atomic percent hydrogen were rapidly cooled in liquid nitrogen and then warmed to room temperature. The dislocation remnants of precipitation and dissolution were observed. The structures (Figures 12-14) consisted of approximately spherical volumes of high density dislocation tangles, 1 to  $2\mu\text{m}$  in diameter, surrounded by dislocation loops emitted in  $\langle 111 \rangle$  directions. The dislocation loops were shown to have  $\frac{1}{2} \langle 111 \rangle$  Burgers vectors in agreement with Schober<sup>(9)</sup>. Several of these loops were analyzed using "inside-outside" contrast techniques<sup>(50)</sup> and were shown to be interstitial prismatic loops.

In order to study the actual hydride precipitation and to observe any differences between precipitation in thin and thick foil areas, hydrogen charged samples were cooled *in situ* at rates of 3 to 20 degrees C/minute. Hydride precipitation did not, however, occur as discrete particles, but instead, all of the hydride formed as a highly deformed ring around the central perforation in the thinnest portion of the foil (Figure 15). Two beam diffraction conditions could not be attained in this deformed area but  $\beta$  superlattice spots were in evidence. Attempts were made to "innoculate" the specimen with a distribution of nucleation sites produced by rapidly quenching to form small hydrides followed by dissolution. On slow cooling, following this treatment, the *in situ* slow cooled hydride still precipitated only in the thinnest sections, and nucleation occurred only at the quenched in nucleation sites nearest the central perforation.

Figure 12A and B. The prismatic loops and dislocation tangles generated during the precipitation and dissolution of fast cooled hydrides.

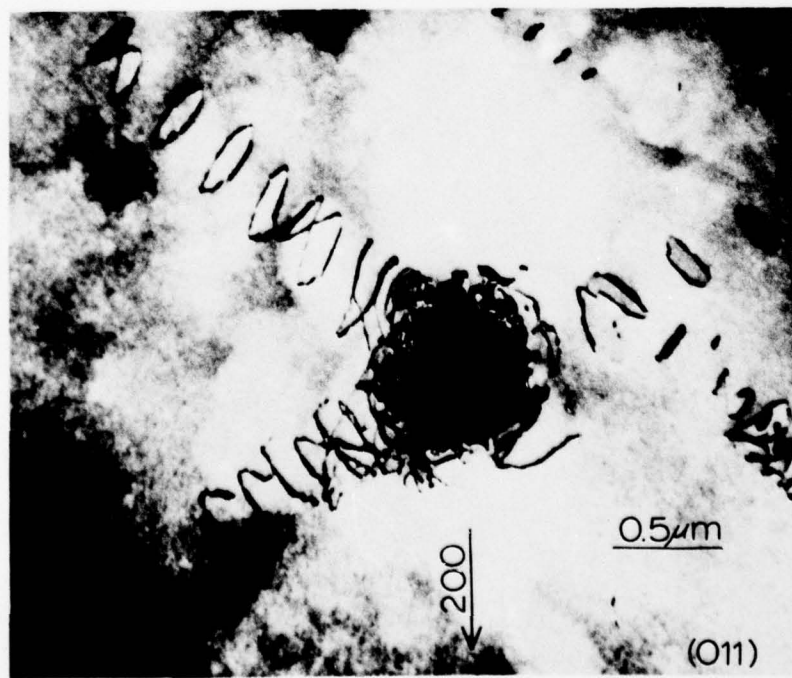
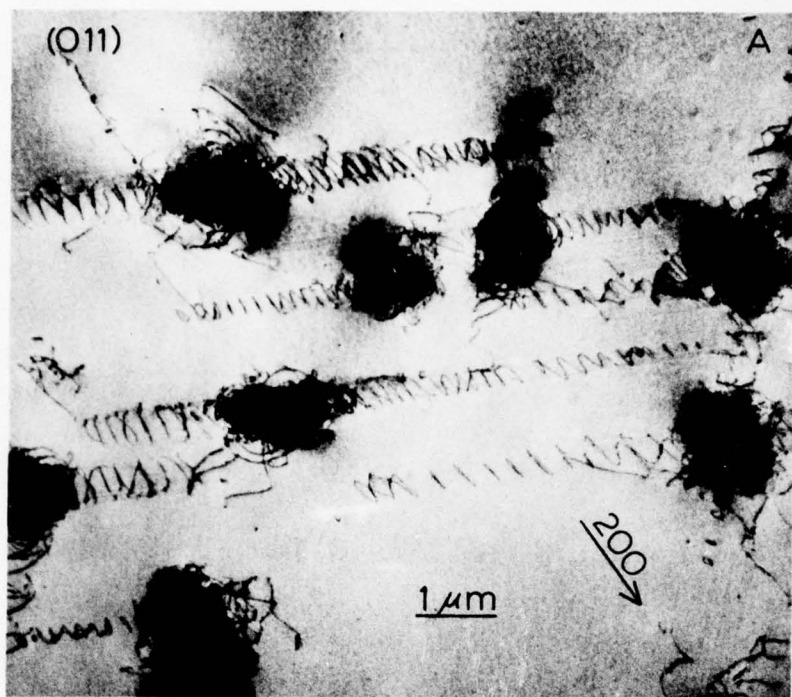


Figure 13. High magnification micrograph of interstitial prismatic loops associated with the precipitation of  $\beta$  hydride.

Figure 14. The dislocation remnants of a large hydride which had nucleated on a low angle grain boundary.

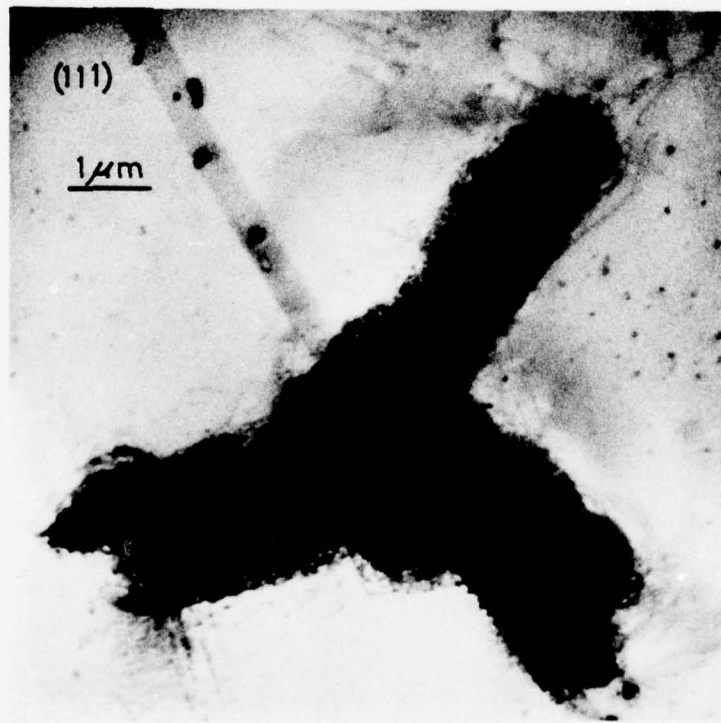
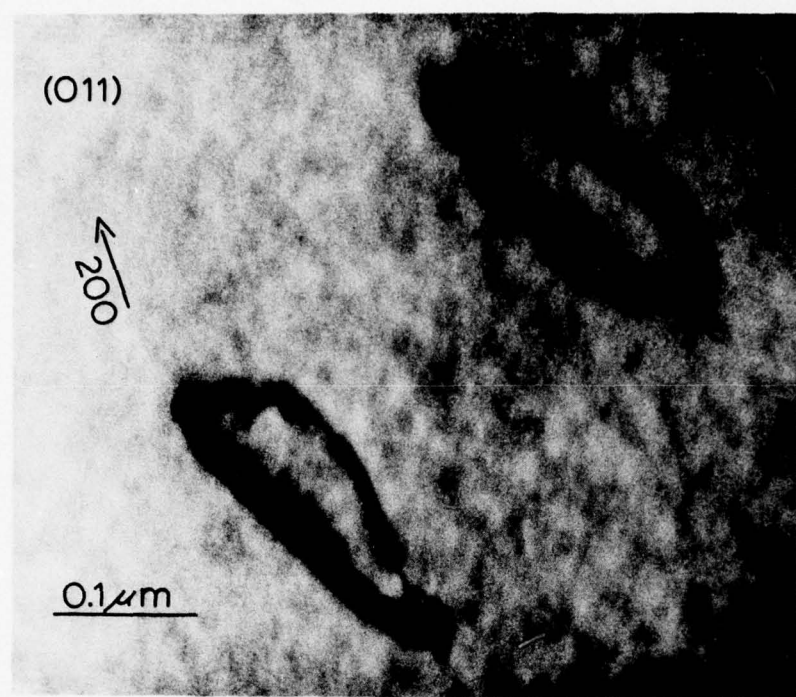
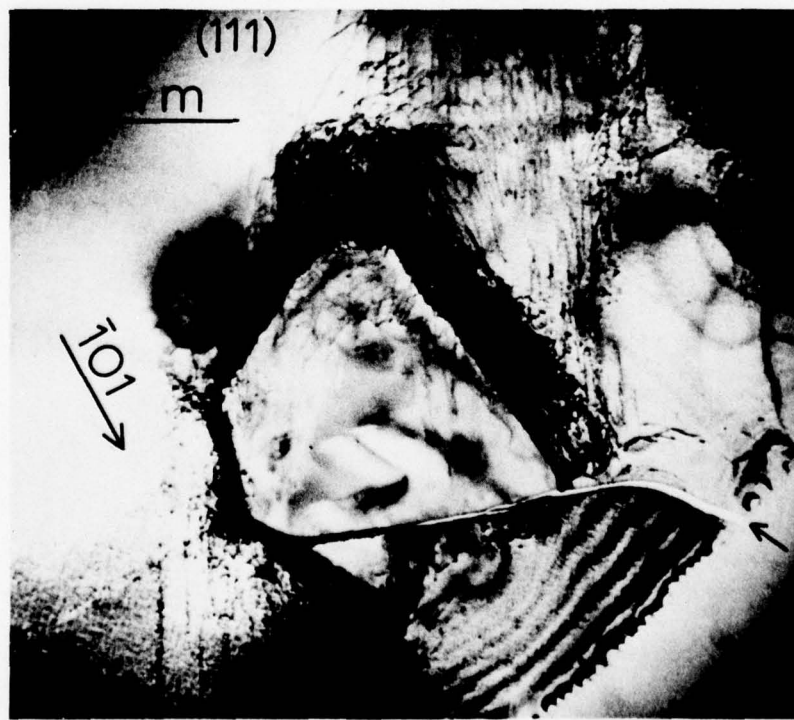
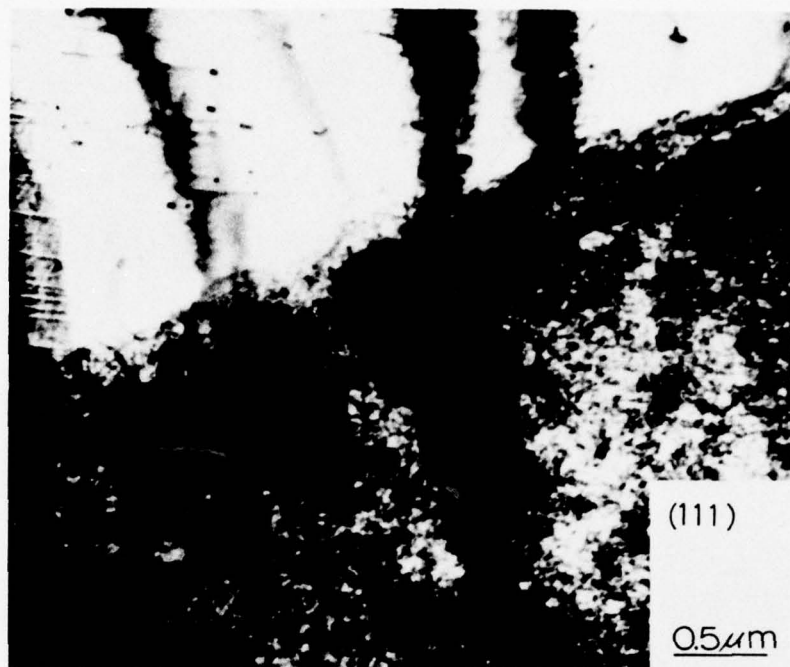


Figure 15. The preferential precipitation of hydride in the thinnest areas of the foil after slow cooling to  $-126^{\circ}\text{C}$  for an  $\text{NbH}_{0.01}$  alloy. The hydride is in the lower half of the micrograph.

Figure 16. Cracking near the edge of a TEM foil in the vicinity of a hydride particle.  $\text{H/Nb}=0.1$ . The crack is indicated by an arrow.



The precipitation of  $\beta$  hydride from solid solution is accompanied by a volume expansion of approximately 12 percent. As discussed by Birnbaum, et al.<sup>(16)</sup>, this expansion is accommodated by elastic and plastic work done on the matrix and on the hydride. The free energy for precipitation  $\Delta G_{\alpha \rightarrow \beta}$  is then

$$\Delta G_{\alpha \rightarrow \beta} = \Delta G(\text{chemical}) + \Delta G(\text{plastic}) + \Delta G(\text{elastic}) + \Delta G(\text{surface}). \quad (1)$$

where  $\Delta G(\text{chemical})$  is the free energy for precipitation in the absence of constraint by the matrix,  $\Delta G(\text{elastic})$  is the elastic work done in the matrix and in the precipitate,  $\Delta G(\text{surface})$  is the energy to create the surface between precipitate and matrix, and  $\Delta G(\text{plastic})$  is the plastic work done in the matrix.

Similarly, a volume decrease of about 12% is required on dissolution of the hydride. Elastic, plastic, and surface energy terms must therefore be accounted for during dissolution.

For precipitation of the hydride, the plastic work term,  $\Delta G(\text{plastic})$ , is the energy required to create prismatic interstitial dislocation loops at the  $\alpha$ - $\beta$  interface and to move these loops into the matrix. Thus matter is transported away from the growing precipitate. As noted by Brown, et al.<sup>(51)</sup>, however, dislocation loops will not be observed unless the stresses at the  $\alpha$ - $\beta$  interface are sufficiently large to nucleate dislocation loops. The maximum stress at the interface is independent of precipitate size and directly proportional to the magnitude of the dilatational strain,  $e^T$ , associated with the phase transformation. At the interface of an ellipsoidal particle, for example<sup>(52)</sup>, the maximum shear stress,  $\tau_S$ , is:

$$\sigma_s = 2\mu e^T / 3 \quad (2)$$

where  $\mu$  is the shear modulus. The shear stress  $\sigma_s$  must be greater than the theoretical shear stress in order for dislocation loop punching to occur.

In the case of rapid cooling to 77°K, the plastic accommodation takes the form of prismatic interstitial dislocation loops which serve to move material away from the precipitate interface. Hydrogen diffusion is too slow, relative to the cooling rate, to allow significant redistribution of the hydrogen atoms. In this case the hydride nucleation appears to occur homogeneously and foil thickness has little effect. For precipitation during slow cooling, hydrogen diffusion is rapid enough to allow hydrogen redistribution and foil thickness has a large effect. In close proximity to the surfaces, the necessary accommodation terms  $\Delta G(\text{plastic}) + \Delta G(\text{elastic})$  are not as large as in the fully constrained case since no constraint is placed on a precipitate by a free surface. Less undercooling is necessary then and the solvus temperature in thin sections approaches the equilibrium, i.e., unconstrained, solvus temperature. The  $\alpha-\beta$  solvus temperature is highest in the thinnest regions of the sample and therefore on slow cooling massive precipitates form first in the thinnest section of the specimen.

An attempt was made to approximately calculate the magnitude of the plastic work term,  $\Delta G(\text{plastic})$ , from the number and position of prismatic interstitial loops seen in the accompanying micrographs. The  $\Delta G(\text{plastic})$  consists primarily of loop formation energy and the energy of loop motion away from the precipitate. These terms can be written:

$$\Delta G(\text{plastic}) = \sum_i \frac{R_i \mu b^2}{2(1-\nu)} \left( \ln \frac{4R_i}{\rho} \right) - 1 + \sum_i 2\pi R_i \nu b d_i \quad (3)$$

where  $\mu$  is the shear modulus,  $b$  is the Burgers' vector,  $R_i$  is the radius of the  $i^{\text{th}}$  dislocation,  $d_i$  is the distance the  $i^{\text{th}}$  dislocation has moved from the precipitate,  $\mu$  is the shear modulus,  $\nu$  is Poisson's ratio, and  $\rho$  is about  $b/8$ . The summation is carried out over all of the dislocation loops. Using Equation 3 and the information obtained from micrographs, a plastic work term of 50 cal/mole is estimated. This value is of the same magnitude but less than the value of approximately 300 cal/mole estimated by Birnbaum, et al. (16). The 50 cal/mole calculated here is a low value because of three factors.

1. The calculation does not take into account the possible generation of loops on slip systems which allow annihilation of dislocation loops at the surface.
2. The energy of the tangle of interfacial dislocations at the precipitate surface has not been included in the calculation.
3. The adjacent free surface alleviates the need for some of the plastic accommodation thus lowering the magnitude of  $\Delta G(\text{plastic})$  in the thin foils relative to bulk specimens.

The hydride dissolution process was studied on slow heating after precipitation. Samples were cathodically charged at  $110^{\circ}\text{C}$  to 10 atomic percent H and quenched immediately into liquid nitrogen. This yielded a room temperature distribution of hydride precipitates ranging in size from  $4-5 \mu\text{m}$  in

diameter in thinnest foil sections to  $1-2\text{ }\mu\text{m}$  in thick foil sections. The morphology consisted of an undeformed multidomain hydride surrounded by a highly deformed interface and by prismatic dislocation loops (Figure 17). Microcracks leading from the central perforation to adjacent hydrides were often observed (Figure 16). The precipitates were heated in situ and the dissolution process was observed. As the hydride particles decreased in size, dislocation having  $a/2<111>$  Burgers vectors were observed to precede the  $\alpha$ - $\beta$  interface into the interior of the  $\beta$  precipitate. The process continued until the entire precipitate filled with dislocation tangles (Figures 18-21). The actual  $\alpha$ - $\beta$  interface could not usually be observed. Dislocation motion occurred quite readily within existing hydrides and the  $\beta$  domain boundaries did not appear to hinder this motion.

It is theoretically possible for the volume accommodation which accompanies hydride dissolution to be accomplished by the punching of vacancy prismatic dislocation loops into the  $\alpha$  matrix or by the absorption of existing prismatic interstitial loops at the  $\alpha$ - $\beta$  interface. Neither of these two mechanisms was observed. Presumably interactions between the existing prismatic interstitial dislocations inhibits the absorption of interstitial loops during reversion. The lack of plastic accommodation by means of prismatic vacancy loop punching in the  $\alpha$  matrix may also be caused by the presence of dislocation tangles at the  $\alpha$ - $\beta$  interface.

The plastic accommodation of the volume change for the  $\beta \rightarrow \alpha$  transformation occurred almost entirely within the dissolving hydrides by motion of  $a/2<111>$  dislocations. These dislocations were not loops and therefore could not be

Figure 17. A portion of a large hydride precipitate formed on quenching to -196°C from a charging temperature of +110°C. The foil composition is NbH<sub>0.1</sub>. The hydride contains little deformation and domain boundaries are visible. The interface is highly deformed and plastic deformation extends into the matrix.



Figure 18. A hydride precipitate formed in a thick foil area by quenching to -196°C from a charging temperature of +110°C. Foil composition H/Nb=0.10.

Figure 19. Same area as above after heating to 60°C to dissolve the hydride precipitate.

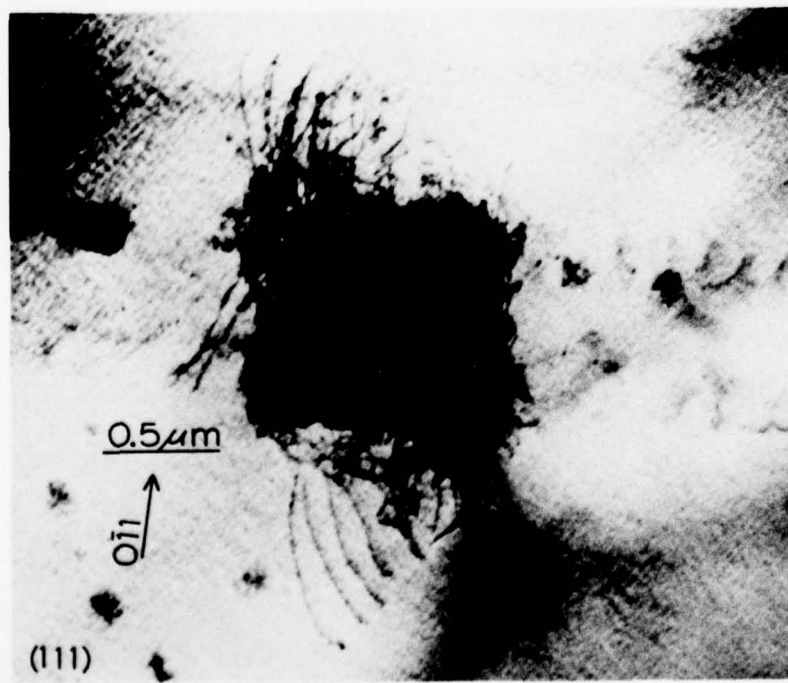
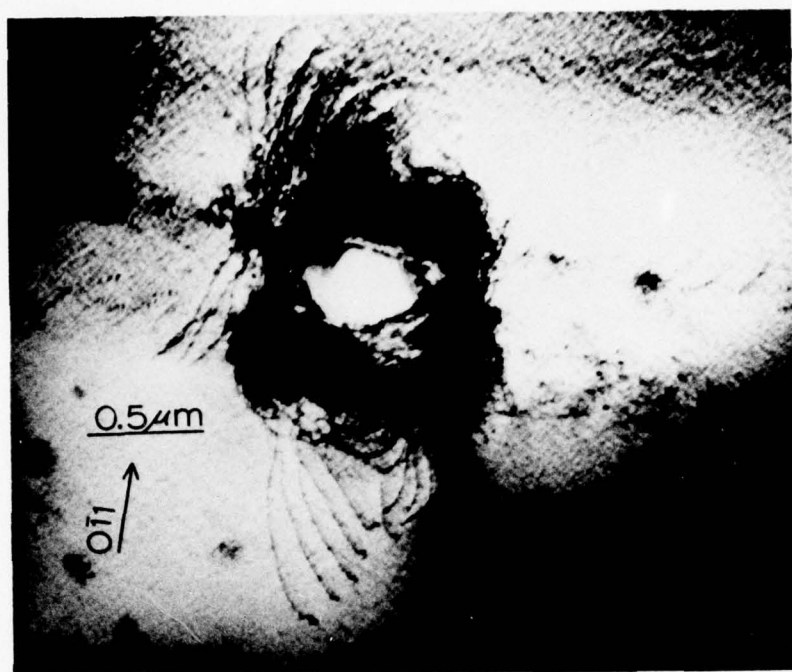
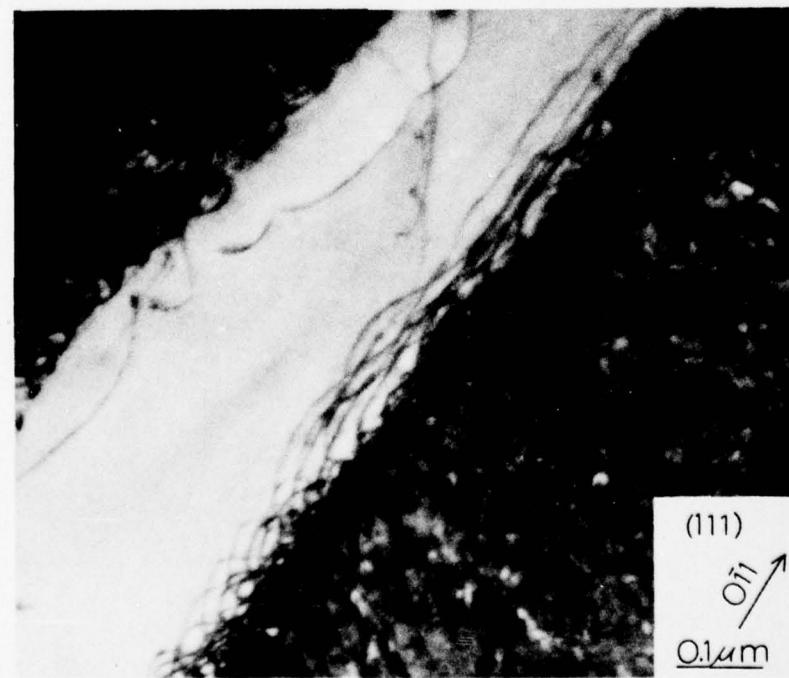


Figure 20. A large hydride precipitate undergoing dissolution at 60°C.

Figure 21. Same as figure above at higher magnification. Dislocations are in motion towards the center of the precipitate.  
 $H/Nb=0.10$ .



analyzed for interstitial or vacancy character. They may be partial prismatic loops which intersect the foil surfaces. Alternatively, if they are shear dislocations, their correlated motion could have the effect of moving material towards the center of the  $\beta$  hydride as reversion occurs. In rare cases the dislocation tangle was sparse enough to permit observation of the  $\alpha$ - $\beta$  interface. Some additional dislocation debris is left behind when the interface passes through an area and some plastic accommodation may occur in this manner.

The analysis was complicated by the unavoidable motion of the dislocations during observation. Since the dislocations were observed within partially dissolved hydride, even small amounts of electron beam heating caused further dissolution and additional stresses which induced dislocation motion.

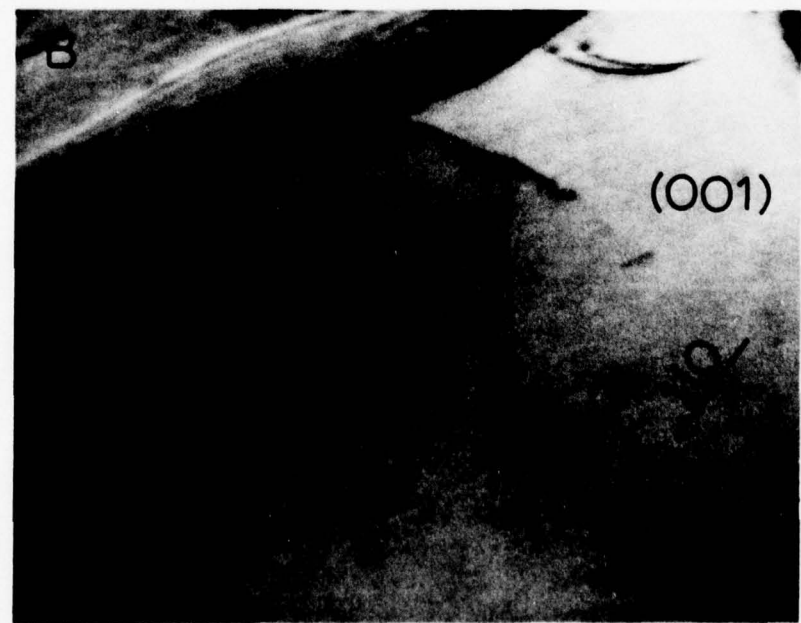
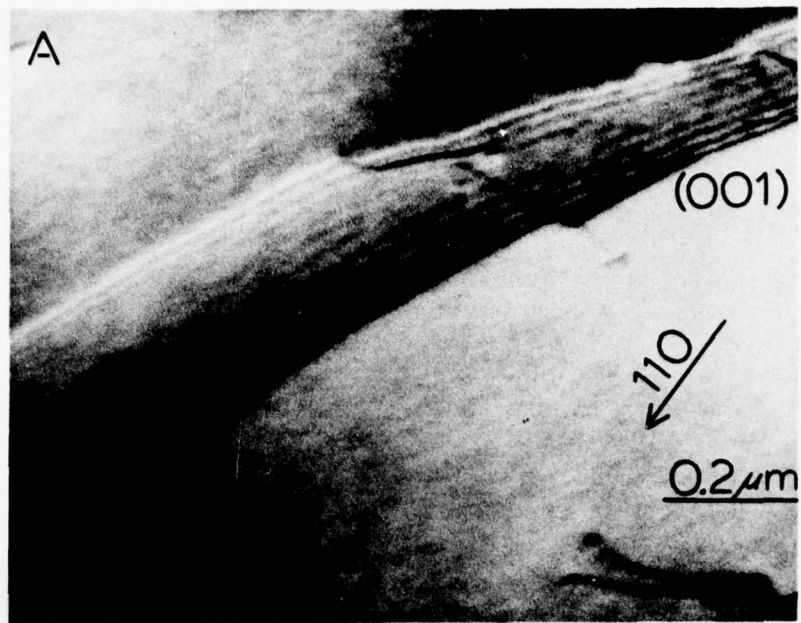
#### 4.1.2 Beam Heating Effects

During in situ cooling of low H concentration samples, precipitation of  $\beta$  hydride always occurred first in thin areas not illuminated by the electron beam. As a consequence, an area several microns in diameter could be kept free of hydride until the electron beam was removed. At normal 200 KV operation, the electron beam bombardment had no effect on already existing hydrides, except very near the solvus temperature. A lower accelerating voltage of 100 KV or operation without a condenser aperture caused rapid movement of domain boundaries within hydrides (Figure 22).

These effects are attributable to electron beam heating of a small area of the sample and the concomitant stresses. Thermal gradients are created within the specimen and mobile solutes having a positive heat of transport,

Figure 22A. A domain boundary within a hydride precipitate. The micrograph was taken at 100 KV with a highly defocused condenser lens.

Figure 22B. Micrograph taken after brief exposure to a 100 KV beam with a normally focused condenser lens. Note the movement of the boundary due to beam heating.



such as hydrogen<sup>(53)</sup>, will tend to migrate towards the cooler areas of the specimen. Concentration gradients are thus established which make precipitation unlikely in the area under observation. Wipf<sup>(53)</sup> has discussed thermal transport of hydrogen solutes, and his phenomenological treatment is outlined here. For steady state, the flux of H due to thermal drift is balanced by the flux due to the induced concentration gradient

$$J \text{ (Diffusion)} = J \text{ (Drift)} \quad (4)$$

$$D \text{ grad } C = -CMQ^* \frac{\text{grad } T}{T} \quad (5)$$

where D is the diffusion coefficient of H in Nb, C is the concentration of H, M is the mobility of hydrogen and T is the temperature.  $Q^*$  is called the "heat of transport" and this quantity includes not only the activation barrier for H motion, but also the effects of electrons, holes, and lattice phonons on the migrating hydrogen atoms. The approximation can be made that:

$$D = C \frac{\partial M}{\partial C} = kT M \quad (6)$$

Then combining the two previous equations:

$$\text{grad } C \approx \frac{-CQ^*}{kT^2} \text{ grad } T \quad (7)$$

For a concentration of 0.001 the value of  $Q^*$  has been reported to be 0.15 eV and the hydride solvus temperature reported to be 173°K.

The beam heating in a TEM cooling stage can be estimated<sup>(54)</sup> by:

$$\Delta T = \left( \frac{\Delta E}{t} \right) \frac{I}{4K\pi} \left[ 5.771 + 2 \ln \frac{R}{\alpha} \right] \quad (8)$$

where R is the distance to a thermal contact between sample and stage, I is the total beam current hitting the sample, K is the thermal conductivity of the sample, t is the sample thickness at the point of irradiation and  $\alpha = \ln \sqrt{2}/2 \cdot H$ , where H is the diameter at half maximum of the gaussian beam profile (H taken here to be  $2\mu\text{m}$ ). The energy loss to the sample by one electron,  $\Delta E$ , can be calculated approximately<sup>(55)</sup> from the equation:

$$E(0)^2 - E(t)^2 = 2\pi e^4 \left[ N\rho/a \right] Zt \quad (9)$$

where A = atomic weight, Z = atomic number,  $\rho$  = density, N = Avogadro's number and E(t) is the electron beam energy after passing through material of thickness t. Using the appropriate constants for niobium,  $\Delta E/t$  is  $0.75 \times 10^6$  eV/cm for  $E(0) = 200$  KeV. Zalusec<sup>(56)</sup> has reported that at 200 KeV for the JEOL 200B instrument,  $I = 3.7 \times 10^{-7}$  amperes ( $2.3 \times 10^{12}$  electrons/second). Then by Equation 8,  $\Delta T$ , between the irradiated area and the supporting stage, is approximately  $7^\circ\text{K}$ . Which in turn, by Equation 7 gives an estimated concentration difference (at  $C(\text{average}) = 10^{-3}$  and  $T = 173^\circ\text{K}$ ) of  $\Delta C = 4 \times 10^{-4}$ . Electron beam heating has a significant effect upon hydrogen concentration in solid solutions and can be expected to influence the precipitate distribution.

#### 4.1.3 Trapping Effects

Several investigators<sup>(57,58)</sup>, using internal friction and resistivity measurements, have found evidence for trapping of hydrogen by other interstitials. Oxygen-hydrogen and nitrogen-hydrogen bound pairs are believed to form in niobium with a binding enthalpy of 0.08<sup>(59)</sup> and 0.12 eV/atom<sup>(58)</sup>, respectively.

There has been investigation of and controversy about the effect of O and N additions on the hydride solvus in the Group Vb refractory metals. Chang and Wert<sup>(60)</sup> and Westlake and Ockers<sup>(61)</sup> both found shifts in the solvus to lower temperatures for oxygen additions in the Vanadium-Hydrogen system, but they differ on the magnitude of the effect. Lecocq<sup>(62)</sup> found no effect of oxygen on the tantalum hydride solvus. Pfeifer and Wipf<sup>(59)</sup> and Chen<sup>(62)</sup> found solvus shifts and decreasing amounts of niobium hydride precipitation with O and N additions, respectively.

To demonstrate the effect of O and N interstitials upon hydride precipitation, TEM samples were made from Niobium sheet which had been doped with 0.27 atomic percent oxygen and 0.47 atomic percent nitrogen. These samples were then electrolytically charged to 0.1 and 0.7 atomic percent hydrogen, respectively. During subsequent *in situ* cooling to 77°K no hydride precipitation was observed in either foil. The hydrogen trapped at O or N is evidently not available for the hydride precipitation process in agreement with the measurements of Pfeifer and Wipf<sup>(59)</sup> and with Chen<sup>(62)</sup>. These observations support their conclusions that the amount of hydride precipitation decreases with increasing solute trap concentrations.

## 4.2 Low Temperature Phase Transformations

### 4.2.1 Transformations in Samples of H/Nb less than 0.70

At room temperature, a two phase mixture of  $\alpha$  solid solution and  $\beta$  hydride is stable for compositions between  $H/Nb=0.04$  and  $H/Nb=0.70$ . Thin foil samples were electrolytically charged at temperatures above  $110^{\circ}\text{C}$  and cooled quickly to ambient temperature. This charging technique successfully avoided the excessive amounts of plastic deformation that usually accompany the nucleation and growth of hydride particles in the  $\alpha+\beta$  region. In general, the entire electron transparent area transformed to a relatively undeformed  $\beta$  hydride. The  $\alpha$  solid solution was presumably confined to the thicker areas of the sample. This distribution is consistent with the volume increase on forming hydride as discussed in previous sections. Domain boundaries were in evidence throughout the structure (Figures 23-24) and  $\beta$  phase superlattice reflections were observed (Figures 25-29) at  $\{1\bar{2}\bar{1}\}$  as previously reported by Somenkov, et al.<sup>(20)</sup> and Schober, et al.<sup>(21)</sup>.

The specimens were cooled *in situ* and observations were made at 200 KV on cooling to and warming from  $-180^{\circ}\text{C}$ . The sequence of transformations on warming will be described here; no differences were found during cooling. The relations between these observations and those previously obtained at 100 KV will be discussed shortly.

Between  $-180^{\circ}\text{C}$  and  $-66^{\circ}\text{C}$  and stable hydride is  $\epsilon$ , which is based on the ordering of hydrogen vacancies on a specific subset of those tetrahedral sites allowed in the  $\beta$  structure (Figures 30-33). In this structure the interstitial sites in the subset labeled (ii) in Figure 33 have occupation probabilities of 1 while those in the subset labeled (i) have occupation probabilities

Figure 23. Domain boundaries in  $\beta$  hydride at room temperature.

Figure 24. Domain boundaries in a sample of composition  $H/Nb=0.79$  at room temperature. The alternating dark-light contrast of domains is caused by changes in diffraction conditions due the differing orientation of the three orthorhombic axes in each domain.

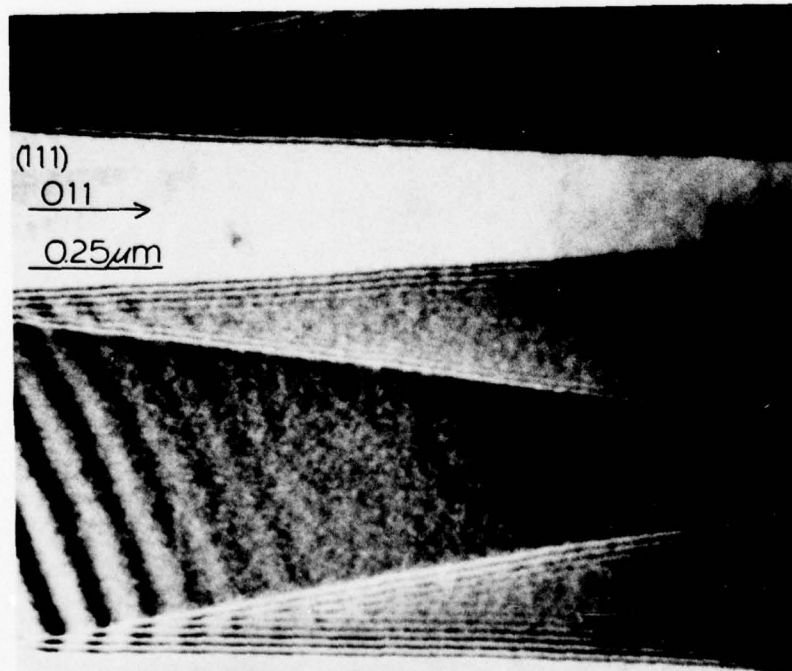
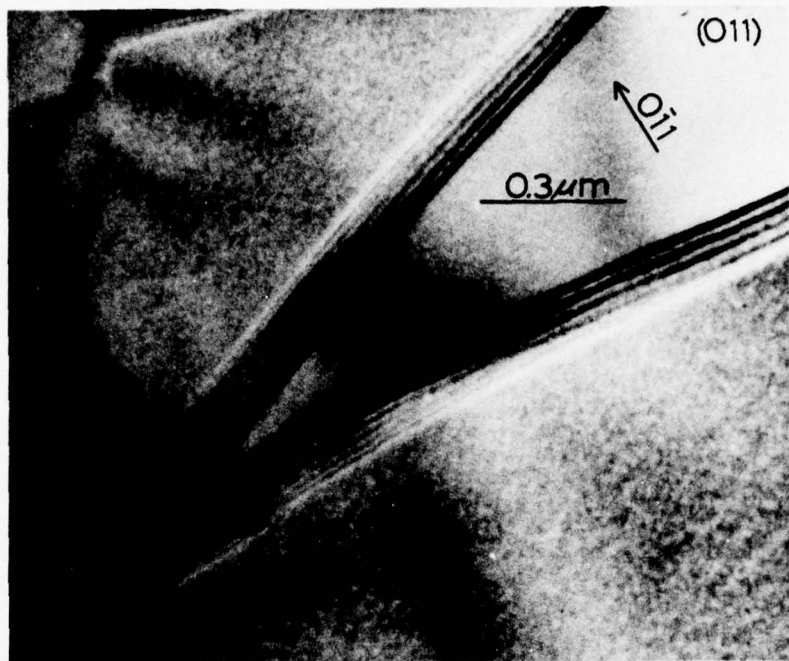


Figure 25. A (110) diffraction pattern showing  $(\frac{1}{2}\frac{1}{2}1)_c$   $\beta$  superlattice reflections. Sample composition is approximately H/Nb=0.70. Temperature is 20°C.

Figure 26. Scanning-Diffraction taken in the  $[1\bar{1}2]_c$  direction and showing the  $\beta$  superlattice spot at  $(\frac{1}{2}\frac{1}{2}1)_c$ . Intensities are on a Log scale.

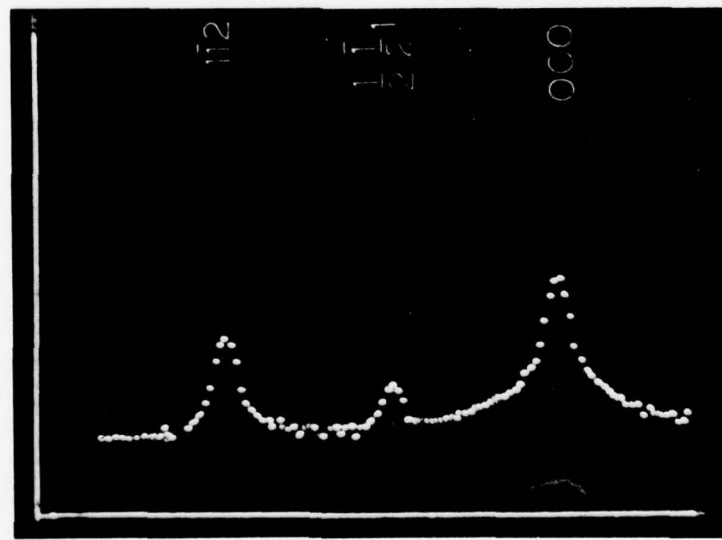
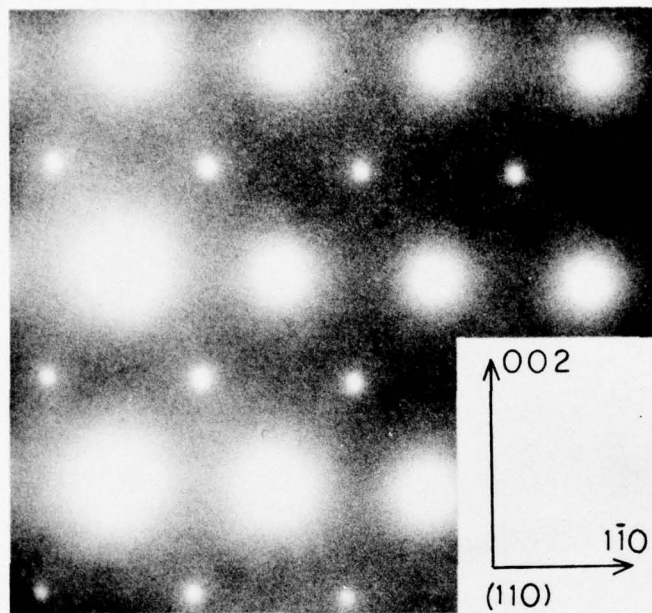


Figure 27. Bright field-Dark field pair of a single  $\beta$  domain. The dark field image is formed using the  $(\frac{1}{2}\frac{1}{2}1)_c$  superlattice reflection indicated.

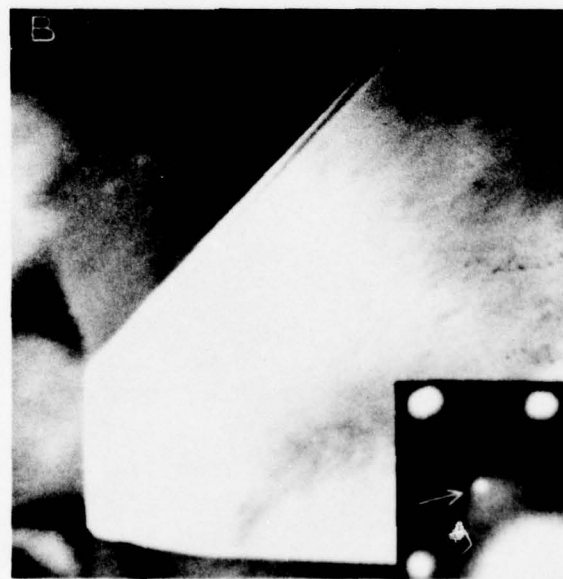
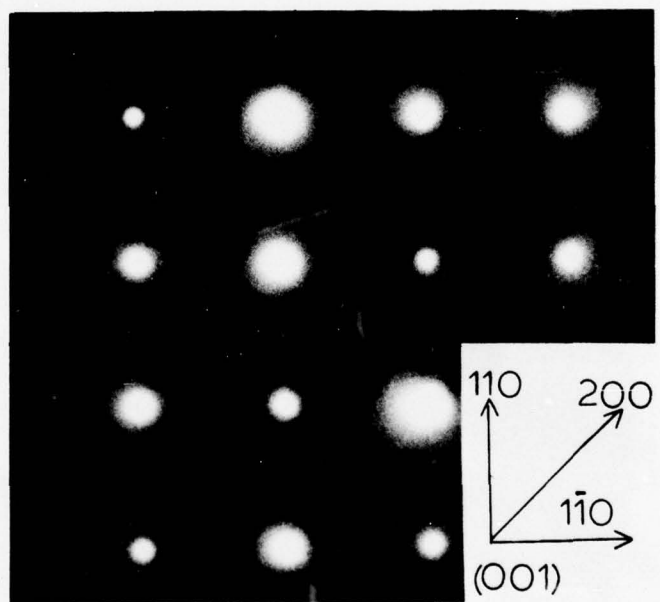


Figure 28. An  $\{001\}_c$  diffraction pattern at  $20^\circ\text{C}$  from  $\beta$  hydride in a sample of composition  $\text{H/Nb}=0.67$ . No superlattice reflections appear on any of the three  $\{001\}_c$  reciprocal sections in  $\beta$  hydride.



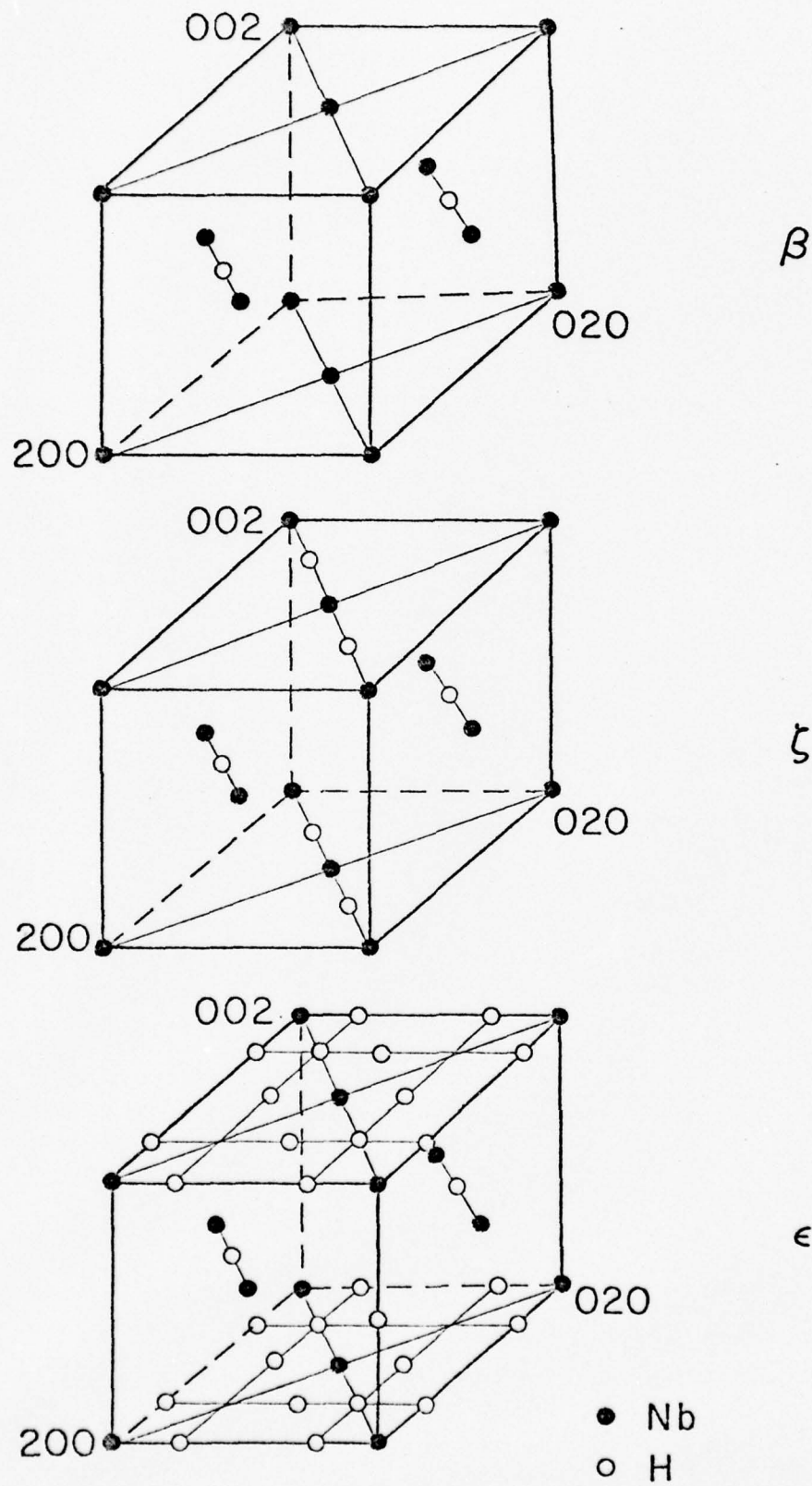
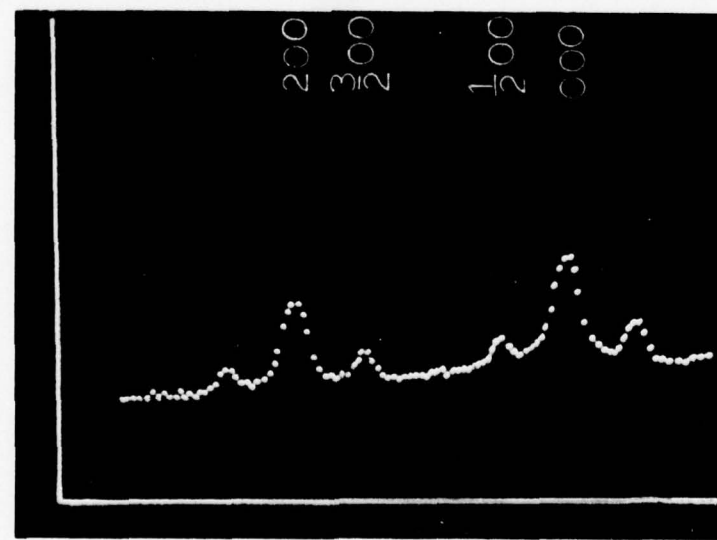
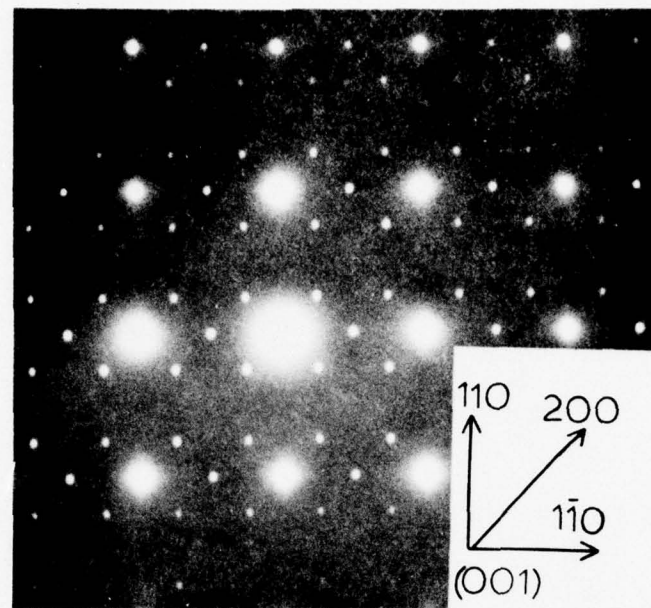


Figure 29. The reciprocal lattices of  $\beta$ ,  $\varsigma$  and  $\epsilon$  hydrides.

Figure 30. An  $(001)_c$  diffraction pattern taken at  $-78^\circ\text{C}$  from a sample of composition  $\text{H}/\text{Nb}=0.67$ . The superlattice reflections at  $(\frac{1}{2}\bar{2}0)_c$ ,  $(\frac{1}{2}00)_c$ , and  $(0\frac{1}{2}0)_c$  are due to a single  $\epsilon$  domain.

Figure 31. Scanning-Diffraction in the  $[200]_c$  direction taken from hydride. Note superlattice spots at  $(\frac{1}{2}00)_c$  and  $(\frac{3}{2}00)_c$ . Temperature is  $-180^\circ\text{C}$ .



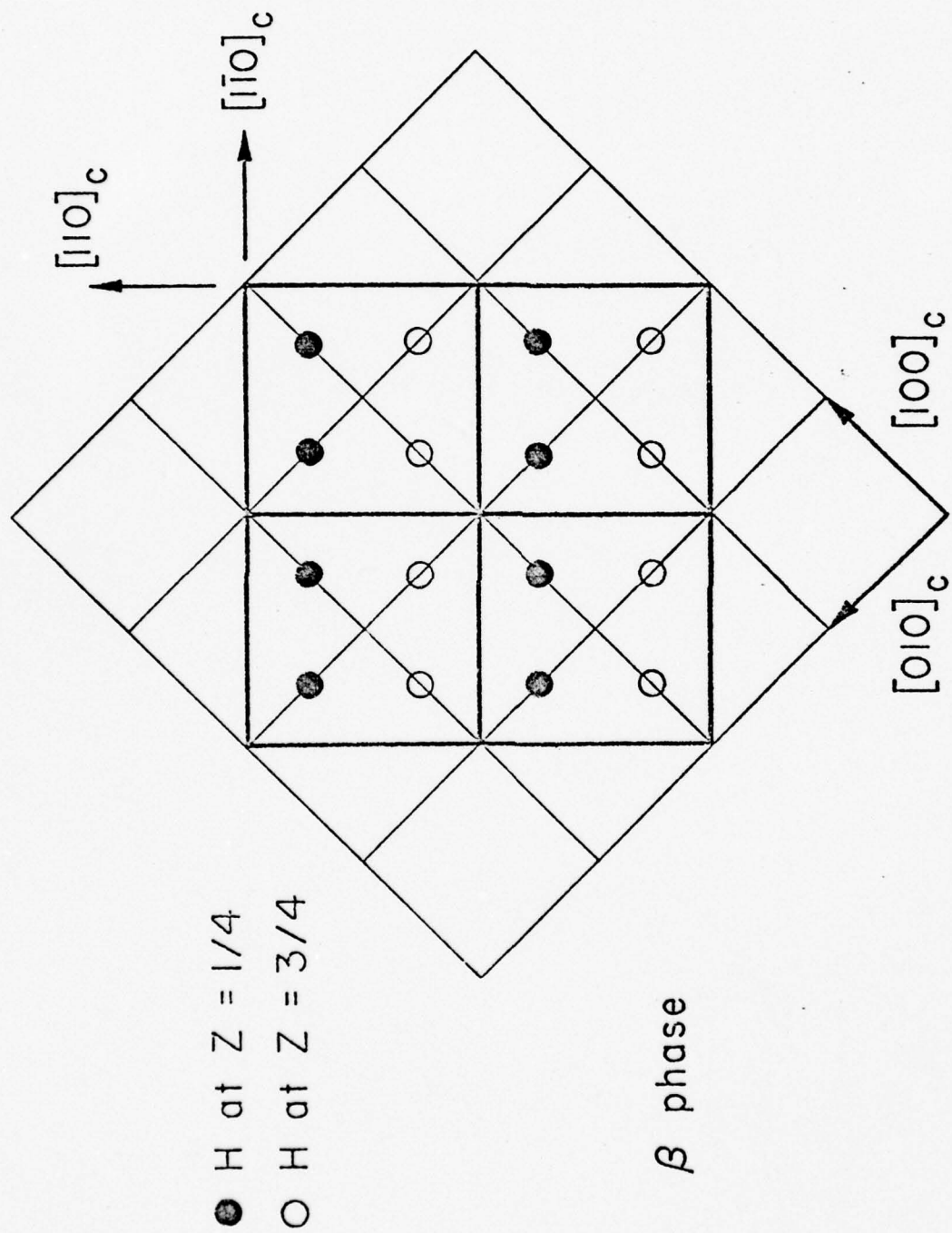


Figure 32. The structure of  $\beta$  hydride. Four  $\beta$  unit cells are shown. Occupation probability is 0.75 for all allowed interstitial sites at the composition  $H/Nb=0.75$ .

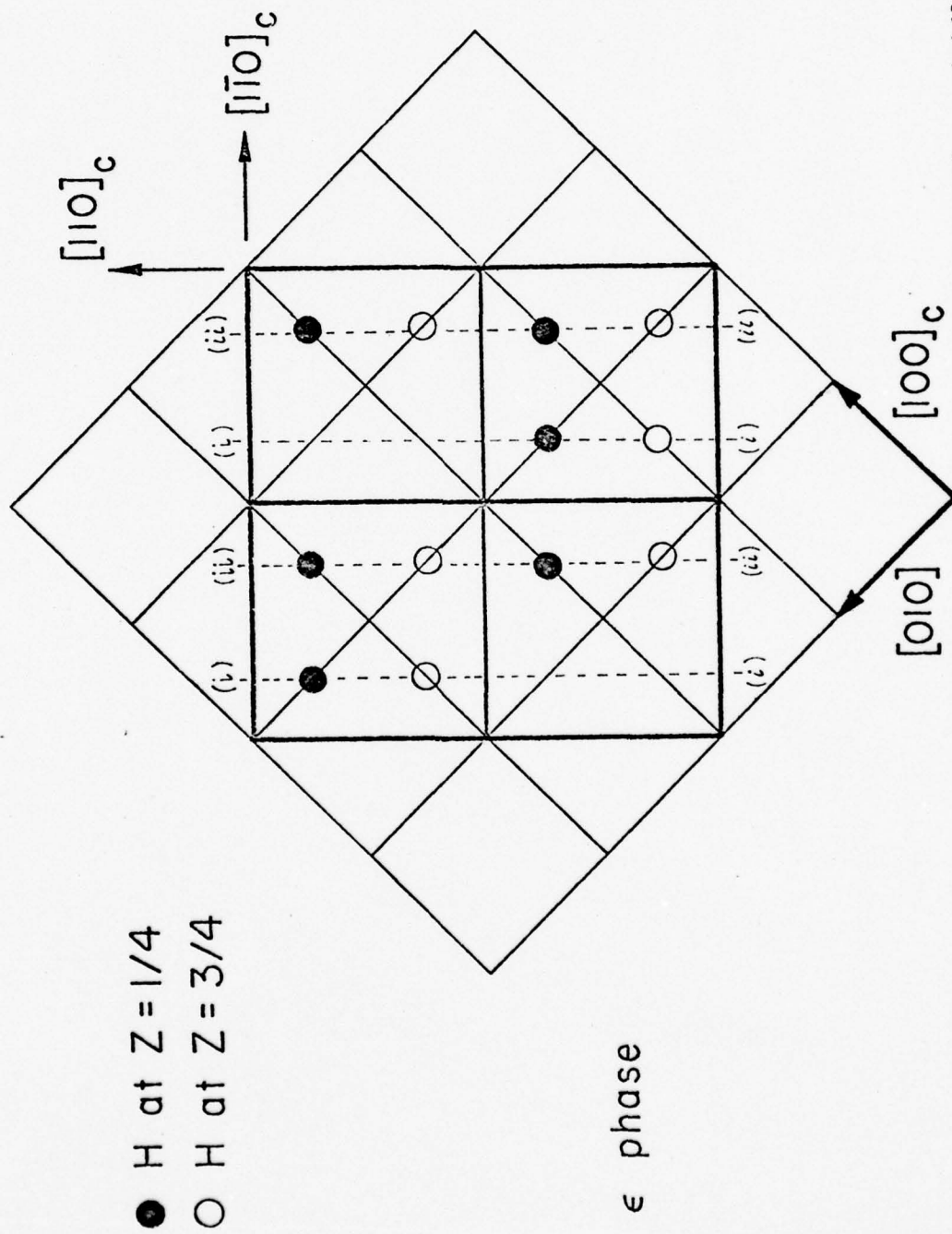


Figure 33. The structure of  $\epsilon$  hydride. Type (i) sites have an occupation probability of either 1 or 0, while type (ii) sites have an occupation probability of 1.

of either 1 or 0 as indicated. The  $\epsilon$  reciprocal lattice observed in this investigation (Figures 29-31) was the same as than seen by Somenkov, et al.<sup>(29)</sup> and Schober, et al.<sup>(9)</sup>. No morphological differences between the  $\beta$  and  $\epsilon$  phases were observed. In particular, the domain structure was the same for the  $\beta$  and  $\epsilon$  phases.

At  $-66^{\circ}\text{C}$  the superlattice reflections at  $\{1\bar{2}0\}_c$  greatly decreased in intensity and nearly disappeared. The superlattice reflections at  $(\bar{1}20)_c$  remained intense. The change in diffraction pattern occurred at approximately the temperature which was reported by Schober<sup>(9)</sup> to characterize the transformation from the  $\epsilon$  to the  $\zeta$  hydride structure (Figure 1). It has been suggested by Schober<sup>(63)</sup> that the  $\zeta$  phase, characterized by the  $(\bar{1}20)_c$  superlattice reflection, (Figure 29), is due to the ordering of hydrogen vacancies such that the sites labeled (ii) in Figure 34 have occupation probabilities of 1 and the sites labeled (i) have occupation probabilities of  $\frac{1}{2}$ . This was confirmed by structure factor calculations where vacancies were placed as shown in Figure 34. The  $\epsilon \rightarrow \zeta$  transition at  $-66^{\circ}\text{C}$  appears to have the characteristics of a first order transition, in agreement with DTA<sup>(64)</sup> specific heat<sup>(33)</sup>, and elastic constant<sup>(34)</sup> measurements.

However, the observations in this work are not entirely in agreement with Schober's results which indicated distinct  $\{1\bar{2}0\}_c$   $\zeta$  reflections and no intensity at the  $\{1\bar{2}0\}_c$  in the  $\zeta$  phase. The range of stability of the phase was reported to be  $-65^{\circ}\text{C}$  to  $-45^{\circ}\text{C}$ . Above  $-45^{\circ}\text{C}$  the  $(\bar{1}20)_c$  intensity was reported to disappear and the structure to become the  $\beta$  hydride.

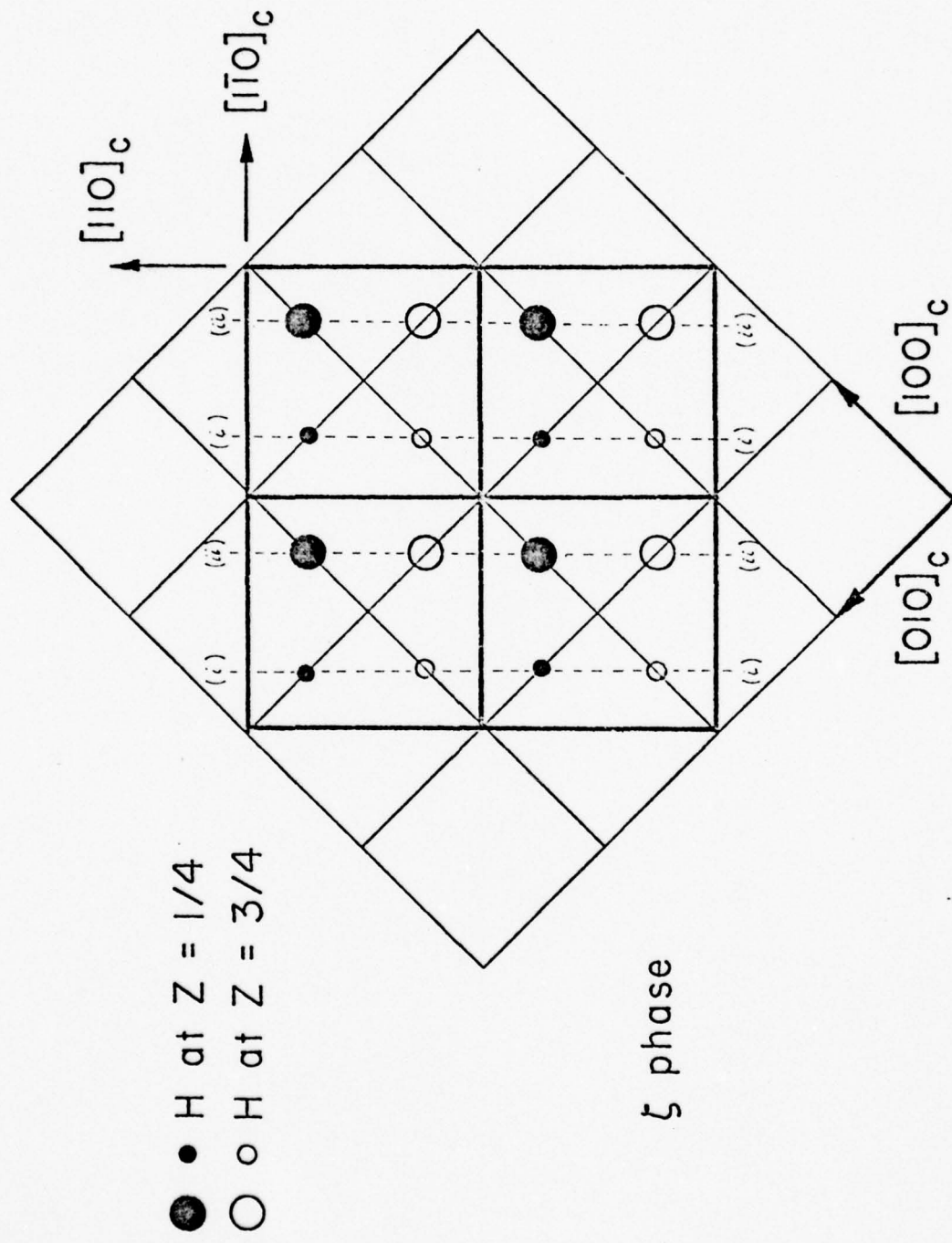


Figure 34. The proposed structure of  $\xi$  hydride. Large circles indicate positions of occupation probability = 1 and small circles indicate positions where the H occupation probability is 0.5. Four unit cells are shown.

In the present experiments, in all cases where the  $\zeta$  hydride was observed, the  $(\frac{1}{2}\bar{2}0)_c$  reflections were accompanied by reciprocal lattice streaks in the  $[100]_c$  and  $[010]_c$  directions (Figures 35-37) with weak intensity maxima at  $(\frac{1}{2}00)_c$  and  $(0\frac{1}{2}0)_c$ . The  $\zeta(\frac{1}{2}\bar{2}0)_c$  reflections and their associated streaks did not disappear at  $-45^\circ\text{C}$ ; rather their intensities gradually decreased as the temperature increased. Both the  $(\frac{1}{2}\bar{2}0)_c$  reflections and the streaks were detectable up to approximately  $0^\circ\text{C}$ .

The gradual decrease in  $\zeta$  reflection intensity with increasing temperature and the occurrence of  $<100>$  streaks will be treated here as two separate but related phenomena. First, the  $\zeta \rightarrow \beta$  disordering of H vacancies does not appear to occur as a distinct first order transformation. The continuous decrease in the  $\zeta(\frac{1}{2}\bar{2}0)_c$  diffracted intensity on increasing the temperature above  $-66^\circ\text{C}$  corresponds to decreasing order of the H vacancies in the  $[1\bar{1}0]_c$  direction, i.e., the occupation probability of type (ii) sites decreases and that for type (i) sites increases towards the  $\beta$  hydride occupation probability of 0.75. The intensity at the  $\zeta$  reciprocal lattice points is a function of the difference in electron scattering between  $(1\bar{1}0)_c$  planes, which varies as the difference in vacancy population on alternate planes. The conclusion that the  $\zeta \rightarrow \beta$  transition is second order, is supported by the fact that three previous studies using DTA<sup>(64)</sup>, specific heat<sup>(33)</sup>, and the variation of elastic constants with temperature<sup>(34)</sup> have failed to show any first order transformation behavior.

The observation of streaks in the  $[100]_c$  and  $[010]_c$  reciprocal directions through  $(\frac{1}{2}\bar{2}0)_c$ , and the observation of weak maxima at  $(\frac{1}{2}00)_c$  and  $(0\frac{1}{2}0)_c$  in the  $\zeta$  temperature range can be interpreted in a number of ways.

Figure 35. An  $(001)_c$  diffraction pattern taken at  $-61^\circ\text{C}$ . Sample composition is  $\text{H}/\text{Nb}=0.66$ . The  $(\frac{1}{2}\frac{1}{2}0)_c$  superlattice reflection is shown as well as streaking in the  $[010]_c$  and  $[100]_c$  directions.

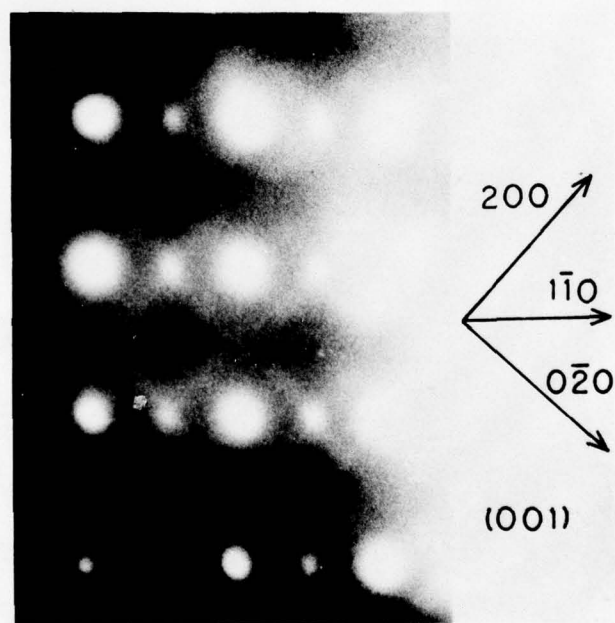
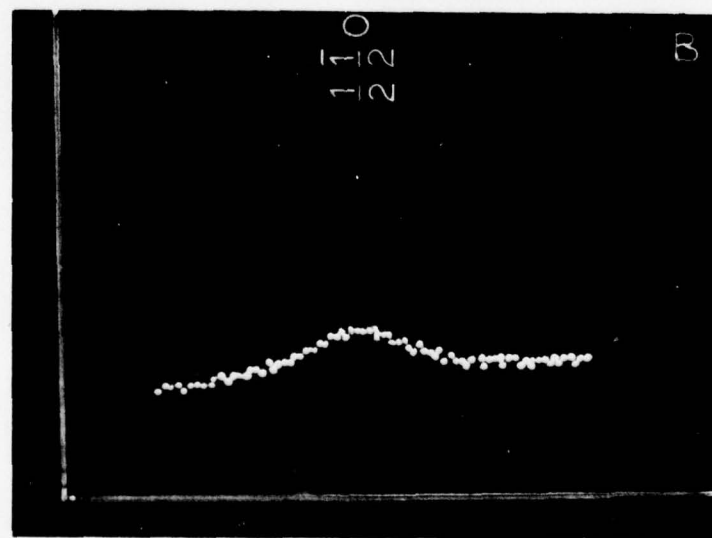
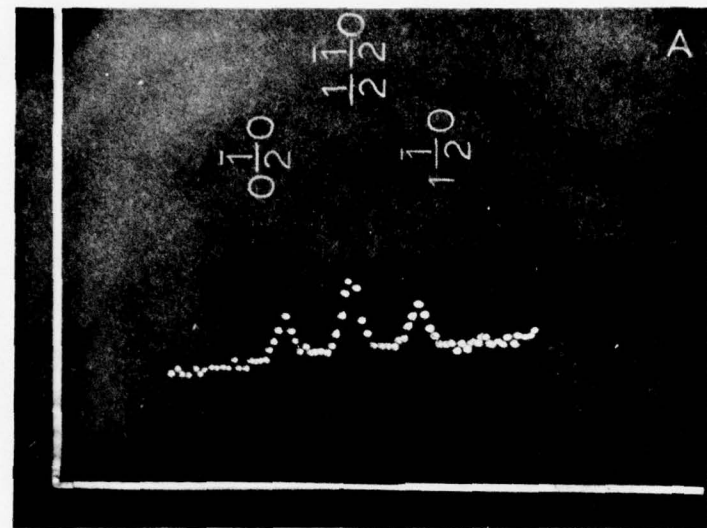


Figure 36A. Scanning-Diffraction taken through three superlattice reflections of the  $\epsilon$  phase at  $-180^{\circ}\text{C}$ .

Figure 36B. Scanning diffraction taken at  $-40^{\circ}\text{C}$ . The three reflections of the  $\epsilon$  phase have changed to the single diffuse (streaked) peak of the  $\zeta$  phase. The weak maximum at  $(0\frac{1}{2}0)_c$  could not be detected using this technique.



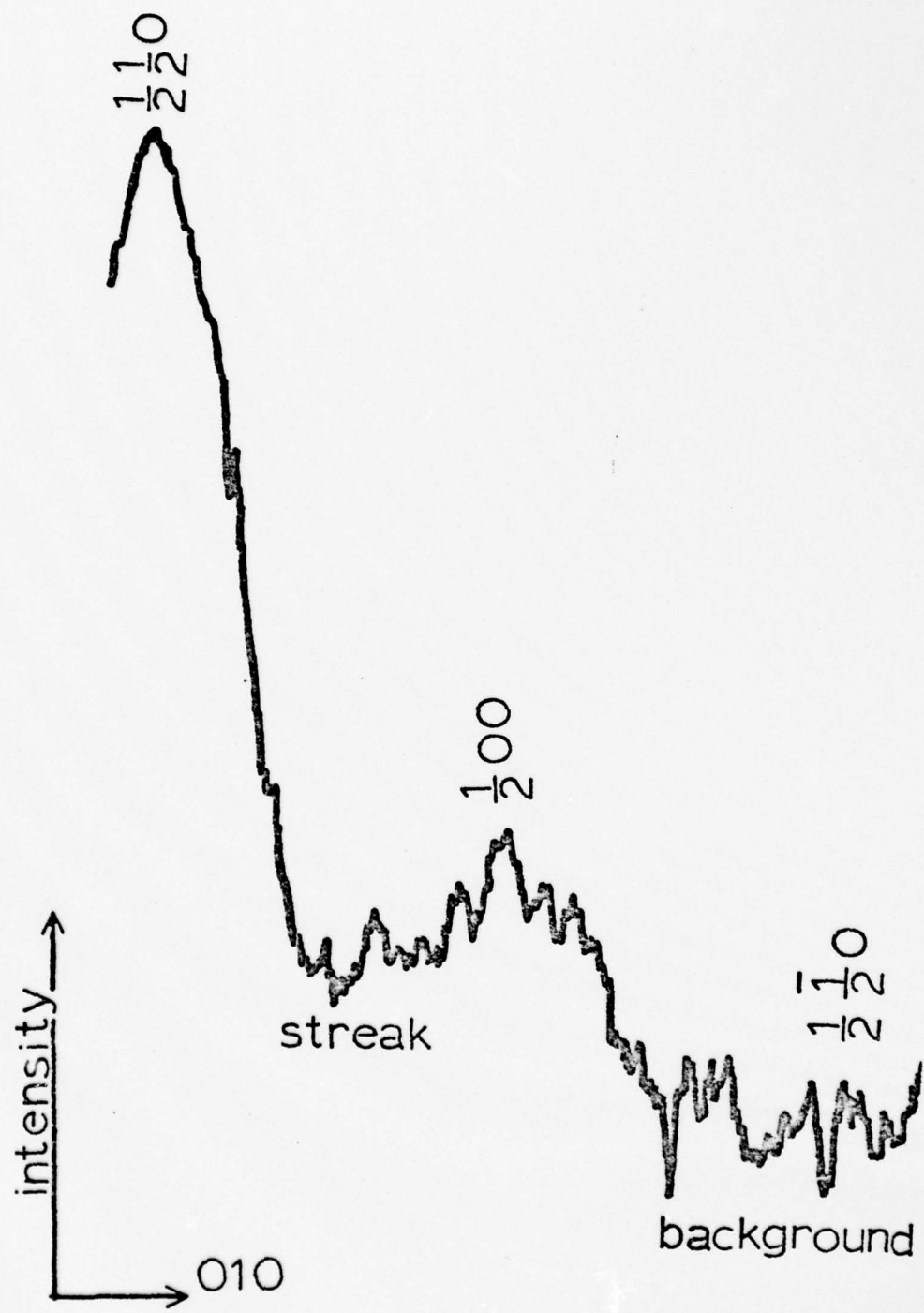
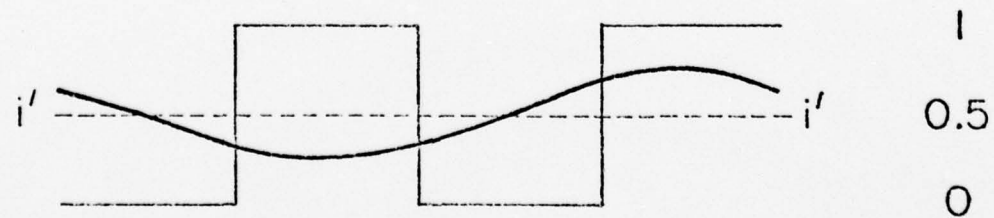
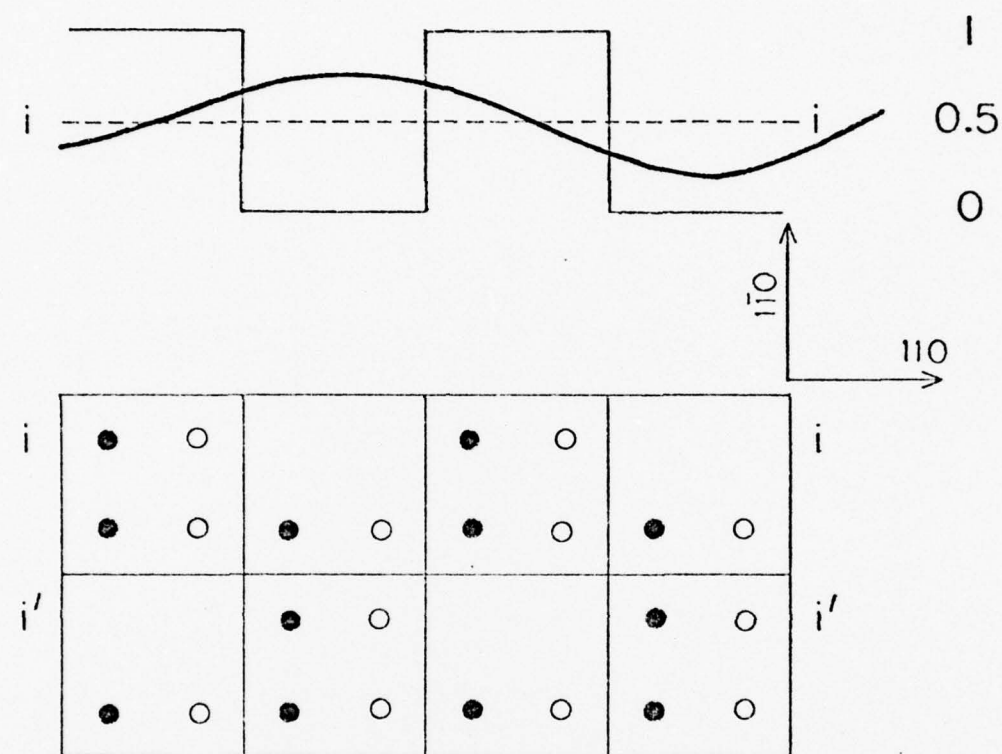


Figure 37. Photo-densitometer tracing taken from Figure 35 of the  $\zeta$ -phase. The  $\zeta$  superlattice reflection, streaking, and the weak maximum at  $(\frac{1}{2}00)_c$  are shown.

The model most consistent with the data is based on a fluctuation phenomenon in which the H vacancies order on the type (i) sites in a number of continuous ordered distributions, of varying wavelength, between the 0-1 bimodal distribution characteristic of the  $\epsilon$  phase and the occupation probability of 0.5 of the  $\zeta$  phase (Figure 38). Such distributions could be a continuous phenomenon throughout the sample or could also possibly take the form of discrete short lived heterophase particles<sup>(66)</sup>. In either case these fluctuations give rise to intensity between the  $(\frac{1}{2}\bar{2}0)_c$  and the  $(\frac{1}{2}00)_c$  and  $(0\frac{1}{2}0)_c$  positions in reciprocal space. The intensity maximum at the  $\{\frac{1}{2}00\}_c$  reflections indicates that the most probable fluctuation is that corresponding to the  $\epsilon$  phase. The abrupt termination of the streaks at the  $(\frac{1}{2}00)_c$  and  $(0\frac{1}{2}0)_c$  spots, then is a consequence of these fluctuations. As the temperature is increased towards 0°C, the intensity in the streaks gradually decreases and above this temperature only the  $\beta$  phase structure is observed.

In summary, the transformation on heating from the  $\epsilon$  phase to the  $\beta$  phase occurs in a series of steps. Below -66°C the H vacancies are distributed on only type (i) sites, and furthermore, exhibit a bimodal 0-1 probability distribution. At  $T_c$  ( $\epsilon \rightarrow \zeta$ ), -66°C, the confinement of vacancies to type (i) sites persists, while the bimodal distribution weakens and many occupancy fluctuations occur among the various type (i) sites. As temperature continues to increase, the confinement of vacancies to the type (i) sites gradually breaks down until only the  $\beta$  type sublattice, with uniform occupation probability of 0.75 exists at room temperature.

Figure 38. The variation of hydrogen occupation probability on type (i) sites with increasing temperature. Two  $\epsilon$  unit cells are shown with hydrogen vacancies allowed along lines  $i - i$  and  $i' - i'$ . The  $\epsilon$  phase has a bimodal 0-1 (square wave) distribution. The transformation of  $\epsilon \rightarrow \zeta$  has been described as a transformation from the 0-1 bimodal distribution to the uniform occupation probability of 0.5 on all type (i) sites. The streaked diffraction pattern shown in Figure 35 can be explained by allowing periodic fluctuations in hydrogen density on the type (i) sites. The distributions are drawn out of phase to eliminate intensity near  $(\frac{1}{2}, 0)$ .



The fact that  $\langle 100 \rangle_c$  streaking seen in this work has not been reported by previous TEM investigators may be in part due to the use of different accelerating voltages. Because of the flatter Ewald sphere, for low wavelength electrons, higher index reflections can, in principal, be observed at 200 KV than at 100 KV and therefore, observations can be made far from the diffuse inelastic background that pervades the center of the electron diffraction pattern. The use of 200 KV accelerating potential also lessens the magnitude of the diffuse background. Thus, higher voltages increase the chance of detecting streaks which are very weak and which may be very narrowly confined to a particular reciprocal plane.

Observations made in the course of this investigation indicate that the weak  $(\frac{1}{2}\bar{1}0)_c$  reflection is detectable at higher temperatures using 200 KV vs. 100 KV. The streaks, although definitely present in diffraction patterns taken at 100 KV operation, are very hard to distinguish from the diffuse background.

#### 4.2.2 The $\lambda$ Phase

As noted in Section 1, the Xray data of Pick (31) indicates that a low temperature bcc  $\gamma$  hydride exists in the composition range from approximately  $H/Nb=0.85$  to  $0.98$ . Welter et al. (65) have interpreted their DTA data as indicating a sequence of at least three  $\lambda$  phases at low temperatures, one of which may be identical to the  $\gamma$  phase (Figure 1). At present the structural relationships between these various ordered non-stoichiometric hydride phases is not understood. An attempt was made in this investigation to study the morphology and possible ordered structures of high concentration hydrides at  $-180^{\circ}\text{C}$ .

Palladium coated niobium samples were electrolytically charged at  $120$ - $140^{\circ}\text{C}$  to compositions in the range  $H/Nb=0.72$  to  $H/Nb=0.98$ . On cooling to room temperature all samples were multi-domain  $\beta$  phase (Figure 39). The specimens were then cooled in situ from room temperature to  $-180^{\circ}\text{C}$ . Morphological electron diffraction studies were carried out at  $-180^{\circ}\text{C}$  and on warming to room temperature.

The observations can be summarized as follows.

1. Samples of composition  $H/Nb=0.72$ , observed at  $-180^{\circ}\text{C}$ , showed a small amount of second phase,  $\lambda$ , in an  $\epsilon$  matrix (Figure 40). The  $\lambda$  precipitates took the form of plates parallel to  $(001)_c$  which appeared to have nucleated at  $\epsilon$  domain boundaries. Diffraction patterns (Figure 41) showed large numbers of superlattice reflections along the  $[001]_c$  which is perpendicular to the  $[010]_c$  and  $[100]_c$  directions which show  $(\frac{1}{2}00)_c$  and  $(0\frac{1}{2}0)_c$   $\epsilon$  superlattice reflections from the  $\epsilon$  phase matrix. Dark field studies (Figures 42, 43) indicate that the  $\epsilon$  reflections are not incorporated in the reciprocal lattice of the  $\lambda$  phase.

2. On warming, the  $\epsilon$  matrix transformed to  $\zeta$  hydride at  $-66^{\circ}\text{C}$ . At  $-40^{\circ}\text{C}$   $(001)_c$  plates of  $\zeta$  hydride appeared within the  $\lambda$  precipitates, and grew to consume the  $\lambda$ .

3. The thinned areas of samples with average composition 0.85 to 0.90 transformed entirely to a single phase  $\lambda$  during cooling to  $-180^{\circ}\text{C}$ . The  $\beta$  domain boundaries disappeared and were replaced with fringed boundaries which were non-planar and were not crystallographic in nature (Figures 44). The sample morphology also showed fine striations perpendicular to  $[001]_c$  on  $(100)_c$  foils. These striations, with approximately  $60-250 \text{ \AA}$  spacings, changed directions in the  $\lambda$  phase upon crossing a fringed boundary (Figures 44, 47). Associated diffraction patterns (Figures 45, 46) also showed large numbers of superlattice reflections along  $[001]_c$  but with different spacing than the lower concentration  $\lambda+\epsilon$  sample (Figure 50). On gradual heating, the samples returned entirely to the  $\beta$  hydride. The new domain pattern of the room temperature  $\beta$  phase was generally not the same as that observed prior to cooling. This was due to a high mobility of  $\beta$  domain boundaries which was observed just above the  $T_c(\lambda-\beta)$  and which was probably caused by stresses induced by the transformation.

4. Samples of composition  $\text{H}/\text{Nb}=0.91-0.96$  at  $-180^{\circ}\text{C}$  showed morphologies and diffraction patterns similar to those observed for the  $\lambda$  phases at lower  $\text{H}/\text{Nb}$  ratios. The superlattice reflection spacing along  $[001]_c$  (Figures 47, 48) again depended on composition. The presence of  $\{\frac{1}{2}\frac{1}{2}1\}_c$  reflections was noted in some of the patterns obtained in this composition range, and this may indicate the presence of some  $\beta$  phase, in addition to the  $\lambda$ .

5. In samples of composition  $H/Nb=0.97$ , rapid cooling to  $-180^{\circ}\text{C}$  resulted in a  $\beta$  phase structure as indicated by the morphology and diffraction patterns. On holding for several minutes at  $-180^{\circ}\text{C}$ , plates of  $\lambda$  hydride nucleated at  $\beta$  domain boundaries (Figure 49) and a two phase mixture of  $\lambda$  and  $\beta$  was formed. Samples of composition  $H/Nb=0.98$  remained entirely single phase  $\beta$  hydride on cooling to  $-180^{\circ}\text{C}$ . No evidence was found for a structure as simple as that suggested by Pick<sup>(31)</sup>, (i.e. having dimensions 2 times the  $\beta$  cell in all dimensions).

In every case where the  $\lambda$  phase was observed, superlattice reflections along the  $[001]_c$  direction were always present. These could be interpreted as satellites of the bcc fundamental reflections and as satellites of the extinct  $(\frac{1}{2}\frac{1}{2}1)_c$  reflections. Most of the observed  $\lambda$  diffraction patterns are complicated by double diffraction, streaking, and by anomalous diffraction spots due to the intersection of streaks with various reciprocal lattice planes. Furthermore, the spacing of superlattice reflections changed with hydrogen concentration as shown in Figures 50-53. The superlattice reflections along the  $[001]_c$  direction appeared at approximately the positions summarized in Table 4.

Transformation temperatures, for the  $\lambda \rightarrow \beta$  transition, as observed on heating, are given in Figure 54.

Brun et al.<sup>(42)</sup> have recently confirmed the existence of  $\lambda$  superlattice reflections at low temperatures for a large deuteride crystal of composition  $D/Nb=0.84$  using neutron diffraction. The superlattice reflections were observed at approximately  $(0,0,3/7)_c$ ,  $(1/2, 1/2, 11/14)_c$  and  $(1/2, 1/2, 17/14)_c$ .

Figure 39.  $\beta$  hydride at room temperature and composition  $H/Nb = 0.94$ .  
Hydrogen charging was performed electrolytically at  $130^\circ C$ .

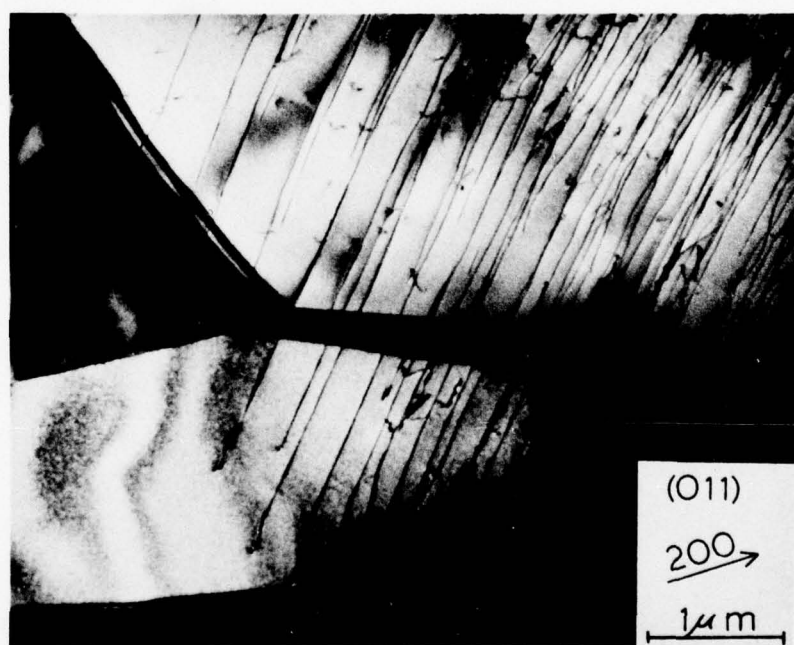


Figure 40.  $\lambda$  hydride plates in an  $\epsilon$  hydride matrix. Sample composition is  $\text{NbH}_{0.72}$ . An  $\epsilon$  domain boundary can be seen in the upper left of the micrograph.

Figure 41.  $(\bar{1}\bar{1}0)_c$  diffraction pattern taken from an area containing both  $\epsilon$  and  $\lambda$  hydride. composition is  $\text{NbH}_{0.72}$ .

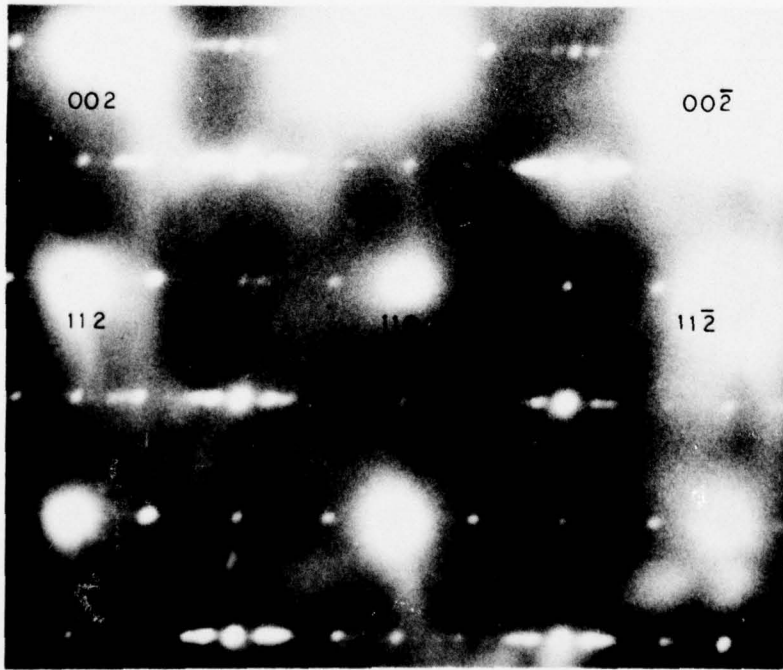
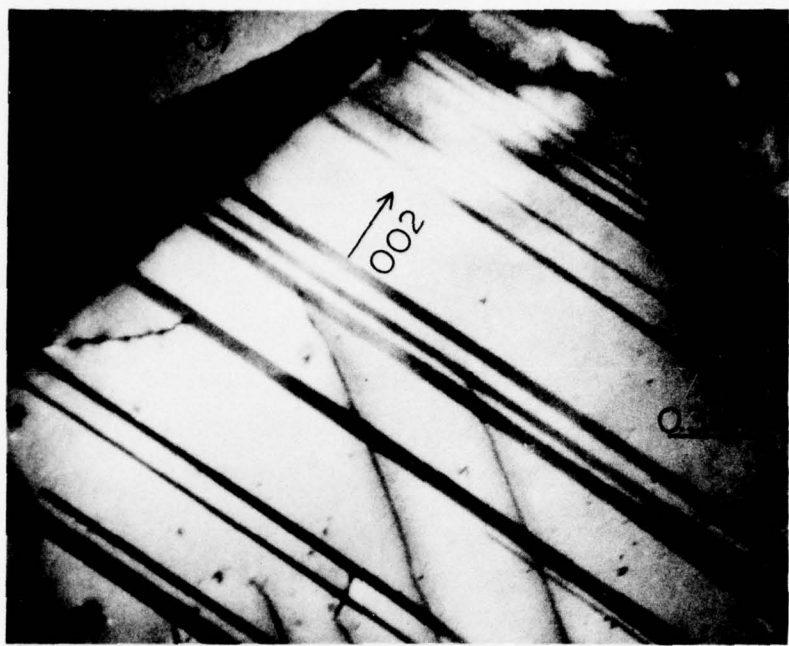


Figure 42. Dark field micrograph taken using the  $\lambda$  reflection indicated.  
Sample composition is  $\text{NbH}_{0.72}$ .

Figure 43. Dark field micrograph using the  $\epsilon$  reflection indicated. Sample composition is  $\text{NbH}_{0.72}$ . This micrograph corresponds to the upper righthand corner of Figure 40. Since the  $\lambda$  plates are not "bright" in this micrograph, the conclusion can be drawn that the  $\epsilon$  reflection is not incorporated in the  $\lambda$  reciprocal lattice.

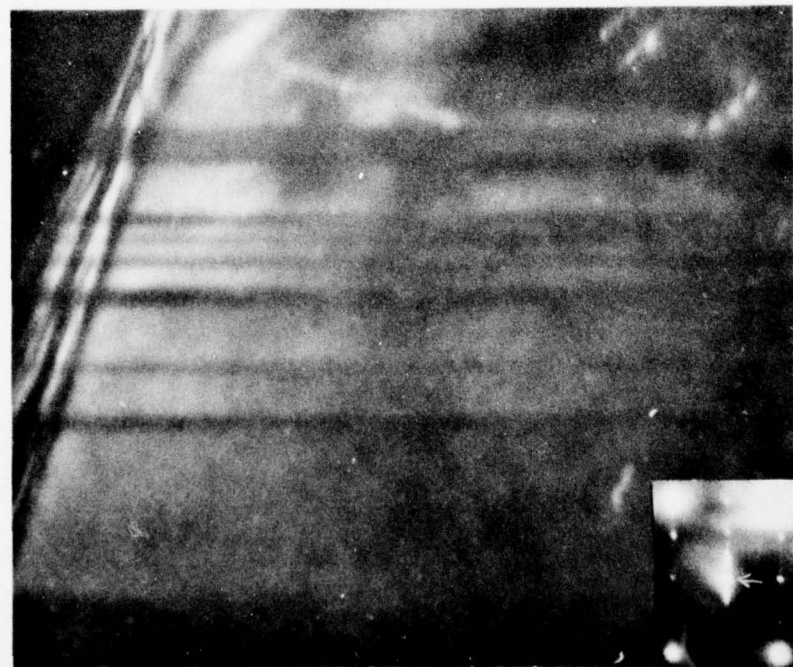
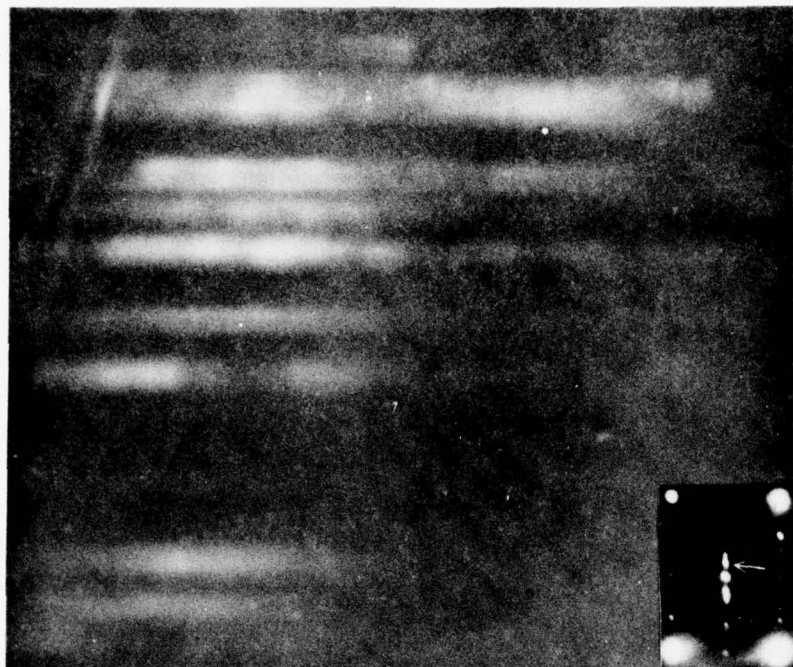


Figure 44. Two transmission micrographs showing the non-crystallographic domain boundaries of the  $\lambda$  phase. These boundaries often formed in nearly the same location as the crystallographic domain boundaries of the parent  $\beta$  phase. Sample composition is  $\text{NbH}_{0.85}$ .

AD-A060 004

ILLINOIS UNIV AT URBANA-CHAMPAIGN DEPT OF METALLURGY --ETC F/G 11/6  
PRECIPITATION AND ORDERING IN THE NIOBium-HYDROGEN SYSTEM. (U)

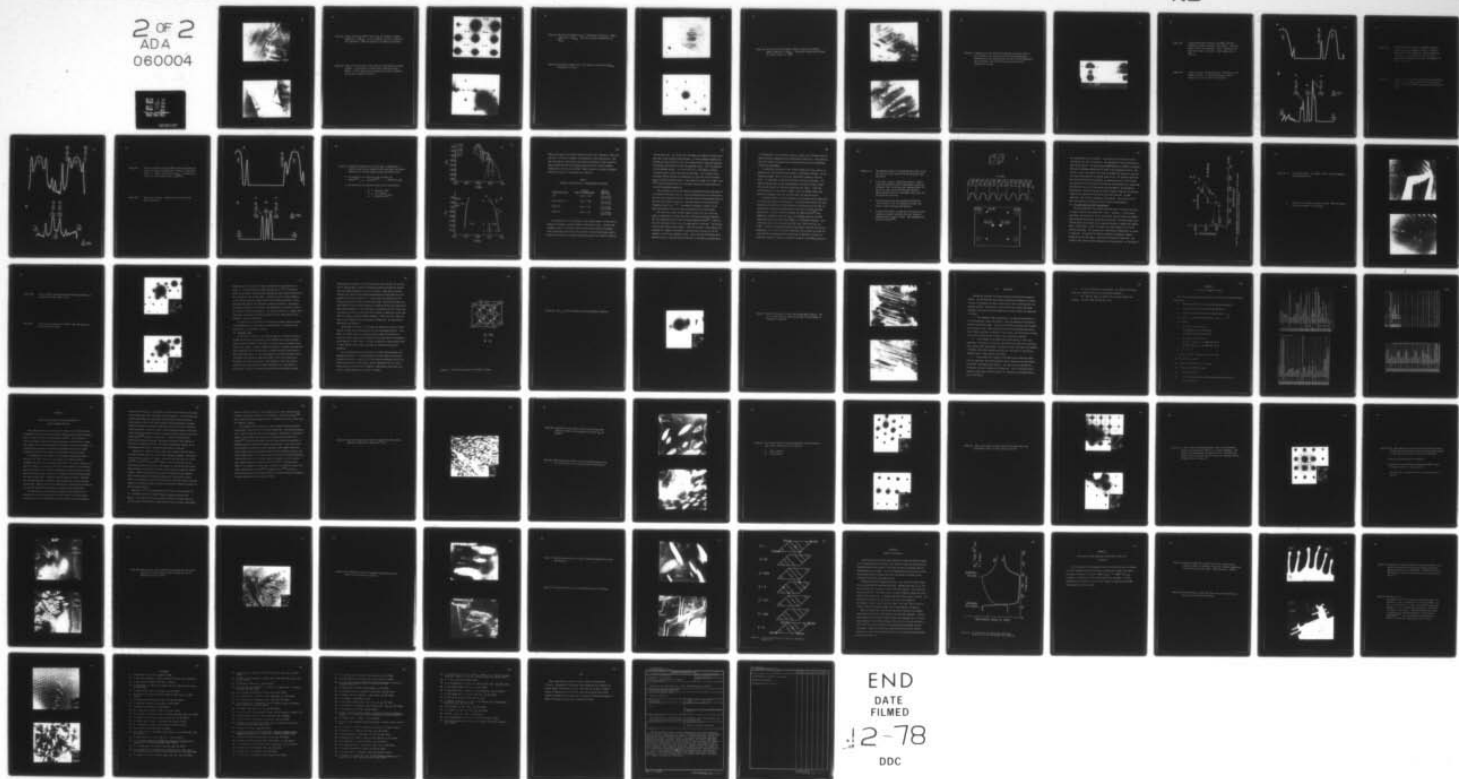
JUL 78 B J MAKENAS

N00014-75-C-1012

NL

UNCLASSIFIED

2 OF 2  
ADA  
060004



END

DATE

FILMED

JUL-78

DDC

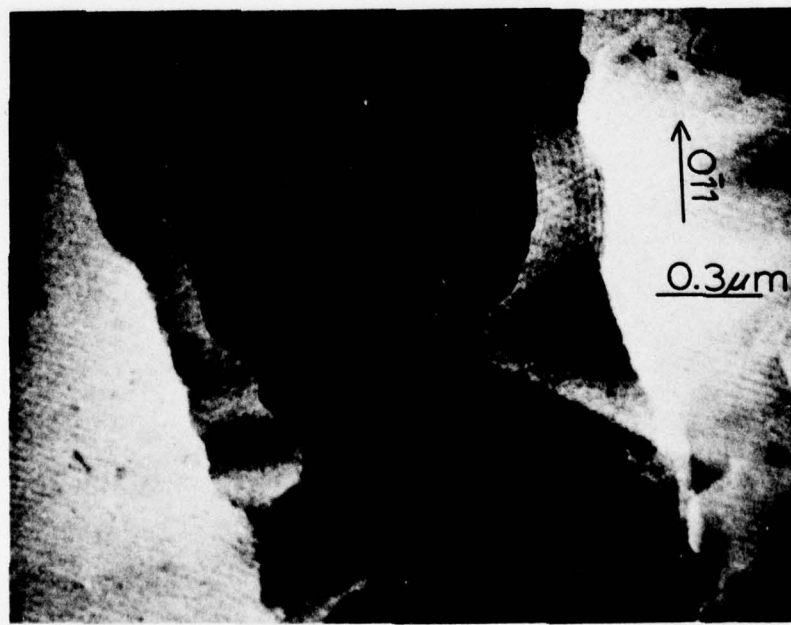


Figure 45.  $(1\bar{1}0)_c$  diffraction pattern from an area of  $\lambda$  hydride. Sample composition is  $\text{NbH}_{0.85}$ . No  $\beta$  or  $\epsilon$  hydride was seen in samples of this composition. Note the absence of the  $(\frac{1}{2}\frac{1}{2}1)$   $\beta$  reflections.

Figure 46.  $(100)_c$  diffraction pattern taken from the same specimen as Figure 45 above. The presence of  $\lambda$  superlattice reflections along  $[002]_c$  in both of these figures indicates that these reflections are not due to double diffraction.

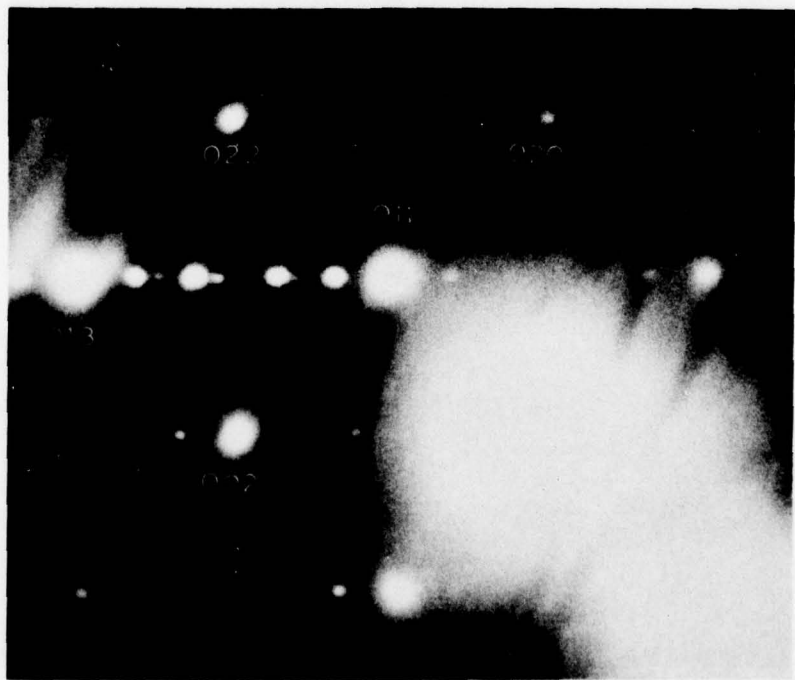
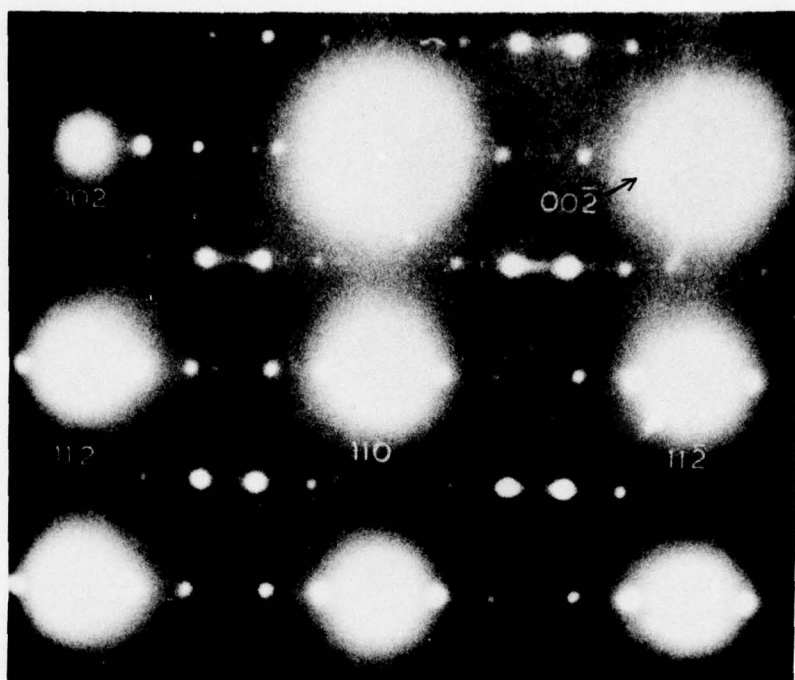


Figure 47. Dark field micrograph using a  $\lambda$  superlattice reflection. Sample composition is  $\text{NbH}_{0.96}$ . Note the striations perpendicular to  $[002]_c$ .

Figure 48. Diffraction pattern taken from a sample of composition  $\text{NbH}_{0.96}$ . Orientation is  $(1\bar{1}0)_c$ .

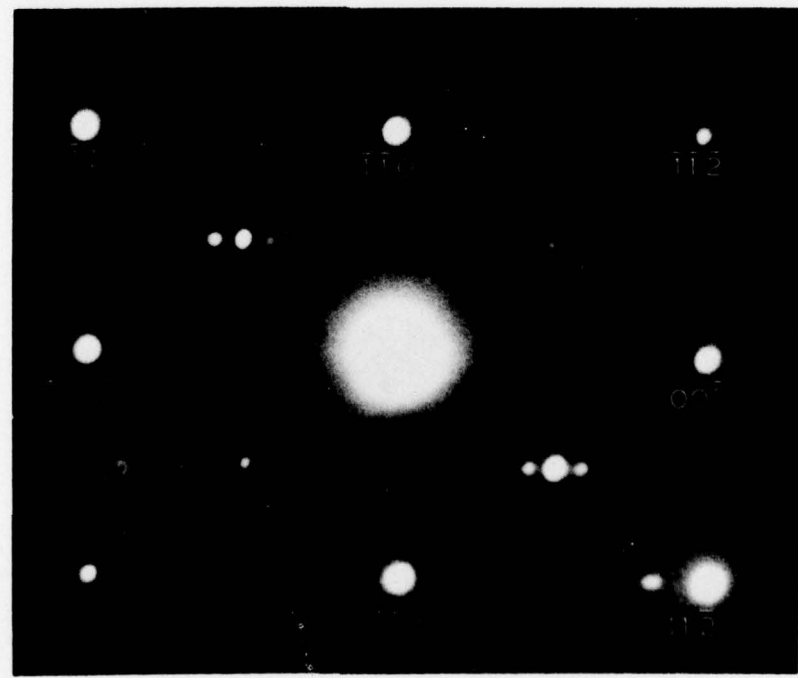
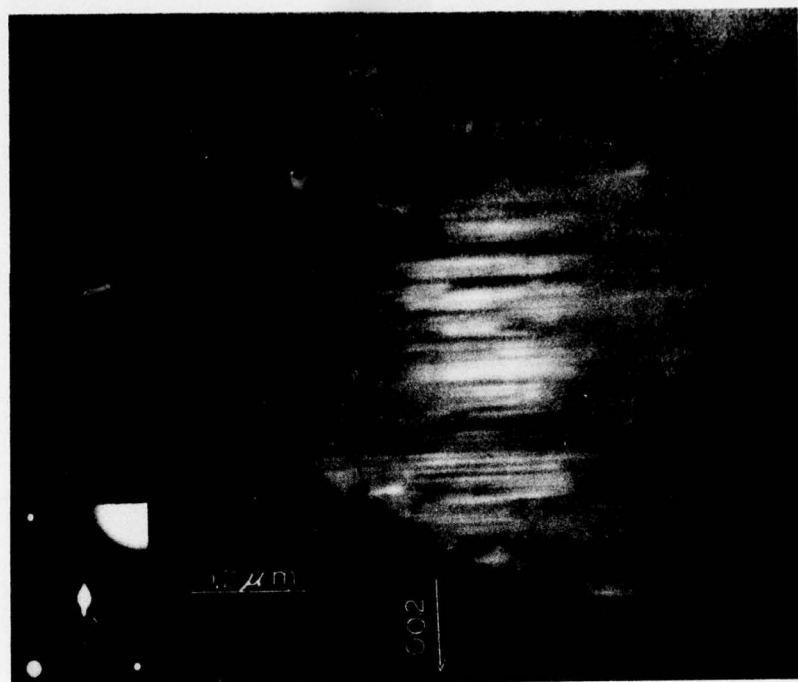


Figure 49. Two transmission micrographs showing  $\lambda$  plates in a  $\beta$  matrix.  
Sample composition is  $\text{NbH}_{0.97}$ . These plates formed after holding  
for several minutes at  $-180^\circ\text{C}$ .

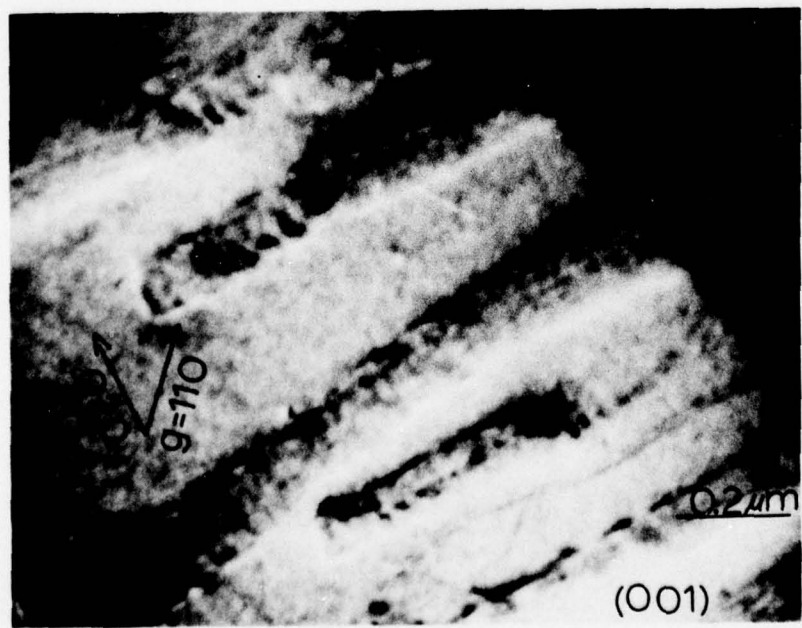
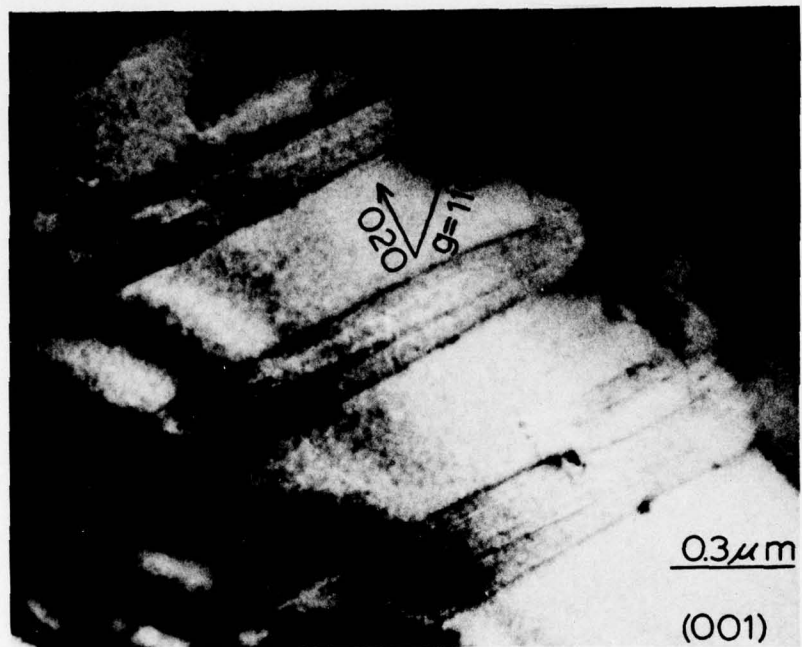


Figure 50. A composite of three diffraction patterns showing the shift in first  $\lambda$  superlattice reflection with increasing composition. Measurements of peak spacings here were made from the photographs and are probably less accurate than those made from the densitometer tracings.

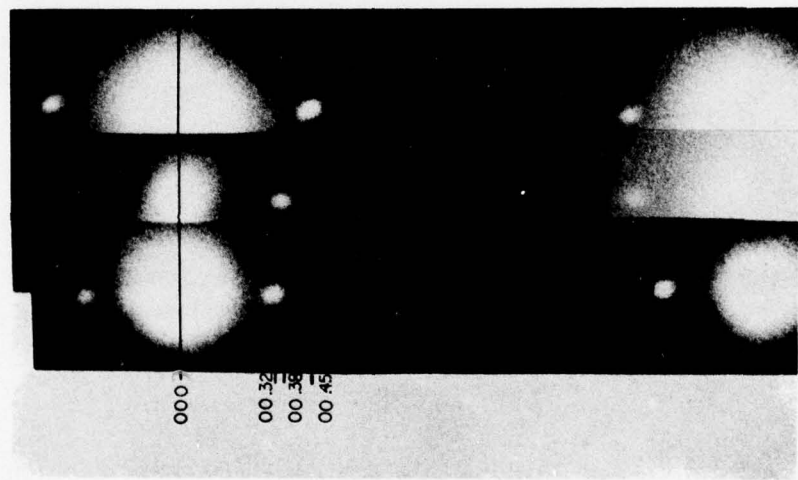
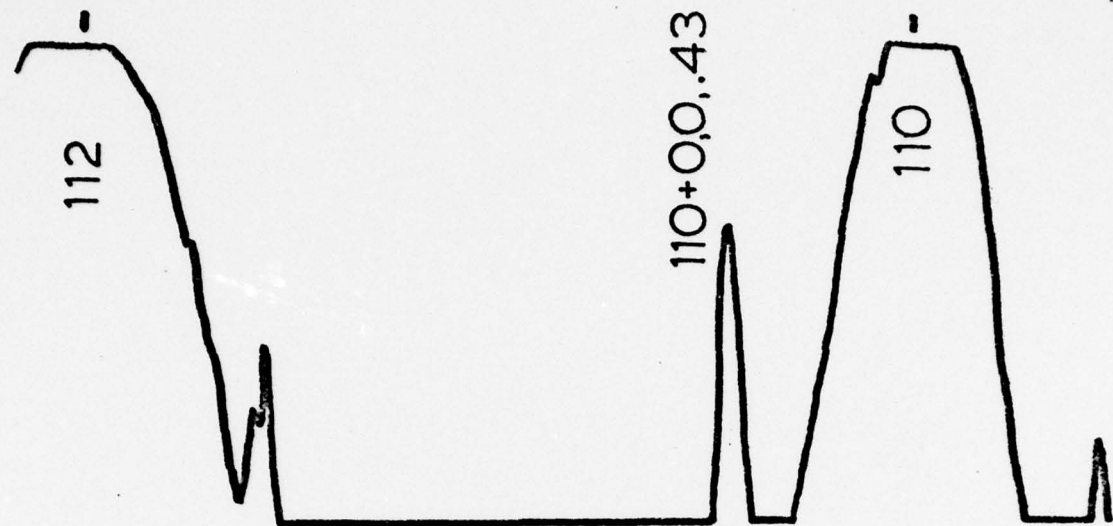


Figure 51A. A photo-densitometer tracing in the  $[002]_c$  direction through two niobium reciprocal lattice peaks. Truncated peaks indicate film saturation. Weak  $\lambda$  reflections are observed at  $(hk1) \pm (0,0,.43)$ . Sample composition is  $\text{NbH}_{0.72}$ .

Figure 51B. A similar tracing through the  $(\frac{1}{2}21)_c$   $\epsilon$  reflection in the  $[002]_c$  direction. The diffraction pattern shown in Figure 41 was used for both of these plots.

A



99

B

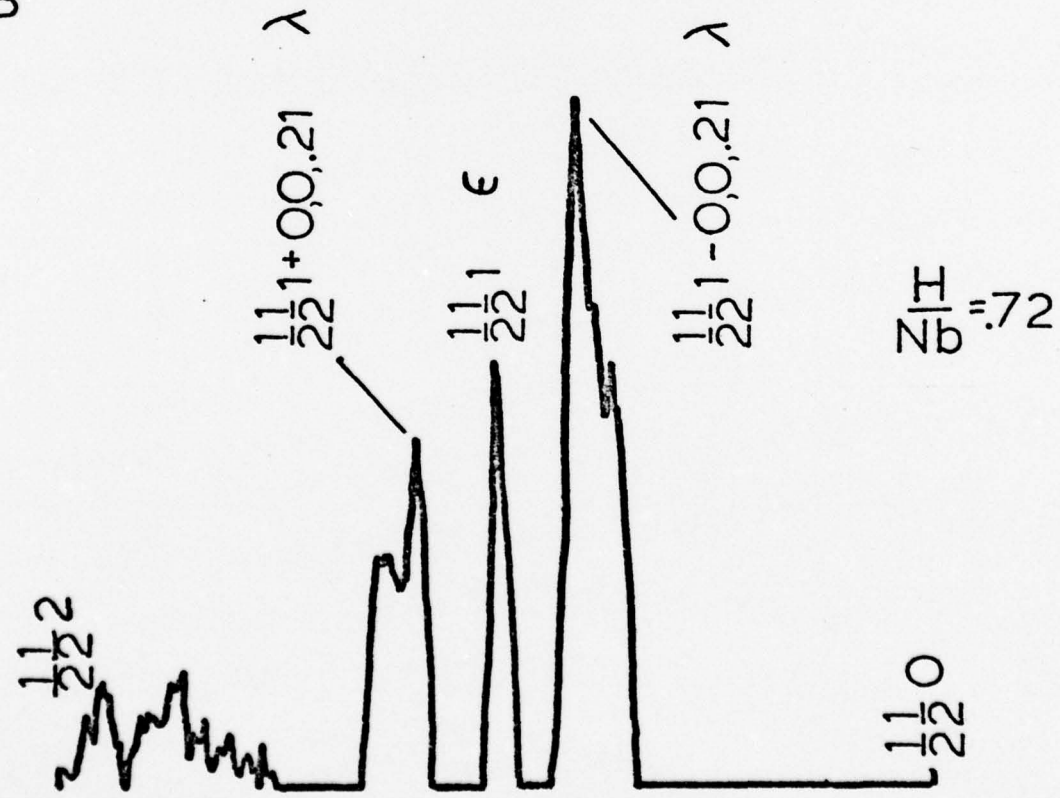
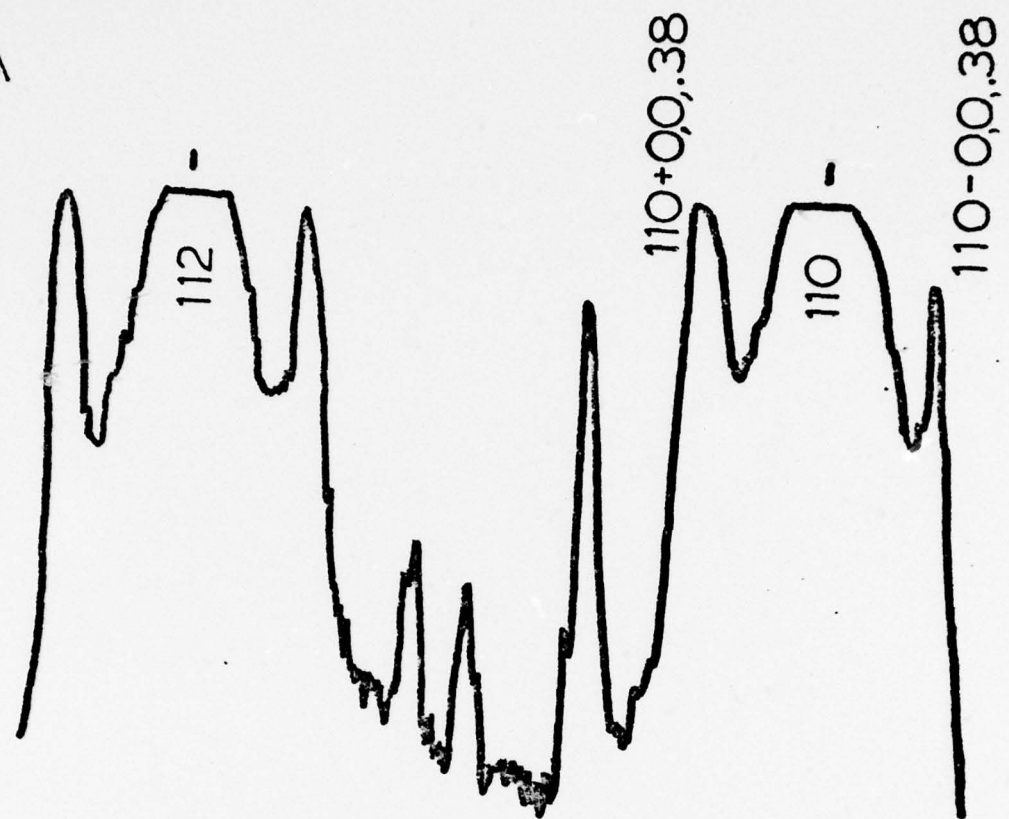


Figure 52A. Photo-densitometer tracing in the  $[002]_c$  direction through two niobium reciprocal points. Truncated peaks indicate film saturation. Sample composition is  $\text{NbH}_{0.85}$ . Figure 44 was used for this plot.  $\lambda$  superlattice reflections can be seen along  $[002]_c$  at  $(hk1) \pm (0,0,.38)$ .

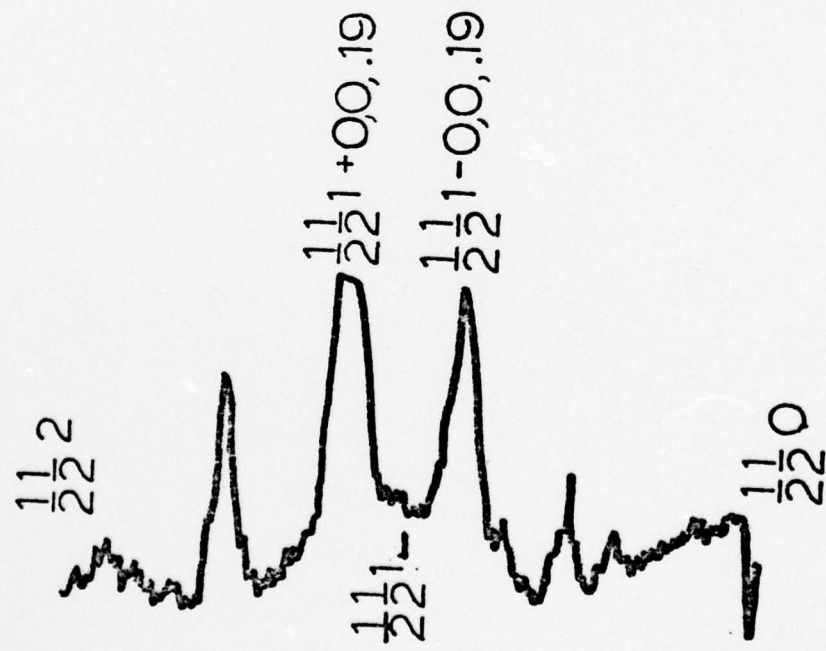
Figure 52B. A similar tracing in the vicinity of the extinct  $(\frac{1}{2}\frac{1}{2}1)_c$  reflection. The  $(\frac{1}{2}\frac{1}{2}1)_c \beta$  reflection does not appear to be incorporated into the reciprocal lattice of the  $\lambda$  phase.

A



101

B



$$\frac{Z}{\sigma} = 85$$

Figure 53A. Photo-densitometer tracing in  $[002]_c$  direction through two niobium reciprocal lattice points. Tracing is taken from Figure 48. Sample composition is  $\text{NbH}_{0.96}$ .  $\lambda$  Superlattice reflections can be seen at  $(hkl) \pm (0,0,.31)$ .

Figure 53B. Same sample as above. Tracing in the vicinity of the  $(\frac{1}{2}\frac{1}{2}1)_c$  reflection.

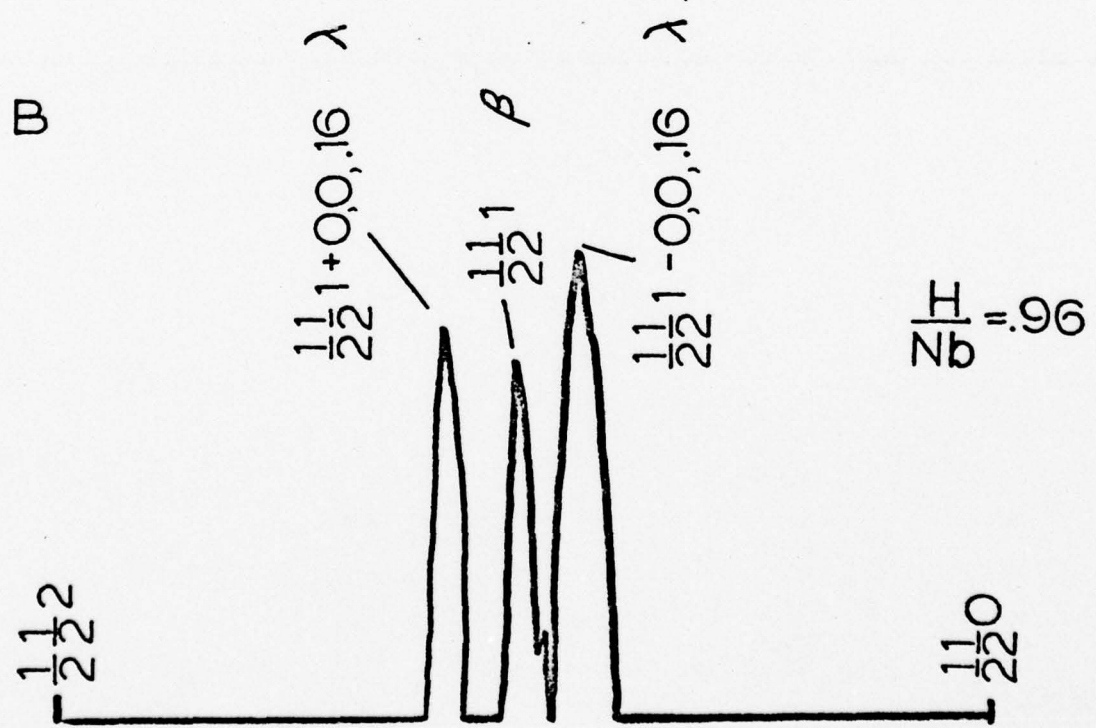
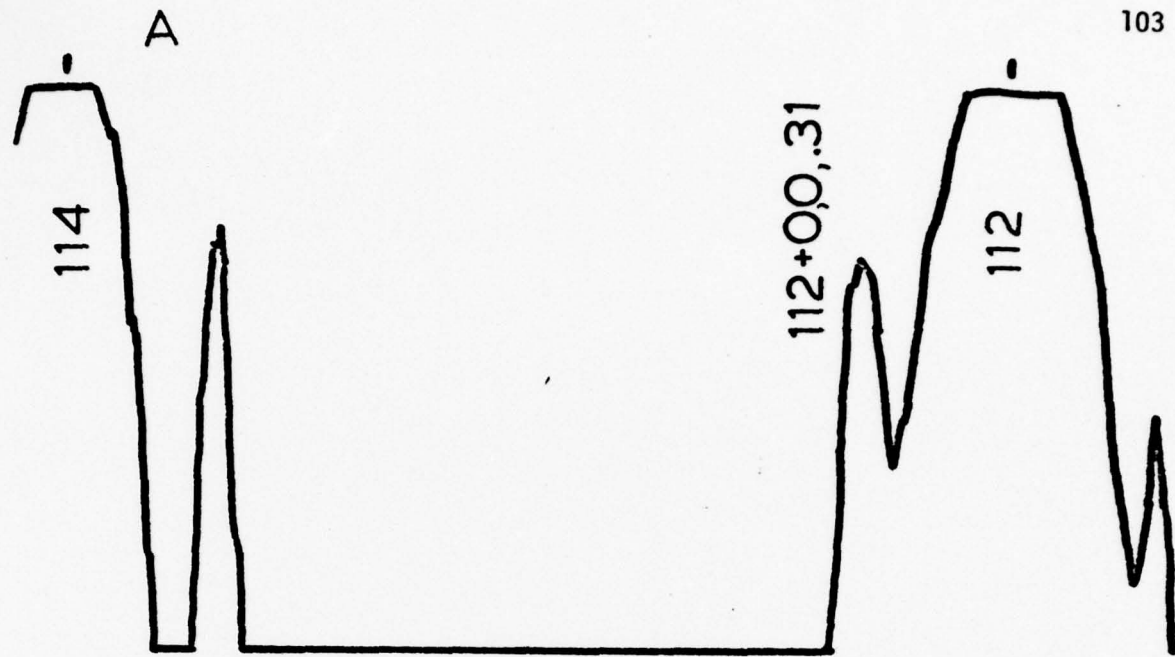
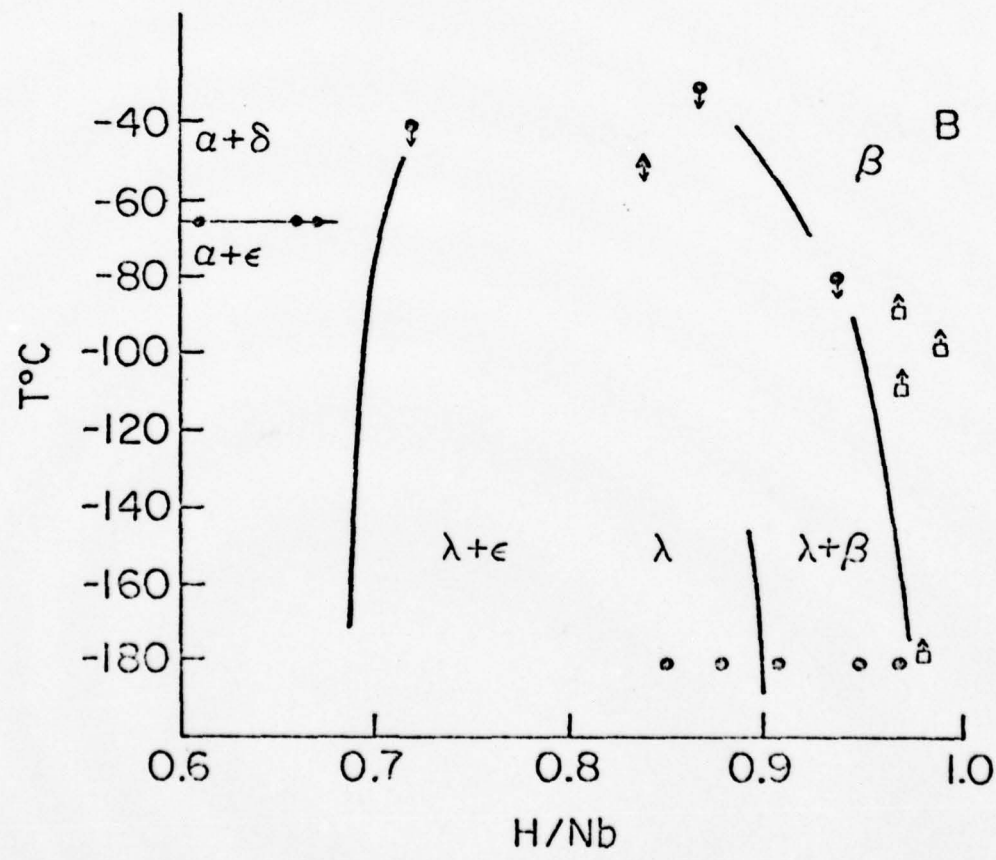
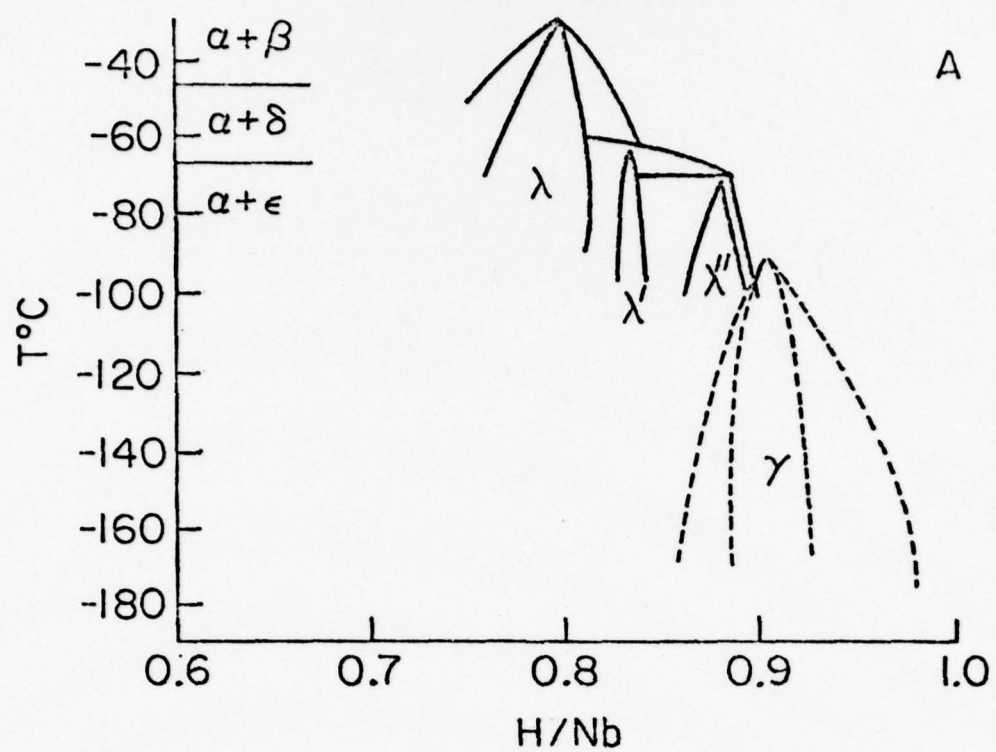


Figure 54. Although TEM methods are not sufficient, in themselves, to determine phase diagram boundaries with confidence, qualitative comparisons can be made between previous and present work.

A. The summarized low temperature data of Welter and Schober<sup>(77)</sup> \_\_\_\_\_ and Pick<sup>(31)</sup> . . . . (DTA and X-rays)

B. The summarized low temperature data of this investigation.

- $\lambda$  - observed in TEM
- $\beta$  - no  $\lambda$  observed
- ▲  $\lambda$  - deuterium, Brun<sup>(42)</sup>



These investigators found that  $\lambda$  hydride coexists with  $\epsilon$  hydride at  $-196^{\circ}\text{C}$  and that the  $\lambda$  reflections disappear at approximately  $-50^{\circ}\text{C}$  upon heating. They have also shown by comparison of the relative intensities of the 6 possible  $\{\frac{1}{2}\frac{1}{2}1\}_c$  reflections that the relative population of the various  $\beta$  domains changes after thermal cycling  $\beta \rightarrow \lambda \rightarrow \beta$ . These results are in general agreement with those observed in the present work (Table 4).

TABLE 4  
REPORTED POSITIONS OF THE  $\lambda$  SUPERLATTICE REFLECTIONS

<u>Composition (H/Nb)</u>	<u>Indices (Near bcc Fundamental)</u>	<u>Indices (Near <math>\frac{1}{2}\frac{1}{2}1</math>)</u>
0.72	(0,0, $\pm .43$ )	(.5,.5,.79) (.5,.5,1.21)
0.84 (D/Nb, Brun)	(0,0, $\pm .428$ )	(.5,.5,.79) (.5,.5,1.21)
0.85-0.90	(0,0, $\pm .38$ )	(.5,.5,.81) (.5,.5,1.19)
0.91-0.96	(0,0, $\pm .31$ )	(.5,.5,.84) (.5,.5,1.16)

The transformation of the  $\beta$  phase to the  $\lambda$  phase appears to represent an ordering of hydrogen solutes on specific interstitial sites. Following the analogy of the  $\beta \rightarrow \epsilon$  transition, which is based on the ordering of hydrogen atoms and hydrogen vacancies on the  $\beta$  structure, the various  $\lambda$  phases may be based on the ordering of hydrogen atoms and vacancies on a specific subset of

interstitial sites. As the H/Nb ratio increases, the number of vacant hydrogen sites on any structure would decrease. If these hydrogen vacancies are ordered, the size of the unit cell will increase and the reciprocal superlattice vectors would shorten as the H/Nb approaches unity. This is consistent with the present results. The  $\lambda$  unit cell size in the  $[001]_c$  direction increased as the H vacancy concentration decreased. The variation of the reciprocal lattice spacing with composition is consistent with the  $\lambda$  phase being a series of distinct phases in the composition range  $0.72 < H/Nb < 0.97$  (65) or with the possibility of a continuous variation of  $\lambda$  phase unit cell size with increasing composition.

The structure of the hydride cannot be completely defined on the basis of the electron diffraction results. Positive determination of the exact hydrogen sites will necessitate precise diffracted intensity measurements which are best done with neutron scattering. Such measurements are being conducted presently by Brun et al. (42). Some general statements, however, can be made from electron diffraction data and structure factor calculations.

The  $\lambda$  unit cell cannot be based simply on the  $\beta$  unit cell since the  $\{1\frac{1}{2}1\}_c$   $\beta$  reflections are absent from the  $\lambda$  diffraction patterns (Figure 45). Nor can  $\lambda$  simply be based on the  $\gamma$  structure proposed by Hauk<sup>(35)</sup>, since his unit cell was shown to give rise to no superlattice reflections. Two explanations of the  $\lambda$  ordering seem tenable. The first involves a distribution of H vacancies on a simple stoichiometric structure such as the  $\beta$  unit cell of Somenkov or the  $\gamma$  cell suggested by Hauk. This H vacancy distribution would necessarily have a long wavelength periodicity in the  $[001]_c$  direction which

is incommensurate with the niobium lattice in order to be consistent with the repeat distances suggested by the  $\lambda$  superlattice reflections. Such distributions were shown by structure factor calculation to give rise to additional reflections along  $[001]_c$ .

An alternative structure is one in which single unit cells, such as  $\beta$  hydride cells, are stacked upon one another in the  $[001]_c$  direction. As the stacking proceeds, some unit cells are rotated with respect to the cell below. A large number of possible structures can then be generated. This type of stacking leads to the extinguishing of the normal  $\beta \{ \frac{1}{2} \frac{1}{2} 1 \}_c$  reflection and the creation of satellite reflections near  $\{ \frac{1}{2} \frac{1}{2} 1 \}_c$ . Large unit cells constructed in this way do, however, result in prohibitively close approach of hydrogen atoms near the point where the rotation occurs.

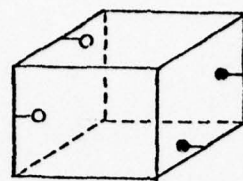
A tentative model for the  $\lambda$  structure can be proposed using a combination of the two explanations discussed above. A structure pertaining to the lower concentration ( $H/Nb=0.72$  to  $0.84$ )  $\lambda$  data will be discussed here but the conclusions should be generally applicable to the entire  $\lambda$  region with minor modification. For the  $\lambda$  structure observed for  $D/Nb=0.84$  Brun<sup>(42)</sup> has suggested a stacking of 14  $\beta$  unit cells in the  $[001]_c$  direction with 180 degree rotations of the cells about  $[001]_c$  in a  $2/3/2/2/3/2$  sequence. Such a structure gives rise to intensity at  $(1/2, 1/2, 11/14)$  and  $(1/2, 1/2, 17/14)$ . In order to generate additional superlattice intensity near the bcc Bragg peaks, i.e. at the  $\pm (0,0,3/7)$  satellites, and in order to relieve the close approach of hydrogen atoms at the points of 180 degree rotation, an occupation probability having a sinusoidal variation in the  $[001]_c$  direction

Figure 55. A. The hydrogen positions for  $\beta$  hydride, here drawn in the bcc unit cell rather than the fcc representation used previously.

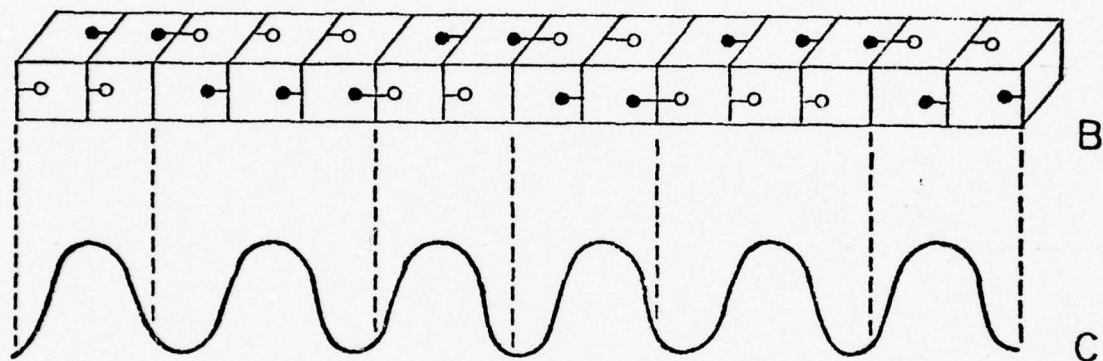
B. A 14  $\beta$  cell, layered, 2/3/2/2/3/2 structure. Dashed lines delineate points where a 180 degree rotation was performed. Such a rotation places hydrogen atoms in a new set of  $\{112\}_c$  planes but does not generate a domain boundary since the orthorhombic distortions are equivalent for both sets.

C. A distribution of hydrogen occupation probability,  $|A \sin(3\pi z/7) + B|$ . Low probabilities occur near areas of closest hydrogen atom approach.

D. A diffraction pattern as generated by structure factor computer calculation using the unit cell formed by superposition of B. and C. above. Note agreement with Figure 51 and Brun<sup>(42)</sup>.

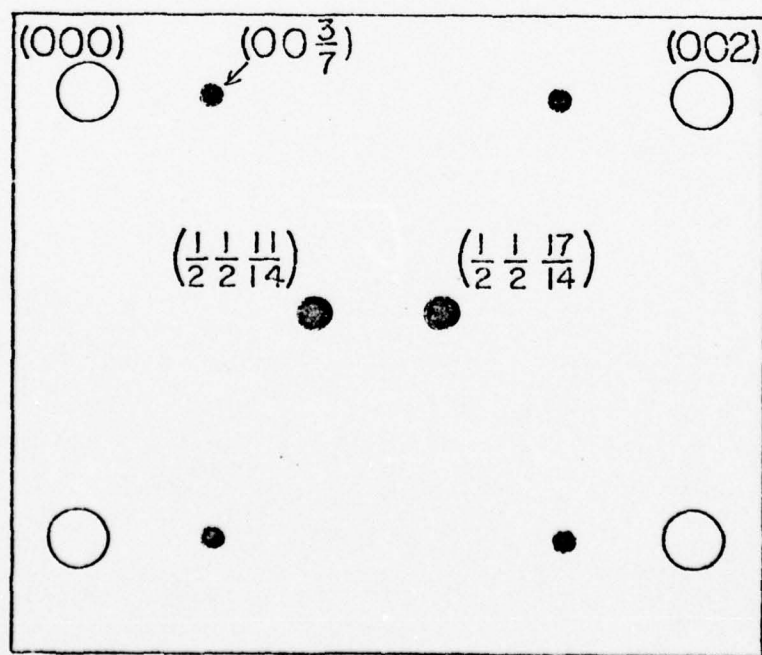


A

 $\leftarrow 001$ 

B

C



D

was superimposed on this structure. The results of such structure factor calculations are shown in Figure 55. The wavelength of the distribution was taken to be  $0,0,7/3$ . The function  $|A\sin(3Z\lambda/7)+B|$  can be adjusted to maintain the overall hydrogen concentration by means of the parameters A and B. The minima in such a distribution are nearly coincident with sections of the unit cell where close approach of hydrogen atoms occurs. The required satellites near the bcc reflections along  $[001]_c$  are generated by such a distribution. The variation of the  $\lambda$  structure with H/Nb can be accounted for by varying the periodicity of the  $\beta$  cell stacking and the wavelength of the probability distribution. As H/Nb increases the interval between rotations and the wavelength of the probability distribution would both increase. As H/Nb approaches 1 the structure approaches the  $\beta$  hydride. The validity of the model can possibly be tested with neutron intensity measurements.

#### 4.3 The High Temperature $\alpha \leftrightarrow \beta$ Transformation

Gahr and Birnbaum<sup>(3)</sup> have demonstrated that there is a marked variation in tensile fracture mode between the  $\alpha$  and  $\alpha'$ - boundary. In the present experiments the structure of the  $\alpha'$  and possible electron diffraction phenomenon associated with elastic softening were examined. Palladium coated, pre-thinned sample were cathodically or gaseously charged to compositions between H/Nb = 0.50 and H/Nb = 0.90. The samples were then heated *in situ* in the electron microscope. The observed  $\beta \rightarrow \alpha'$  transformation temperatures are shown in Figure 56. At  $T_c(\beta \rightarrow \alpha')$  the  $\beta$  domain boundaries disappeared suddenly (Figure 57) as did the  $\{1\frac{1}{2}1\}_c$  superlattice reflections (Figure 58). Considerable bend contour motion accompanied the transformation. No diffraction

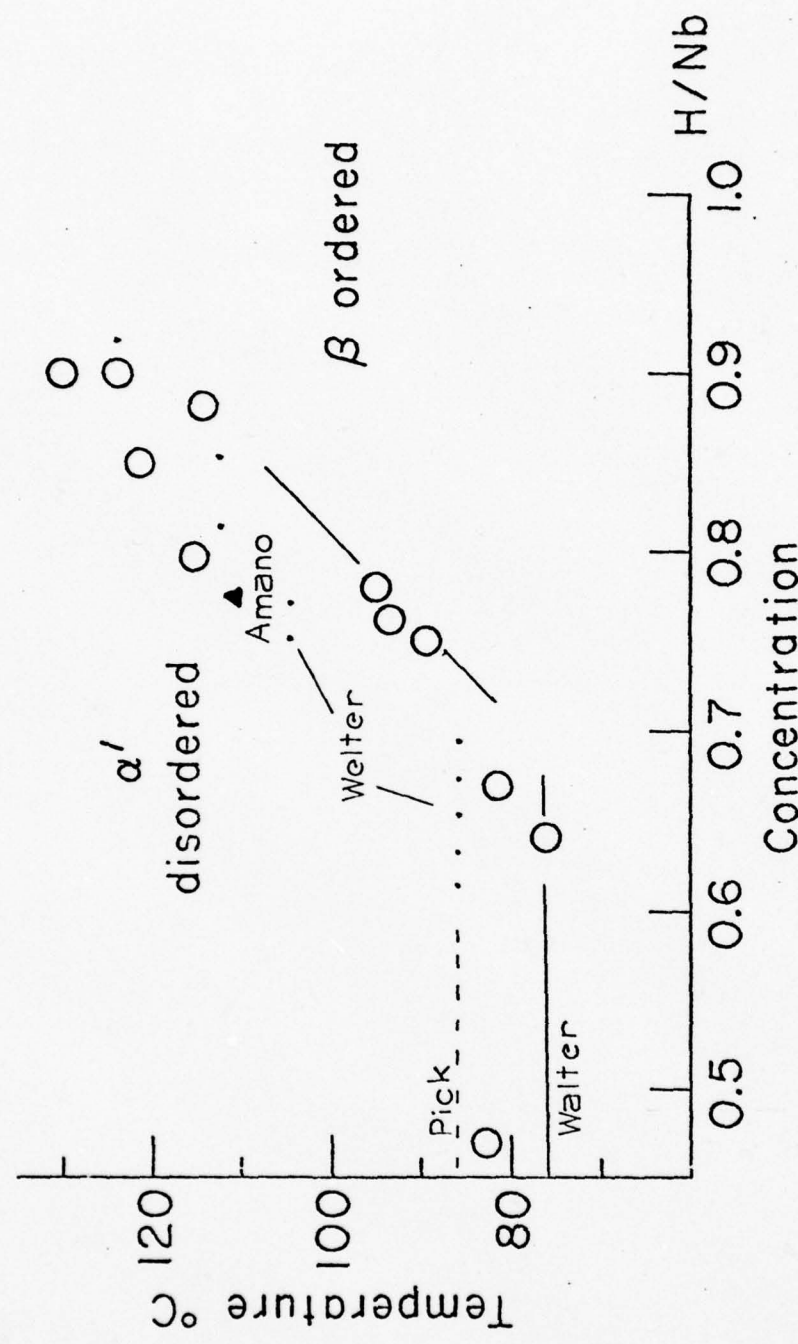


Figure 56. The temperatures at which the thinned area of various hydride samples transformed from  $\beta$  hydride to  $\alpha'$  hydride to  $\alpha'$  solid solution.

Figure 57. A. A  $\beta$ -hydride ( $H/Nb = .79$ ) sample at  $78^\circ C$ . Note the presence of domain boundaries.

B. Same area as previous figure but at  $140^\circ C$ . Note the absence of domain boundaries in the  $\alpha'$  phase.

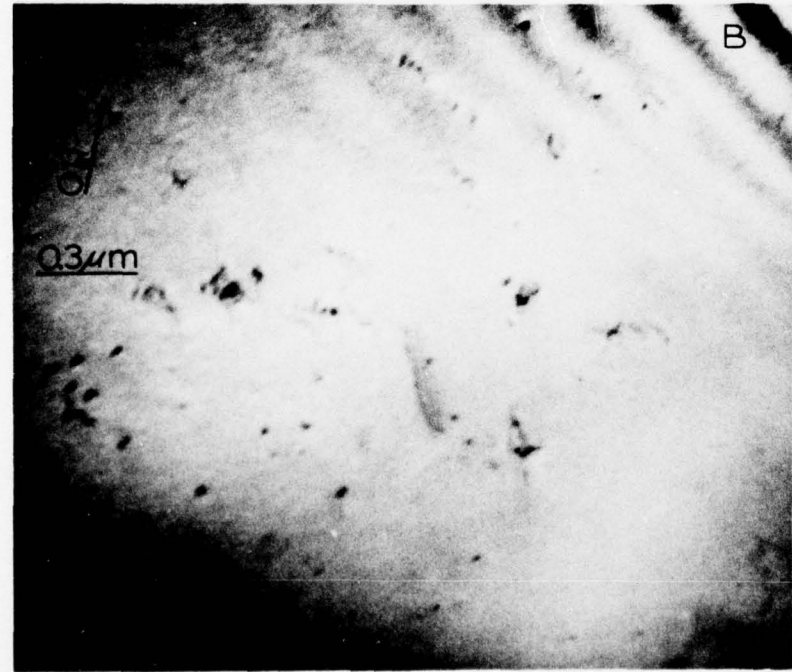
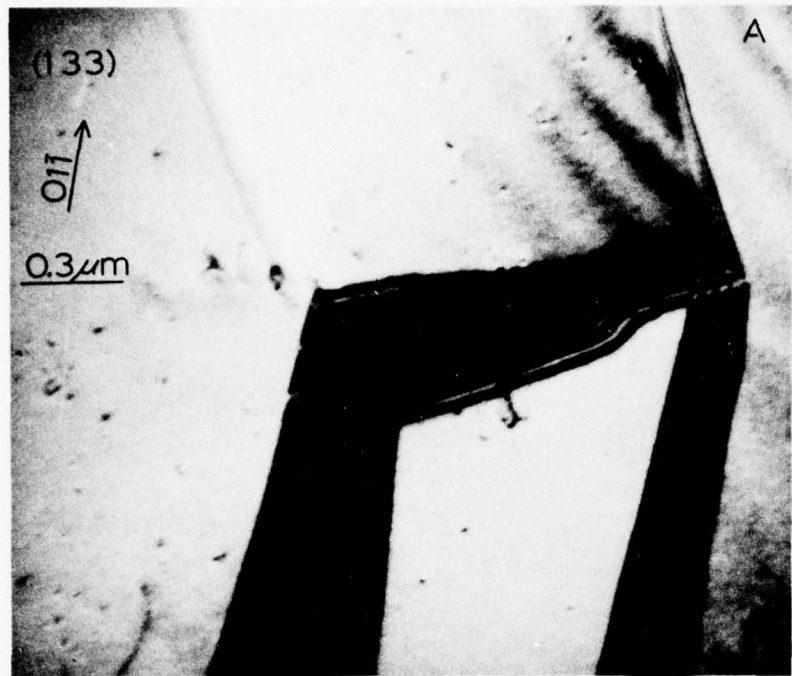
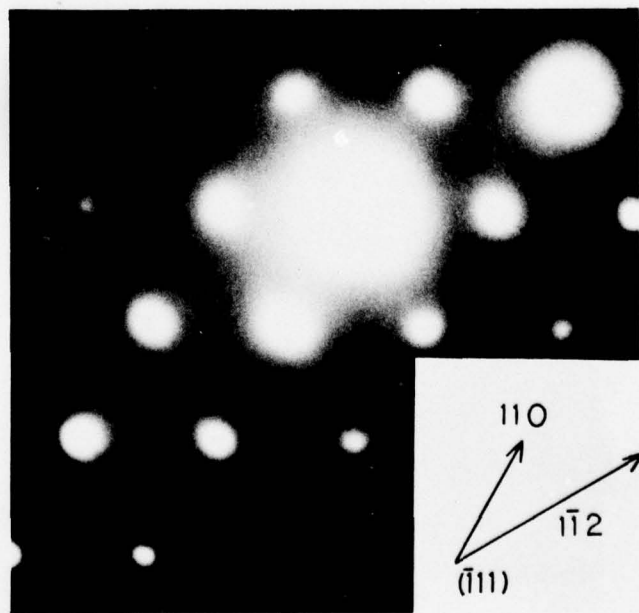
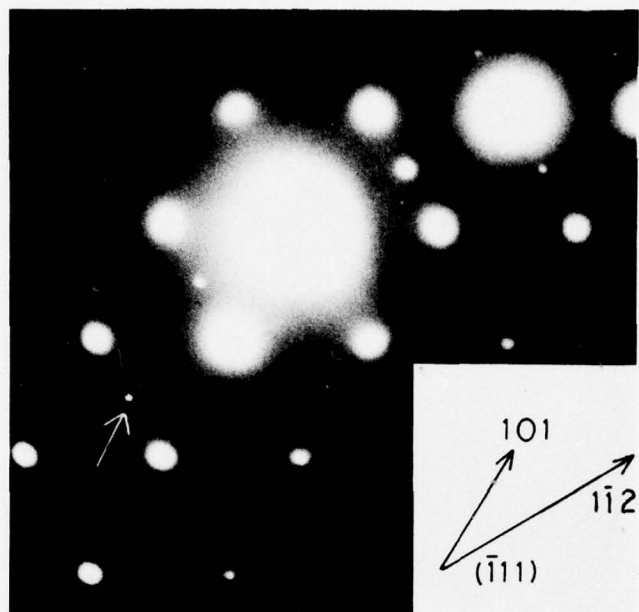


Figure 58A.  $\{111\}_c$  electron diffraction pattern showing superlattice  $\beta$  reflections at  $102^\circ\text{C}$ ;  $\text{H/Nb} = 0.76$ .

Figure 58B. Same as previous figure but at  $108^\circ\text{C}$ . Note the absence of superlattice reflections.



anomalies such as streaking or diffuse scattering could be observed at or above  $T_c$ . It should however be noted that Brun et al. (42) in a parallel study, using neutron diffraction have reported some weak diffuse scattering in the  $\alpha'$  phase near the extinct  $\{111\}_c$  reflection as well as some asymmetry in the diffuse scattering intensity near the bcc Bragg reflections. No evidence for these effects was observed in electron diffraction. The neutron diffraction technique has inherently lower background and a greater facility for reliable intensity measurements. The results of Brun et al. suggest short range order correlations for the H positions in the  $\alpha'$  phase which are not detected in electron diffraction.

In returning to the  $\beta$  phase during cooling, the domain boundaries generally reappeared in the same pattern as before heating. No hysteresis was observed for  $T_c$  on heating vs. cooling.

#### 4.4 $\delta$ Hydride - $\text{NbH}_2$

As discussed in Section 2, the dihydride  $\text{NbH}_2$  has a flourite structure (Figure 59) with Nb atoms occupying a face centered cubic lattice and the H atoms occupying tetrahedral interstitial sites that form an interpenetrating simple cubic lattice. Previous attempts to study the  $\delta$  hydride using TEM have been unsuccessful due to the difficulty in handling brittle  $\delta$  bulk samples during electropolishing. In this investigation, prethinned palladium coated TEM samples were charged to compositions  $\text{H/Nb} = 1.02$  to  $1.07$  and mercury quenched as described in Section 3. When examined in TEM, these samples contained very large amounts of plastic deformation and large numbers of microcracks. Diffraction patterns (Figure 60) taken from these specimens

demonstrated the presence of both the  $\beta$  hydride,  $\text{NbH}$ , and the face centered cubic  $\delta$  hydride  $\text{NbH}_2$ . Extensive dislocation tangles prevented the observation of  $\beta$  domain boundaries or the  $\beta$ - $\delta$  interface. Areas which consisted entirely of  $\delta$  could be distinguished morphologically from  $\beta$  hydride by the presence of fcc twins (Figure 61). The twin plane was determined to be  $\{111\}_{\text{fcc}}$  and the twin boundaries were stable under electron bombardment even after removal of the condensor aperture, in contrast to the usual behavior of the  $\beta$  domain boundaries. This difference is consistent with the larger twinning shear for  $\{111\}$  fcc twinning of the  $\delta$  hydride in comparison to the small shear for  $\{110\}_{\text{bcc}}$   $\beta$  domain boundary twinning. Classic fcc twin spots were seen in the associated diffraction patterns (Figure 60). No superlattice reflections were observed.

The occurrence of twins in the  $\delta$  phase may indicate an attempt by the  $\delta$  lattice to match crystallographically with the surrounding  $\beta$  matrix. Since there is a volume increase on going from  $\text{NbH}$  to  $\text{NbH}_2$ , the frequency of twinning in the  $\delta$  phase could be expected to be larger than the frequency of twins (domains) in the  $\beta$  phase. In fact, the density of twins observed here in the  $\delta$  hydride is much larger than that ever observed for  $\beta$  domain boundaries.

In situ observations were also made as a sample containing  $\text{NbH}_2$  lost hydrogen by effusion. The palladium coating of this sample had not been poisoned with mercury. Nearly all of the electron transparent area of this sample was originally twinned  $\text{NbH}_2$ . During "decharging" the foil transformed entirely to multi-domain  $\beta$  hydride. Superlattice reflections from several  $\beta$  domain boundaries were then in evidence.

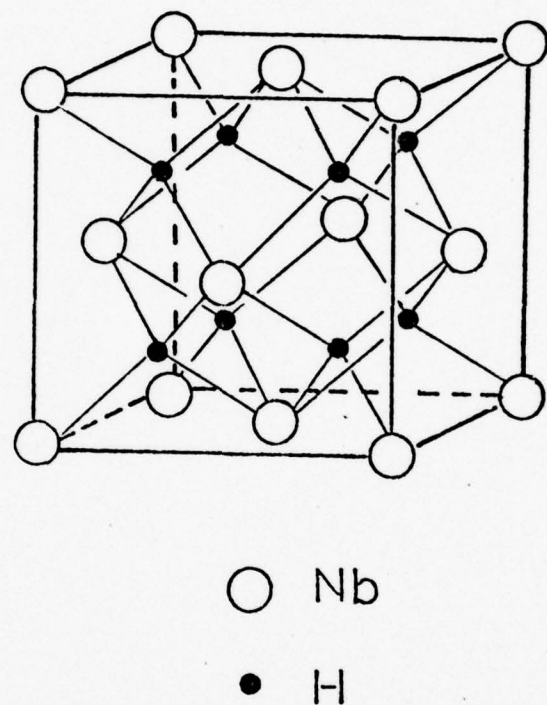


Figure 59. The Fluorite structure of the  $\text{NbH}_2$   $\delta$  - phase.

Figure 60.  $\{110\}_{\text{fcc}}$  diffraction pattern from twinned  $\text{NbH}_2$ ,  $\delta$ -hydride.

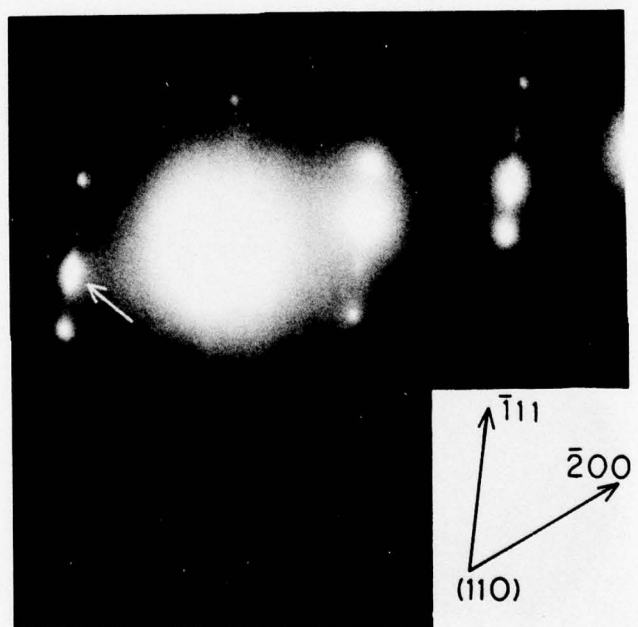
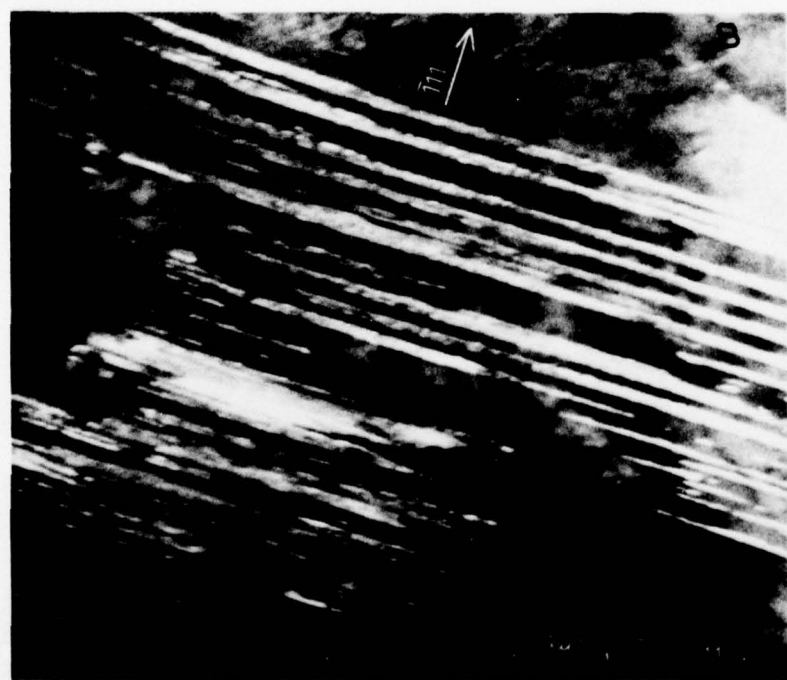
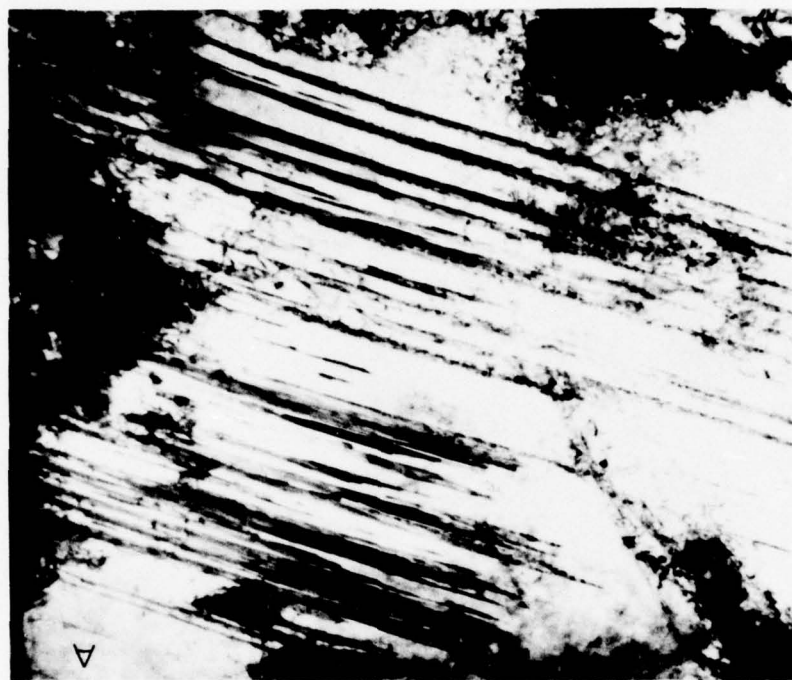


Figure 61. Bright field-dark field pair from twinned  $\text{NbH}_2$   $\delta$  hydride. The fcc twinning reflection used for the dark field micrograph is indicated in Figure 60.



## 5.0 CONCLUSIONS

A method was developed to produce palladium coated niobium composite samples. It was shown that this specimen preparation technique is an effective way to circumvent the oxide surface barrier and to allow impurity free hydrogen charging. Observations, using transmission electron microscopy techniques, were made at several compositions and the results are summarized as follows.

1. The necessary volume accommodation, for hydride precipitation in low H concentration alloys, was shown to cause the punching of interstitial prismatic dislocation loops. The plastic deformation necessary for reversion was observed to occur almost entirely within the shrinking hydride precipitate. Thermal gradients, proximity of free surface, and the presence of other interstitial solutes greatly influenced the nucleation of hydride.

2. The existence of low temperature ordered phases,  $\epsilon$  and  $\zeta$ , was confirmed. The behavior of the  $\beta \rightarrow \zeta$  transformation was shown to be consistent with a second order phase change. Reciprocal streaks were shown to be present in  $\zeta(001)_c$  diffraction patterns and these are interpreted as indicating a tendency toward  $\epsilon$  type ordering the  $\zeta$  phase.

3. The existence of a  $\lambda$  phase at the approximate composition H/Nb = 0.85 was confirmed. Non-crystallographic domain boundaries and superlattice reflections along  $[001]_c$  were observed. The spacing of the superlattice reflections was seen to change with composition. This is consistent with a hydrogen vacancy ordering model based on an incommensurate hydrogen density wave in the  $[001]_c$ .

4. The  $\beta \rightarrow \alpha'$  transformation was observed. No anomalous diffraction effects were detected with electron microscopy techniques.

5. The  $\delta$  hydride,  $\text{NbH}_2$  was shown to have a highly twinned fcc structure. The twin plane observed was  $\{111\}_c$ .

## APPENDIX A

## Flow Chart of Computer Program

The following computer program was used in this work for structure factor calculations.

1. Read H positions (X,Y,Z) and scattering factor  $F_H(X,Y,Z)$
2. Read diffraction pattern of interest (HP,KP,LP)
3. Choose next reciprocal point of interest H,K,L
4.  $\boxed{\text{yes} \text{--- Is } (H,K,L) \cdot (HP,KP,LP) = 0? \text{--- no}}$
5.  $\boxed{S=C=0.}$
6. Sum over all Nb atoms X,Y,Z  

$$S=F(\text{nb}) \sum \sum \sum \sin 2\pi[H \cdot X + K \cdot Y + L \cdot Z]$$

$$C=F(\text{Nb}) \sum \sum \sum \cos 2\pi[H \cdot X + K \cdot Y + L \cdot Z]$$
7. Sum over all H atoms X,Y,Z  

$$S=S+\sum \sum \sum F_H(X,Y,Z) \cdot \sin 2\pi[H \cdot X + K \cdot Y + L \cdot Z]$$

$$C=C+\sum \sum \sum F_H(X,Y,Z) \cdot \cos 2\pi[H \cdot X + K \cdot Y + L \cdot Z]$$
8.  $A^2 = S^2 + C^2$
9.  $\boxed{\text{yes} \text{--- Is } A^2 \text{ significant?} \text{--- no} \rightarrow 3.}$
10.  $\boxed{\text{Save } H, K, L, \text{ and } A^2}$
11.  $\boxed{\text{yes} \text{--- Last } H, K, L? \text{--- no} \rightarrow 3.}$
12.  $\boxed{\text{Set up } 60 \times 100 \text{ plot array}}$
13. Print all H,K,L,A<sup>2</sup>
14. Plot diffraction pattern using numeric characters equal to  $\log_{10}$  (intensity).



```

00001      FUNCTION F(SIN(X,K),X,F)
00002      REAL H,K,L,F(H12,7,7)
00003      DATA F,H,P1/10.,3.14159265/
00004      SIN(X,K),
00005      COS(X,K),
00006      (*****)
00007      DO 40 I=1,4
00008      L=L12-11/4,
00009      D0301251,3,2
00010      2517/4,
00011      00 30 1*1,3,2
00012      Y11/4,
00013      P1=12.*P1*(H(X)*Y11*2)
00014      SIN(X)*SIN(X)*SIN(X)*(P1)
00015      COS(X)*COS(X)*COS(X)*(P1)
00016      40  CONTINUE
00017      00 4012*1,2
00018      2*112-11/2,
00019      00 40 1*1,2
00020      Y11(-1)*1/2,
00021      P1=12.*P1*(H(X)*Y11*2)
00022      SIN(X)*SIN(X)*SIN(X)*(P1)
00023      COS(X)*COS(X)*COS(X)*(P1)
00024      40  CONTINUE
00025      00 50 1*1,7,2
00026      1*11/4,
00027      D05121,3,2
00028      2*11/4,
00029      D045 1*1,2
00030      1*112-11/2,
00031      P1=12.*P1*(H(X)*Y11*2)
00032      SIN(X)*SIN(X)*SIN(X)*(P1)
00033      COS(X)*COS(X)*COS(X)*(P1)
00034      45  CONTINUE
00035      00 50 1*1,2
00036      2*112-11/2,
00037      00 50 1*1,3,2
00038      Y11/4,
00039      P1=12.*P1*(H(X)*Y11*2)
00040      SIN(X)*SIN(X)*SIN(X)*(P1)
00041      COS(X)*COS(X)*COS(X)*(P1)
00042      40  CONTINUE
00043      SIN(X)*SIN(X)*SIN(X)
00044      COS(X)*COS(X)*COS(X),
00045      *****CONSIDER N LATTICE POINTS
00046      00 51 1*1,2
00047      D05111,15,2
00048      D051121,2,2
00049      1*11/4,
00050      2*112/4,
00051      X1X/16,
00052      P1=12.*P1*(H(X)*Y11*2)
00053      SIN(X)*SIN(X)*SIN(X)*(P1)
00054      COS(X)*COS(X)*COS(X),
00055      53  CONTINUE
00056      *****END OF SUBROUTINE

```

## APPENDIX B

The Formation of Oxides During High Temperature  
Gaseous Hydrogen Charging

Since the oxide layer on the surface of niobium is an effective barrier to hydrogen entry, the gaseous charging of samples usually requires heating to 650°C in order to dissolve the impermeable layer<sup>(67)</sup>. This procedure is known to introduce a quantity of oxygen which may be insignificant in large bulk samples, but could be of greater significance in thin foils (<2000Å). An investigation was therefore undertaken to determine the extent of oxygen contamination during gaseous charging of prethinned niobium specimens.

The annealing of thin samples, in the absence of hydrogen at 650°C in vacuums of  $10^{-8}$  torr resulted in large numbers of oxide precipitates throughout the volume of the specimen (Figure 62). In contrast, annealing at 250°C for 18 hours in a vacuum of  $10^{-8}$  torr did not produce any precipitates which were visible in TEM. Similar specimens were then annealed in an atmosphere of 0.16 torr  $H_2$  for 18 hours in an attempt to diffuse hydrogen through the surface oxide layer. Subsequent analysis showed that  $H/Nb = 0.025$  had been achieved compared to the  $H/Nb = 0.05$  expected from equilibration with hydrogen gas. Hydrogen charging can therefore occur by permeation through the surface oxide during long time anneals at relatively low temperatures.

TEM examination of these specimens revealed a high concentration of precipitates in the thinnest part of the foil, within 10 m of the central perforation as shown in Figures 63-64. Selected area diffraction patterns,

Figures 65-67, exhibited a large number of superlattice reflections and could not be indexed with any of the known hydride structures. In situ heating and cooling experiments also showed that the precipitates were not hydrides. Rapid cooling to 77°K did not cause growth of these precipitates, although formation of  $\beta$  hydride occurred in the thick portions of the foil away from these precipitates. Heating to 250°C in the transmission electron microscope caused growth and further nucleation of the precipitates similar to that seen by Van Landyt<sup>(68)</sup> and shown in Figure 68. If these had been hydrides, dissolution would have occurred. Additional annealing of these samples at 400°C and at vacuums of  $10^{-8}$  torr for 18 hours produced the changes in the morphology and structure of the precipitates shown in Figure 69.

Apparently an interstitial phase other than a hydride forms during annealing of niobium thin foils in a purified hydrogen atmosphere. This phase is most likely a suboxide of niobium. Such suboxides have been seen in the V-O<sup>(7,69)</sup>, Ta-O<sup>(70,71)</sup> and Nb-O<sup>(72)</sup> systems. They are characterized by diffraction patterns which contain large numbers of superlattice reflections whose spacings are not simple fractions of the normal bcc reciprocal lattice vectors. There is no dislocation structure associated with the suboxides which usually contain twin boundaries parallel to  $\{110\}_c$  planes (Figures 70-72). The twinning results from the multiplicity of oxide ordering variants (domains) in which the oxygen sublattice has different orientation relative to the bcc niobium lattice.

Monfort et al.<sup>(72)</sup> have determined the reciprocal lattice (Figure 73) for a tetragonal suboxide of niobium ( $\text{Nb}_8\text{O}$  to  $\text{Nb}_{6.5}\text{O}$ ) which they call  $\text{NbO}_X$ (I). The electron diffraction patterns presented in Figures 65-67 can be satisfactorily interpreted as super-positions of two or more single-domain

patterns from this suboxide. Exact oxygen sites for this niobium suboxide structure are not yet available in the literature. Milillo and Potter<sup>(70)</sup> have recently calculated oxygen positions in tantalum for a very similar, but not identical, suboxide.

It is notable that the formation of the niobium suboxide precipitates occurred only in the presence of purified hydrogen gas. One possible explanation is that the hydrogen aids in the transport of contaminants, principally oxygen, to the niobium sample from the surrounding vacuum system walls.

Hickmott<sup>(72)</sup> has established that for glass vacuum systems the presence of hydrogen increases the partial pressure of water vapor. This occurs principally through the formation of atomic hydrogen at hot tungsten ionization gauge filaments and the subsequent reduction by this hydrogen of  $\text{SiO}_2$  at the vacuum chamber walls. It is possible that a similar cycle involving hydrogen reduction of metal oxides at vacuum system walls exists for the stainless steel hydrogen charging system used in this work<sup>(74)</sup>. Annealing below  $1600^{\circ}\text{C}$  in an atmosphere of water vapor is known to irreversibly increase the oxygen concentration of niobium<sup>(75)</sup> and Monfort et al.<sup>(72)</sup> observed a suboxide phase identical to that observed in the present work after charging in argon saturated with water vapor at  $350^{\circ}\text{C}$ .

Figure 62. Oxide precipitates which formed in niobium thin foils during annealing at  $650^{\circ}\text{C}$  and a vacuum of  $10^{-8}$  torr.

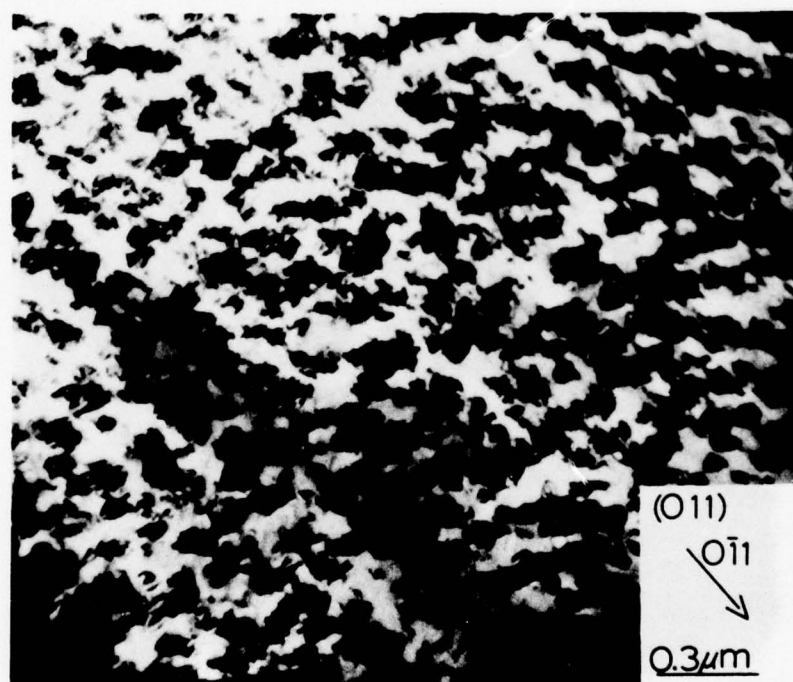


Figure 63. Precipitates which formed in thin foils which had been annealed at 250°C in an atmosphere of 0.16 torr  $P_{H_2}$  for 18 hours.

Figure 64. These precipitates formed only in the thinnest areas of the foil, thus forming a ring around the central perforation.

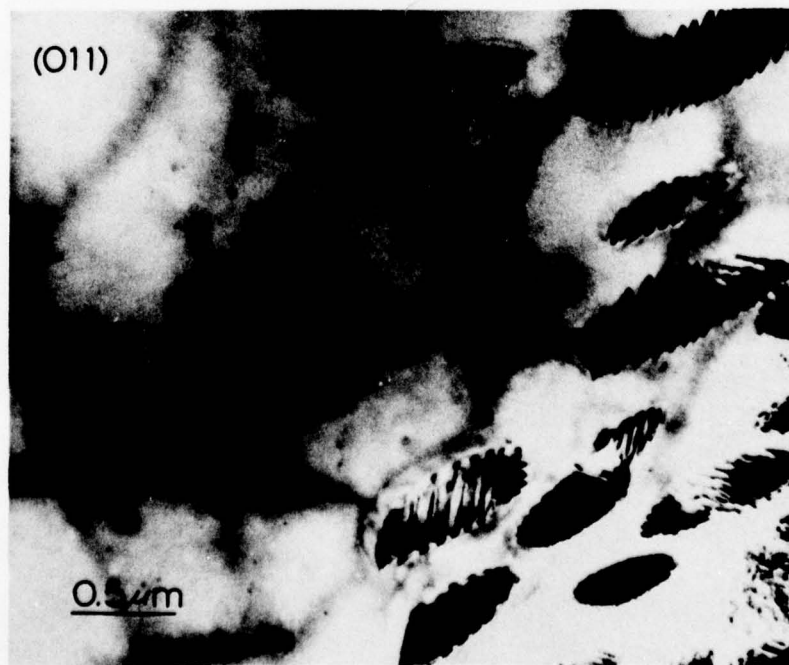
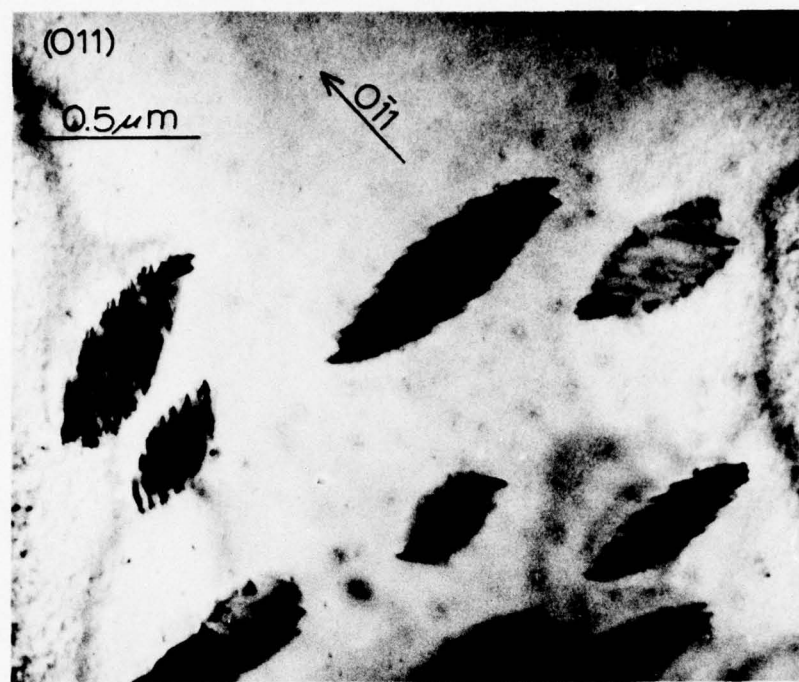


Figure 65. Multi-domain electron diffraction patterns taken from precipitates similar to those shown in Figure 64.

- A.  $(\bar{1}11)_c$  pattern
- B.  $(011)_c$  pattern

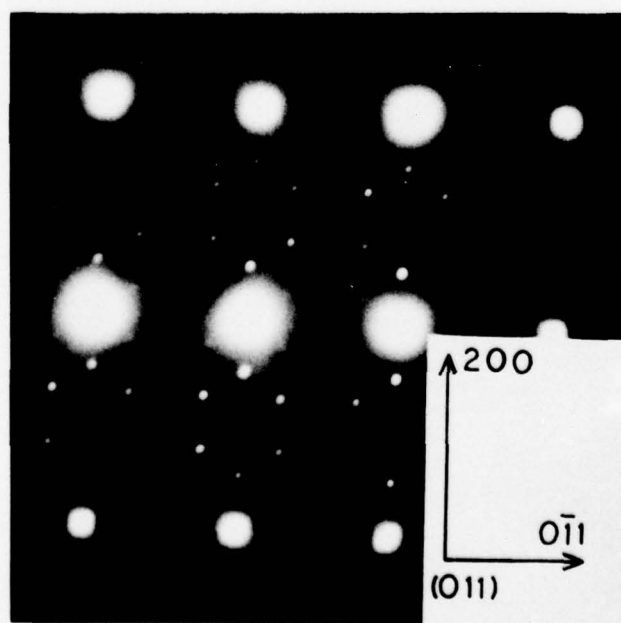
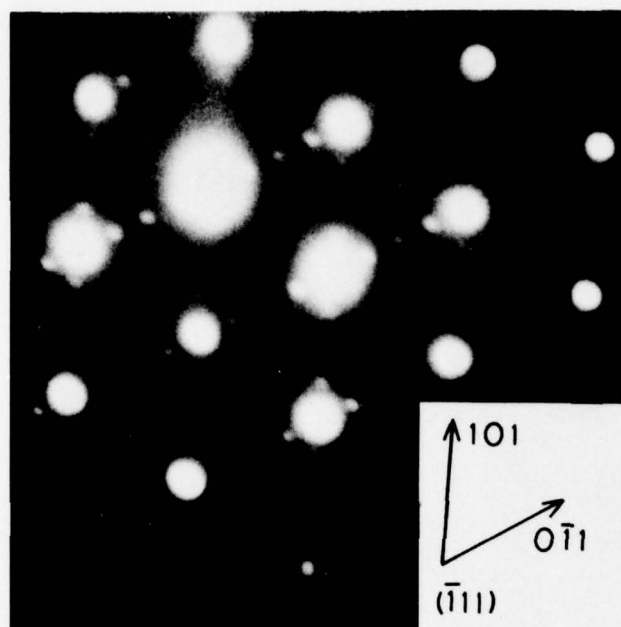


Figure 66.  $\{100\}_C$  multi-domain electron diffraction patterns taken from precipitates similar to those shown in Figure 64.

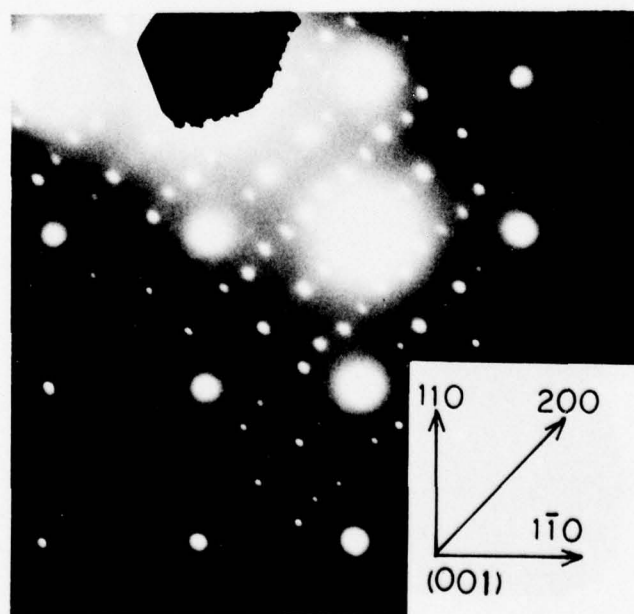
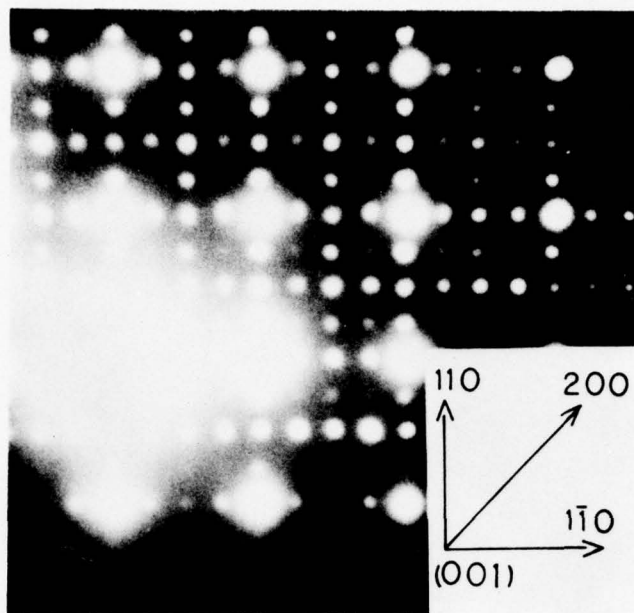


Figure 67. A  $\{100\}_c$  electron diffraction pattern taken from precipitates formed during annealing at 250°C in a hydrogen atmosphere. This pattern, and the previous four patterns, can be interpreted as superpositions of several sections through the reciprocal lattice of  $\text{NbO}_x$  (I) shown in Figure 73.

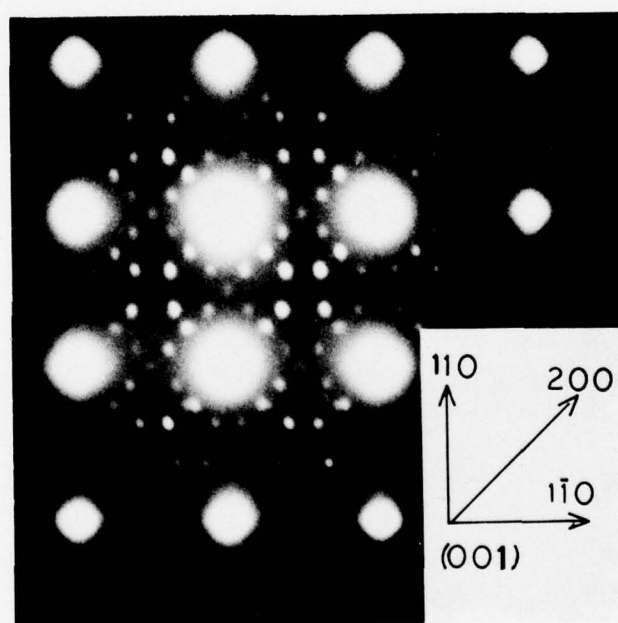


Figure 68. Hot stage experiments done in the electron microscope demonstrated that these precipitates did not dissolve upon heating. In fact, growth and further nucleation were observed.

- A. Suboxide precipitates prior to heating.
- B. Precipitates after heating to approximately 200°C in the electron microscope. (same area as A.)

This behavior is characteristic of an oxide rather than a hydride.

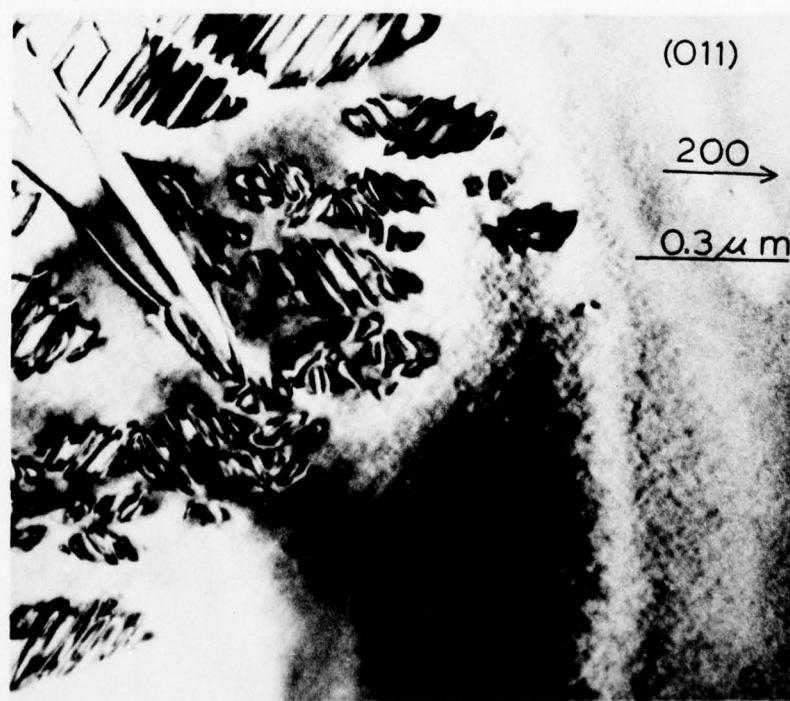
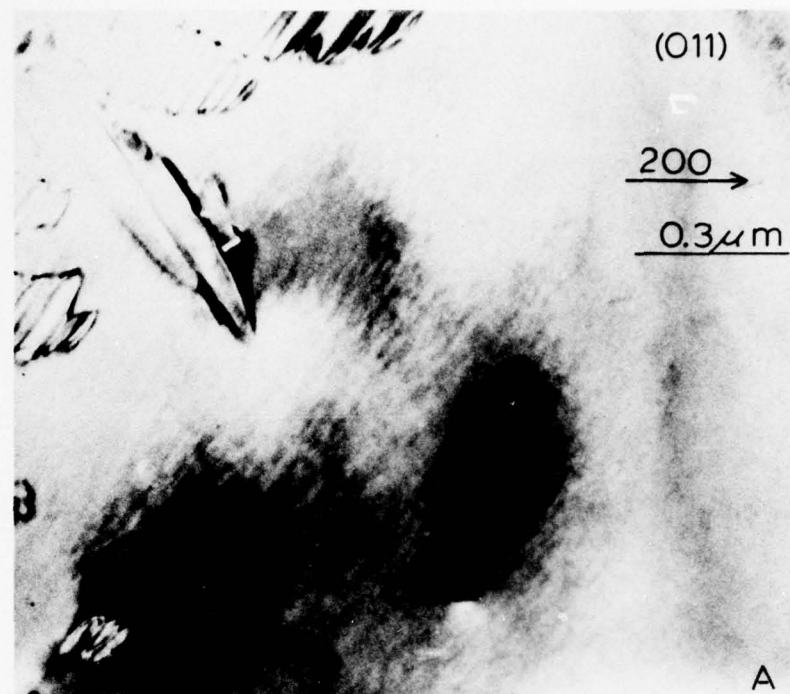


Figure 69. Oxide structure which formed during annealing of foils, which previously contained suboxides shown in Figure 63, for an additional 18 hours at 400°C.



**Figure 70.** Two transmission electron micrographs showing domain boundaries in the suboxide precipitates.

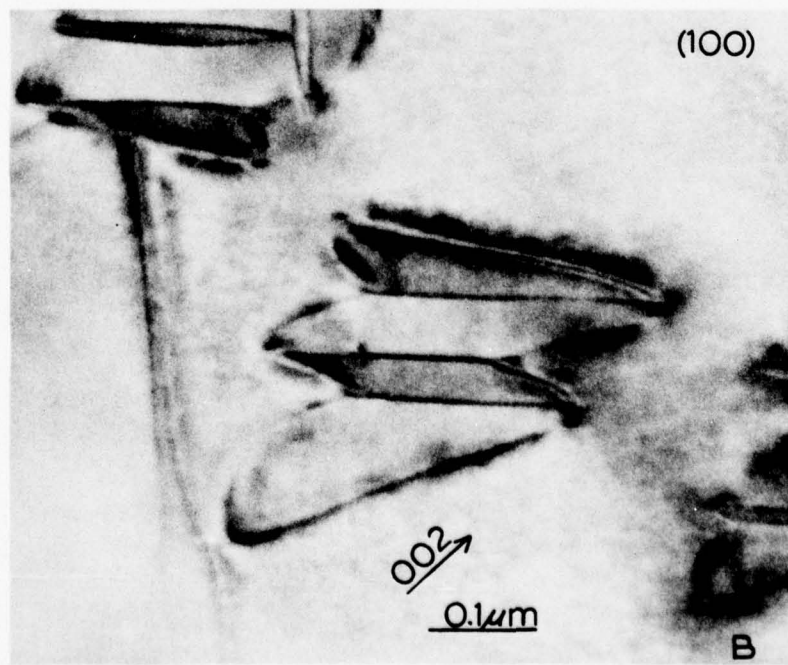
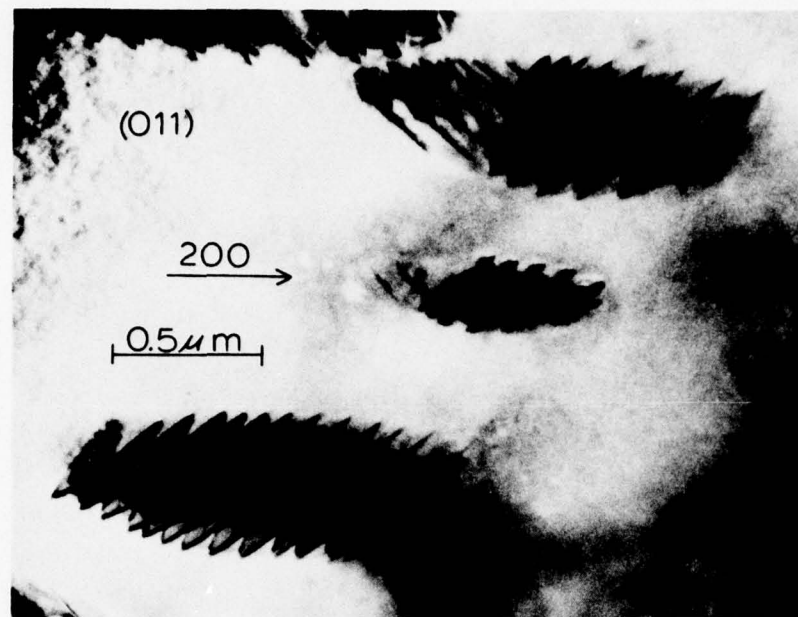
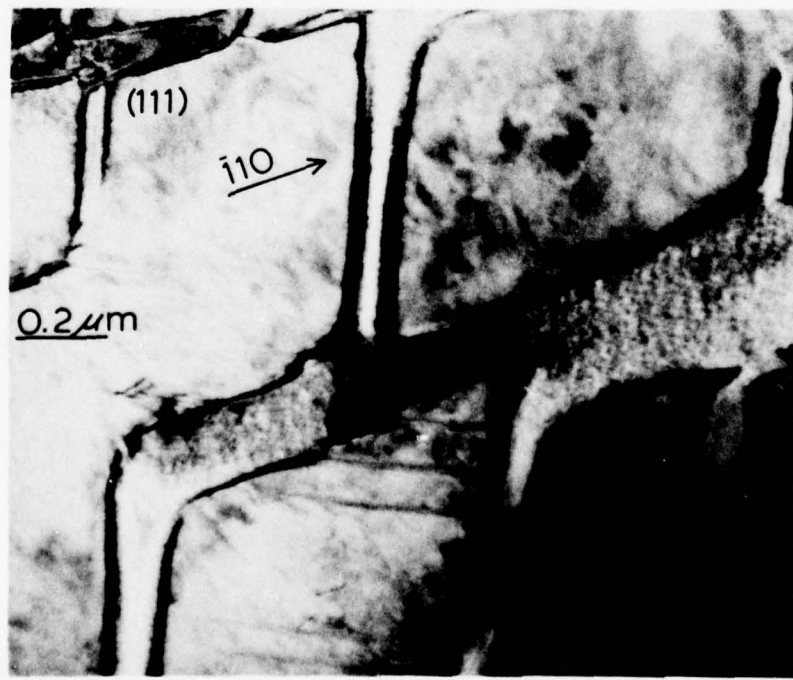
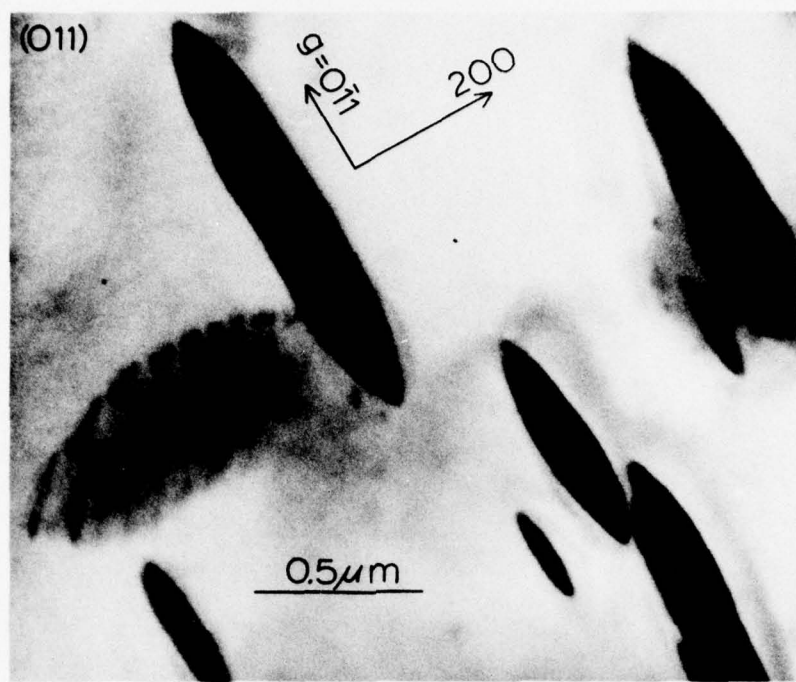


Figure 71. Suboxide precipitates with domain boundaries perpendicular to the beam direction.

Figure 72. Suboxide precipitates with domain boundaries out of contrast.



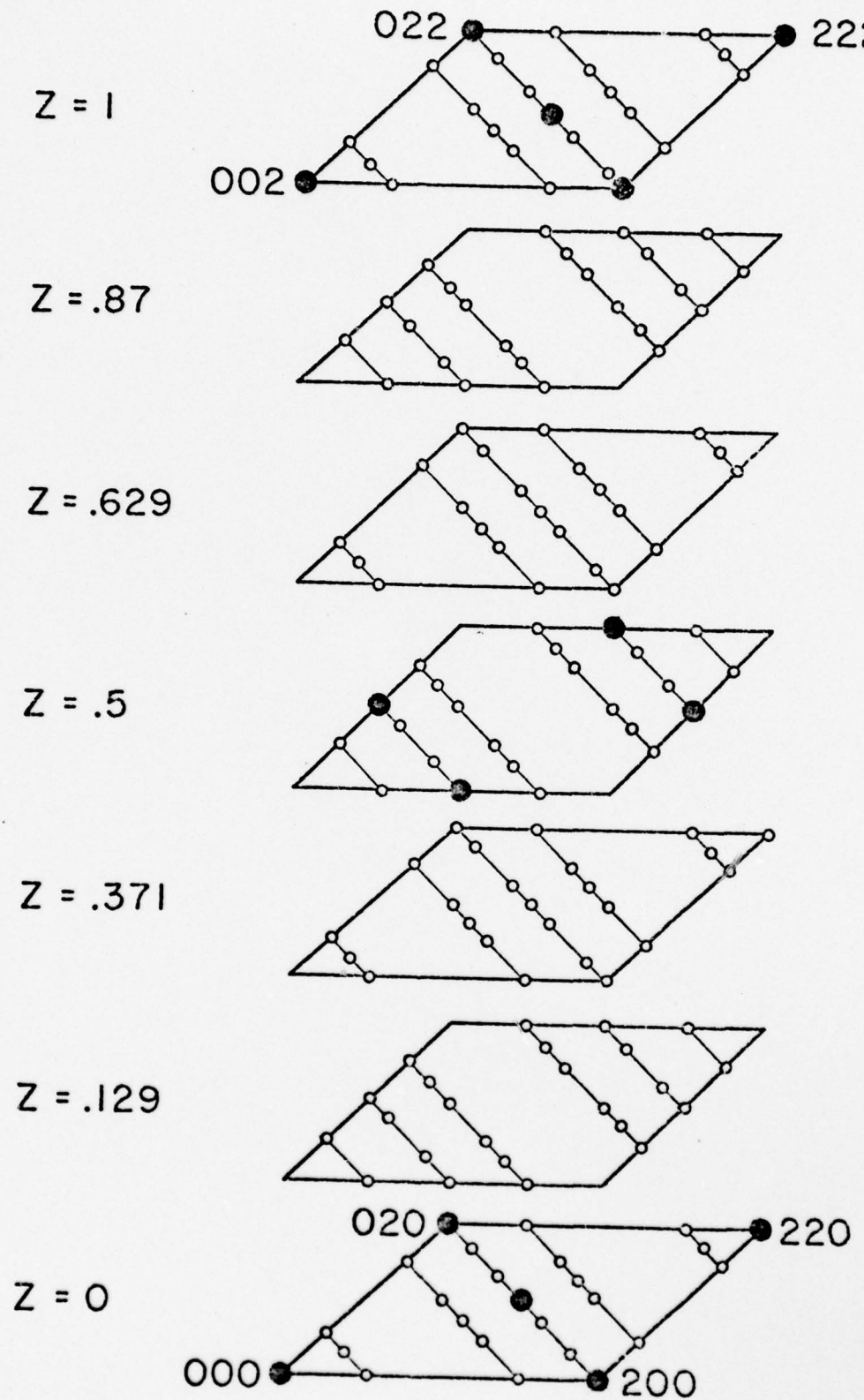


Figure 73. The reciprocal lattice of  $\text{NbO}_x(\text{I})$  as reported by Monfort et al.

APPENDIX C  
Hydrogen Ion Charging

Experiments on bulk samples were conducted to study the effects of hydrogen ion bombardment on the surface oxide layer of niobium and specifically to determine whether both removal of the oxide and entry of hydrogen could be accomplished by this method. In situ ion bombardment was carried out in PHI 545 Scanning Auger Microprobe, SAM, with simultaneous recording of the differentiated niobium and oxygen signals.

Niobium specimens of approximately 1cm x 1cm x .01cm were used in both the as received and UHV annealed conditions. Hydrogen pressures of  $4 \times 10^{-5}$  torr and accelerating voltages of 0.5 to 2KV were employed. The results are shown in Figure 74. The oxygen signal was greatly reduced, though not eliminated, during bombardment. Correspondingly the niobium signal increased. The possible ionic species  $H^+$ ,  $H_2^+$  and  $H_3^+$ , therefore, are thought to have removed at least some of the oxide layer. This most likely is due to chemical attack of the bound oxygen atoms by the hydrogen ion species.

When the samples were removed from the SAM and analyzed for hydrogen content they were found to have picked up no appreciable hydrogen. Likewise other attempts to ion bombard niobium samples with hydrogen ions in a glass vacuum system at accelerating voltages of 0.5 KV to 3 KV and  $H_2$  pressures of  $10^{-4}$  to  $10^{-1}$  torr did not result in any penetration of hydrogen into the bulk sample. Apparently sufficient oxygen remains bound to the niobium surface or to some selective hydrogen entry site, to prevent hydrogen uptake under these conditions.

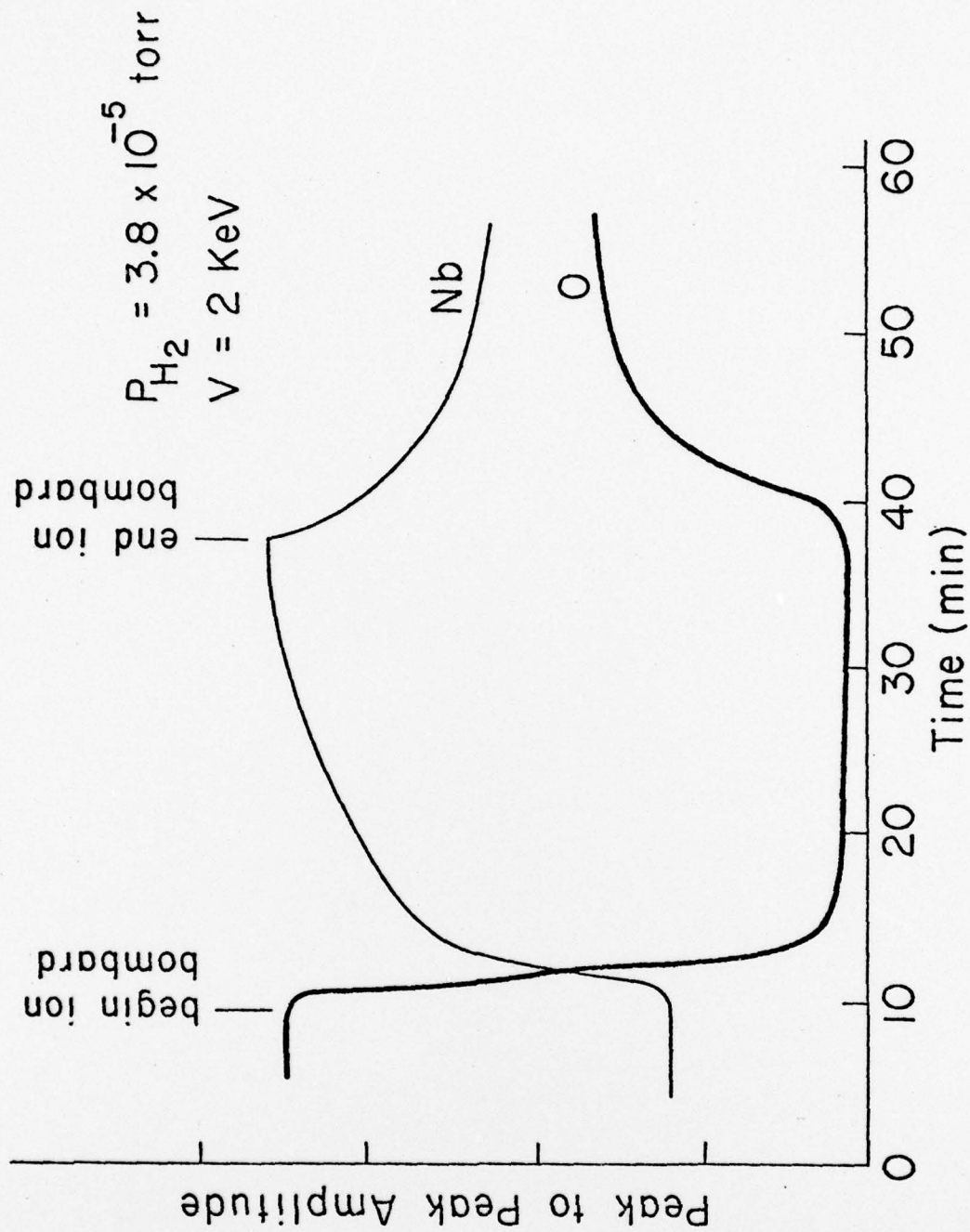


Figure 74. The behavior of the niobium and oxygen Auger electron signals during hydrogen ion bombardment.

## APPENDIX D

The Effects of High Temperature Annealing on Thin Foils  
of Niobium

The following set of micrographs (Figures 75-78) details several attempts to anneal prethinned niobium TEM samples at temperatures higher than those previously indicated in this work,  $1200^{\circ}\text{C}$  ( $\frac{1}{2}T_{\text{mp}}$ )  $< T < 1800^{\circ}\text{C}$  ( $\frac{3}{4}T_{\text{mp}}$ ). A number of interesting surface tension effects are described. Also the precipitation of carbides in thin and bulk samples is noted during non-UHV high temperature vacuum anneals.

Figure 75. During the annealing of niobium thin foils at temperatures 1500°C and 1800°C the thinnest areas of the specimens agglomerate into the thick structures shown.  $T(\text{melting point}) = 2468^\circ\text{C}$ .

Figure 76. During annealing at 1200°C the edge of the central perforation forms very crystallographic features.

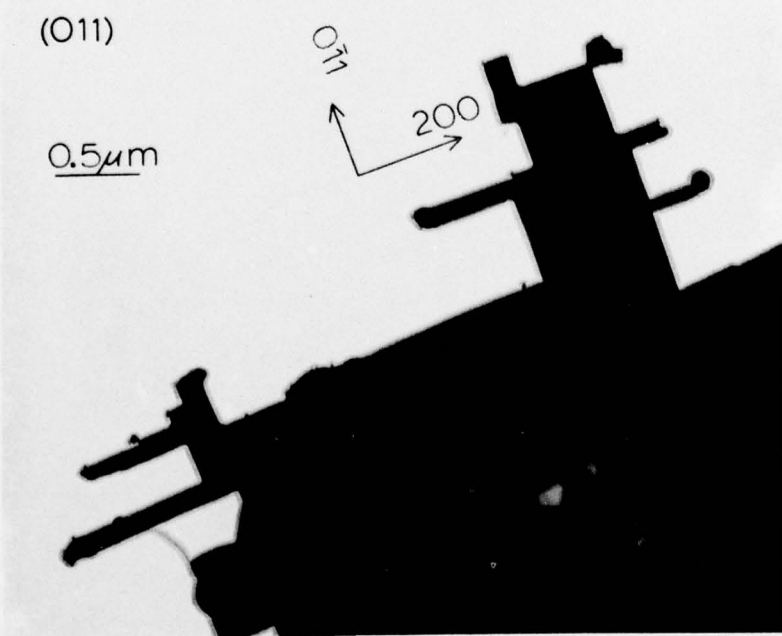
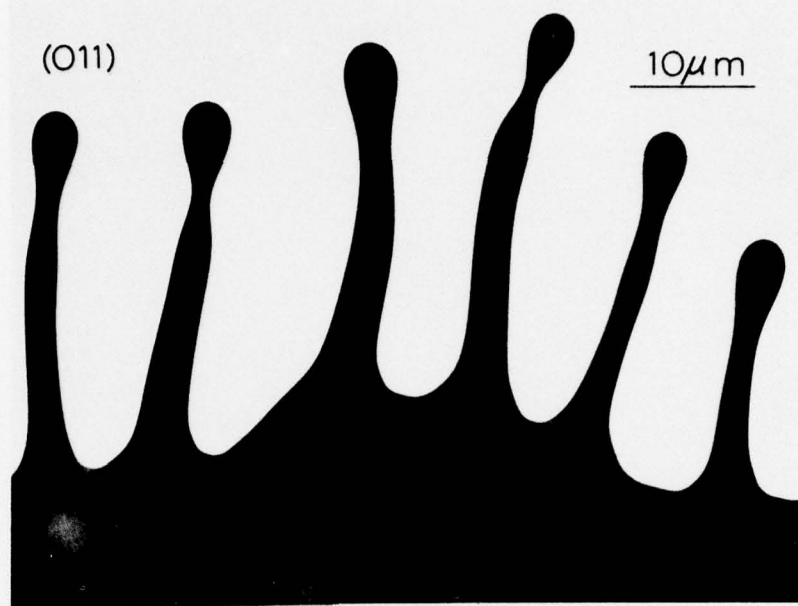
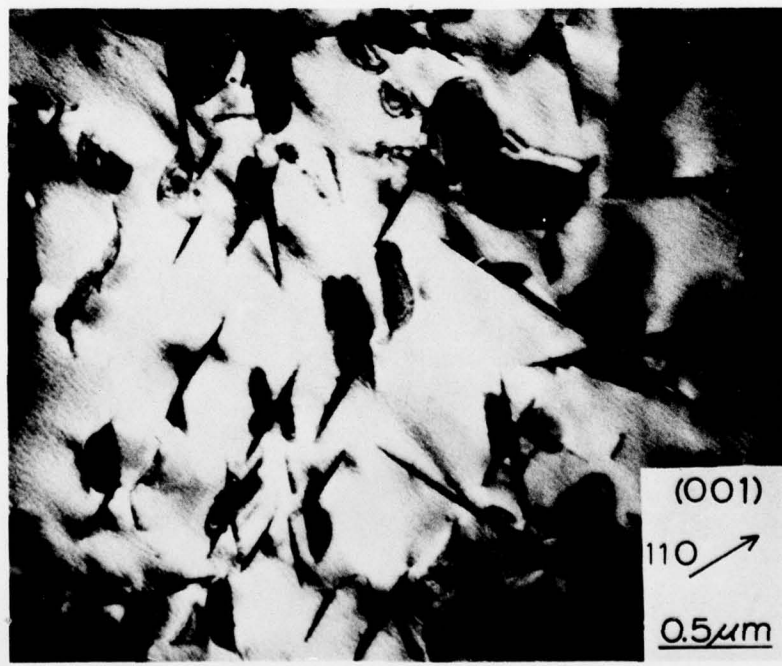
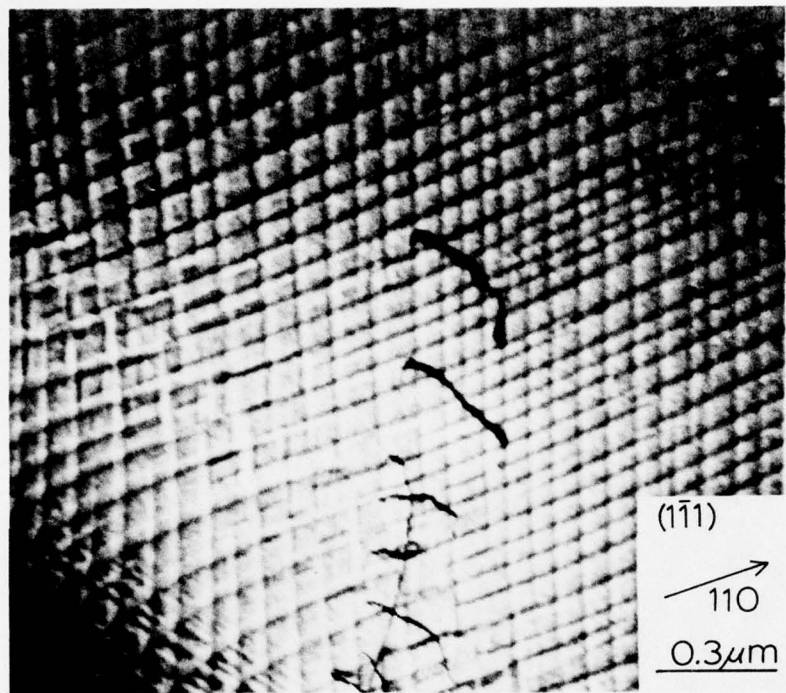


Figure 77. Transmission micrograph showing the striations formed in thin areas not immediately adjacent to the central perforation. Annealing temperature was 1500-1800°C. Further study using SEM techniques demonstrated that these are on the surface of the foil.

Figure 78. Niobium carbides.

The oxygen content of niobium can be effectively lowered by heating in vacuum to temperatures in excess of 1800°C. However, if this annealing is done in non-UHV diffusion pumped systems, as much as 1 atomic percent carbon is introduced into bulk or thin samples. These precipitates are similar in morphology and diffraction pattern to those seen by Viswanadham<sup>(76)</sup>. The vacuum used for outgassing was  $5 \times 10^{-6}$  torr and the bulk samples were 0.003 in. thick.



## REFERENCES

1. D.G. Westlake: Trans. AIME, 245, 287 (1969).
2. S. Gahr, M.L. Grossbeck, and H.K. Birnbaum: Acta Met., 25, 125 (1977).
3. S. Gahr and H.K. Birnbaum: Acta Met., in press.
4. D.G. Westlake, S.T. Okers, M.H. Mueller and K.D. Anderson: Met. Trans., 3, 1709 (1972).
5. T. Schober and A. Carl: Scripta met., 11, 397 (1977).
6. D.I. Potter, H.D. Epstein and B.M. Goldstein: Met. Trans., 5, 2075, (1974).
7. K. Hiraga and M. Hirabayashi: Trans. JIM, 16, 431 (1975).
8. P. Jung and T. Schober: Scripta Met., 9, 949 (1975).
9. T. Schober: Scripta Met., 7, 1119 (1973).
10. M. A. Pick and R. Bausch: J. Phys. F, 6, 1751 (1976).
11. H. W. Paxton, J. M. Sheelan and W. J. Babyak: TMS-AIME, 215, 725, (1959).
12. T. Schober, U. Linke and H. Wenzl: Scripta Met., 8, 805 (1974).
13. T. Schober and U. Linke: J. Less Common Met., 44, 63 (1976).
14. M. L. Grossbeck: University of Illinois, Ph.D Thesis (1975).
15. D. G. Westlake: TMS-AIME, 245, 287 (1969).
16. H. K. Birnbaum, M. L. Grossbeck, and M. Amano: J. Less Common Met., 49, 357 (1976).
17. N. Dahlstrom and B. L. Eyre: Met. Sci. J., 6, 96 (1972).
18. J. C. Williams: Effects of Hydrogen on the Behavior of Metals (ed. A. Thompson and I. M. Bernstein, AIME, 1976) p. 367.
19. R. J. Walter and W. T. Chandler: TMS-AIME, 233, 762 (1965).
20. V. A. Somenkov, A. V. Gurskaya, M. G. Zemlyanov, M. E. Kost, N. A. Chernoplekov and A. A. Chertkov: Soviet Phys. Sol. St., 10, 1076 (1968).
21. T. Schober, M. A. Pick, H. Wenzl: Phys. Stat. Sol., 18, 175 (1973).

22. J. VanLanduyt, R. Gevers, and S. Amelinckx: Phys. Stat. Sol., 13, 467 (1966).
23. R. Gevers, P. Delavignette, H. Blank, and S. Amelinckx: Phys. Stat. Sol., 4, 383, (1964).
24. S. Amelinckx: Surface Sci., 13, 296 (1972).
25. M. P. Cassidy, B. C. Muddle, T. E. Scott, C. M. Wayman and J. S. Bowles: Acta Met., 25, 829 (1977).
26. M. P. Cassidy: University of Illinois Ph.D Thesis (1977).
27. M. S. Rashid and T. E. Scott: J. Less Common Met., 31, 377 (1973).
28. V. A. Somenkov: Ber. Bunsenges. Phys. Chem., 76, 733 (1972).
29. V. A. Somenkov, V. F. Petrunin, S. Sh. Shil'Shtein, and A. A. Chertkov: Soviet Phys. Cryst., 14, 522 (1970).
30. T. Schober: Phys. Stat. Sol. (a), 30, 107 (1975).
31. M. A. Pick: Int. Mttg. Hydrogen in Metals, Julich, Report 6, (1972) p. 90.
32. T. Schober and U. Linke: J. Less Common Met., 44, 77 (1976).
33. R. Heibel and H. Wollenberger: Scripta Met., 10, 945 (1976).
34. M. Amano and H. K. Birnbaum: 6th Int. Conf. on Internal Friction and Acoustical Attenuation, Tokyo (1977).
35. J. Hauck: Acta Cryst., A33, 208 (1977).
36. G. Alefeld, J. Volkl, and J. Tretkowsky: Effects of Hydrogen on the Behavior of Metals (ed. A. Thompson and I. Bernstein, AIME, 1976).
37. H. Zabel and H. Peisl: Phys. Stat. Sol (a), 37, K67 (1976).
38. H. Zabel, G. Alefeld, and H. Peisl: Scripta Met., 9, 1345 (1975).
39. H. J. Fenzl, M. A. Pick, and H. Wenzl: Scripta Met., 11, 271 (1977).
40. W. Maier and H. Wipf: Scripta Met., 11, 695 (1977).
41. M. Amano and H. K. Birnbaum: To be published.
42. T. Brun and H. K. Birnbaum: Private communication (1977).

43. J. J. Reilly and R. H. Wiswall: Inorg. Chem., 9, 1678 (1970).
44. D. G. Westlake and W. R. Gray: Appl. Phys. Let., 9, 3 (1966).
45. A. M. Glauert: Practical Methods in Electron Microscopy, 1, (Elsevier, New York, 1972) p. 3.
46. T. Schober and V. Sorajic: Metallography, 6, 183 (1973).
47. B. J. Makenas and H. K. Birnbaum: Scripta Met., 11, 699 (1977).
48. E. Veleckis and R. K. Edwards: J. Phys. Chem., 73, 683 (1969).
49. B. J. Makenas: Trans AIME, in press.
50. H. Foll and M. Wilkens: Phys. Stat. Sol. (a), 31, 519 (1975).
51. L. M. Brown, G. R. Woolhouse, and U. Valdre: Phil. Mag., 17, 781 (1968).
52. G. C. Weatherly: Phil. Mag., 17 791 (1968).
53. H. Wipf: Electro and Thermotransport of Hydrogen in Metals (Hydrogen in Metals, ed. G. Alefeld and J. Volkl, Springer Verlag, Berlin, 1977).
54. Y. Tullman and E. L. Thomas: To be published.
55. N. Dyson: Xrays in Atomic and Nuclear Physics, (Longman, London, 1973) p. 89.
56. N. J. Zalusec: Private Communication, University of Illinois (1977).
57. C. Baker and H. K. Birnbaum: Acta Met., 21, 865 (1973).
58. R. F. Mattas and H. K. Birnbaum: Acta Met. 23, 973 (1975).
59. G. Pfeiffer and H. Wipf: J. Phys. F, Metal Physics, 6, 167 (1976).
60. H. Y. Chang and C. A. Wert: Acta Met. 21, 1233 (1973).
61. D. G. Westlake and S. T. Okers: Met. Trans. (A), 6, 399 (1975).
62. P. Lecocq: University of Illinois Ph.D Thesis (1974).
63. C. G. Chen and H. K. Birnbaum: unpublished research (1976).
64. T. Schober: The Systems NbH, TaH, and V<sub>2</sub>H (Hydrogen in Metals, ed. G. Alefeld and J. Volkl, Springer Verlag, Berlin, 1977).

65. J. M. Welter, M. A. Pick, T. Schober, J. Hauck, H. J. Fenzl and H. Wenzl: Second Int. Congress on Hydrogen in Metals, Report 1D3, (Paris, 1977).
66. H. E. Cook: *Acta Met.*, 23 1027 (1975).
67. H. K. Birnbaum and C. A. Wert: *Ber. Bunsen. Phys. Chem.*, 76, 806 (1972).
68. J. Van Landuyt: *Phys. Stat. Sol.*, 6, 957 (1964).
69. D. Gunwaldsen and D. I. Potter: *J. Less Common Met.*, 34, 97 (1974).
70. J. Van Landuyt and C. M. Wayman: *Acta Met.*, 16, 803 (1968).
71. F. Milillo and D. Potter: TMS-AIME, in press.
72. Y. Monfort, A. Maisseu, G. Allais, A. Deschanvres and P. Delavignette: *Phys. Stat. Sol.*, 15, 129 (1973).
73. T. W. Hickmott: *J. Appl. Phys.*, 31, 128 (1960).
74. L. C. Beavis: *J. Vac. Sci. Tech.*, 10, 386 (1973).
75. E. From: *J. Vac. Sci. Tech.*, 7, 100 (1971).
76. R. K. Viswanadham: University of Illinois Ph.D Thesis (1973).
77. J. M. Welter: presented at Second Int. Congress on Hydrogen in Metals (Paris, 1977).

## VITA

Bruce James Makenas was born on July 7, 1950 in Evergreen Park, Illinois. He graduated from Michigan State University with a Bachelor of Science Degree in Metallurgy in 1972. Since 1972 he has been a graduate student at the University of Illinois, where he was awarded the Allied Chemical Fellowship for graduate study, and where he received the degree of Master of Science in Metallurgical Engineering in 1973.

Unclassified

Security Classification

DOCUMENT CONTROL DATA - R & D

(Security classification of title, body of abstract and indexing annotation must be entered when the overall report is classified)

1. ORIGINATING ACTIVITY (Corporate author) University of Illinois Department of Metallurgy & Mining Engineering	2a. REPORT SECURITY CLASSIFICATION Unclassified	
3. REPORT TITLE  Precipitation and Ordering in the Niobium-Hydrogen System	2b. GROUP	
4. DESCRIPTIVE NOTES (Type of report and inclusive dates) Technical Report July 1978		
5. AUTHOR(S) (First name, middle initial, last name)  Makenas, Bruce J.		
6. REPORT DATE July 1978	7a. TOTAL NO. OF PAGES 159	7b. NO. OF REFS 77
7a. CONTRACT OR GRANT NO	9a. ORIGINATOR'S REPORT NUMBER(S)	
8. PROJECT NO		
9.	9b. OTHER REPORT NO(S) (Any other numbers that may be assigned this report)	
10. DISTRIBUTION STATEMENT  This document is unclassified. Distribution and reproduction for any purpose of the U.S. Government is permitted.	11. SPONSORING MILITARY ACTIVITY  Office of Naval Research	
12. ABSTRACT  An experimental study, using transmission electron microscopy techniques was carried out to observe precipitation and ordering phenomena in the niobium-hydrogen system. Niobium-hydrogen alloys of composition H/Nb = 0.001 to H/Nb = 1.07 were prepared by improved hydrogen charging methods. Room temperature, hot stage, and cold stage experiments were performed <i>in situ</i> in the electron microscope. The plastic deformation, which accompanies the precipitation and dissolution of hydrides, was observed. Volume constraint, temperature gradients, and impurity traps were shown to have an effect on the nucleation of hydrides. Several low temperature ordered phases, $\xi$ , $\epsilon$ and $\lambda$ were studied using electron diffraction. The crystal structures were observed to change with both temperature and composition. The $\text{NbH}_2$ , $\delta$ -phase was also studied and shown to consist of a highly twinned fcc structure.		

DD FORM 1 NOV 65 1473

Unclassified

Security Classification

**UNCLASSIFIED**

Security Classification

14 KEY WORDS	LINK A		LINK B		LINK C	
	ROLE	WT	ROLE	WT	ROLE	WT
transmission electron microscopy ordering phenomena niobium-hydrogen system						

**UNCLASSIFIED**

Security Classification